Measurement of the $^{17}O(p,\alpha)^{14}N$ Cross Section at Stellar Energies

Jeffery C. Blackmon

University of North Carolina at Chapel Hill

A dissertation submitted to the faculty of the University of North Carolina in partial fulfillment of the requirements for the degree of Doctor of Philosophy in the Department of Physics and Astronomy.

Chapel Hill, North Carolina

1994

Approved by

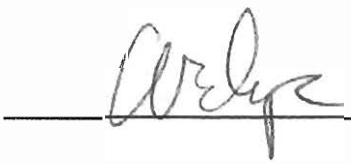 , Advisor

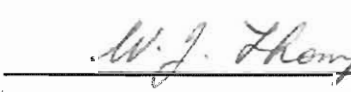 , Reader

 , Reader

JEFFERY C. BLACKMON. Measurement of the $^{17}O(p,\alpha)^{14}N$ Cross Section at Stellar Energies (Under the direction of Arthur E. Champagne.)

ABSTRACT

The isotopic abundance ratio $^{16}O/^{17}O$ has been shown to be a good probe of mass flow and mixing in stars. This ratio is sensitive to the depth of convective mixing which occurs on the giant branch and to the amount of nonconvective mixing occurring on the main sequence. The interpretation of recent observations of this ratio in red giants is limited by a large uncertainty in the value of the $^{17}O(p,\alpha)^{14}N$ reaction rate. This reaction rate is dominated at stellar energies by a resonance at E_x = 5673 keV in the compound nucleus ^{18}F, whose strength was previously uncertain. We have carried out a measurement of the $^{17}O(p,\alpha)^{14}N$ cross section at proton energies of 75 keV and 65 keV. Thick, high-purity Ta_2O_5 targets enriched to 77% ^{17}O were used in conjunction with beam currents of 0.45 mA and large-solid-angle detectors. The background for the experiment was measured using targets of natural isotopic composition. The resonance peak was observed in the data collected at 75 keV, and we determined the proton width of the 5673 keV state to be 22 ± 4 neV. This implies a rate for the $^{17}O(p,\alpha)^{14}N$ reaction that is ten times greater than the typical rates used previously in stellar models.

ACKNOWLEDGMENTS

There are many individuals that contributed to the success of this experiment. Foremost is Professor Art Champagne. His hard work and guidance always kept the project progressing. Mariet Hofstee and Professor Bill Thompson were also invaluable. These three provided untold assistance in analyzing problems and concerns as they arose. Professors Tom Clegg, Ed Ludwig, and Hugon Karwowski also provided me with much good advice.

We collaborated with two groups from outside the university. Michael Smith of Oak Ridge National Laboratory was a great resource. He contributed many good ideas, and Oak Ridge generously supplied electronics, detectors and enriched ^{17}O gas for use in the experiment. We also collaborated with Greg Downing and George Lamaze of the National Institute of Standards and Technology. They arranged beam time at the Cold Neutron Research Facility and assisted with much of our target analysis.

I am very thankful for the tremendous support I received from my fellow graduate students and our post-doctoral researchers. Eric Crosson, Rupak Das, Kurt Fletcher and Susan Lemieux contributed as much as anyone to my graduate education. Zeid Ayer, Tim Black, Dave Junkin, Bill Geist, Beata Kozlowska, Steve Hale, Lijun Ma, Denise Ralston, and Kevin Veal contributed many long shifts during our data collection. I am most grateful to them for their moral support.

Tom Clegg, John Dunham, and Tony Mendez spent many hours working to increase the beam current from the polarized ion source. Their effort is particularly appreciated. Without the substantial gains in beam current we achieved, this experiment would not have been possible.

I owe many favors to the staff at TUNL: Paul Carter, Richard O'Quinn, Sidney Edwards, and Pat Mulkey. They generously lent their technical expertise on many occasions, and frequently on short notice. Special thanks to Paul Carter who not only gave much assistance, but was also a very patient teacher.

Al Lovette, Bob Hogan, and the staff of the Duke Instrument Shop constructed most of the apparatus and were very helpful with the design. Bo Sanford, Hal Mann, and the staff of the UNC Instrument Shop also contributed. I must say a special word of thanks to Carolyn Cox, Barbara Szilvey, and Pat Gibson. Their great interpersonal skills were helpful on many occasions.

Finally, I am most thankful for the support and sacrifices of my family and friends. In particular, I would like to thank Judy Vernon, Anne Smith, and Charles Rasco. Their patience and understanding brings me great comfort and inspiration.

TABLE OF CONTENTS

LIST OF TABLES

LIST OF FIGURES

I. Introduction

Following over half a century of research in nuclear astrophysics, we are confident in our understanding of the processes that power stars. Whereas the nuclear reactions which provide the primary energy generation are well known, there is still much to be learned from studying reactions involving trace isotopes. The observed abundances of the trace isotopes can serve as a diagnostic tool, giving us information about the astrophysical environment. This work focuses on one isotope which is particularly valuable as a diagnostic, ^{17}O.

All stars begin their lives by fusing hydrogen into helium. This occurs for two simple reasons. First, hydrogen is by far the most abundant element in the universe. Thus, when a star is born, most of its mass consists of hydrogen. Second, stars are cold objects by nuclear-physics standards. The temperature at the center of the sun is only 15×10^6 K. The average thermal energy of a particle at this temperature is about 1 keV. This is a small amount of energy compared to the Coulomb repulsion between nuclei. The electrostatic potential energy, V_c, between two nuclei of charge Z_a and Z_b, separated by a distance r is given by

$$V_c = \frac{Z_a Z_b}{r}(1.44 \text{ MeV} \cdot \text{fm}) \ . \qquad (1.1)$$

In order for two protons to fuse, they must get to within 2.5 fm of each other. At this distance the electrostatic potential energy between them is 575 keV, far greater than their kinetic energy. This electrostatic repulsion increases in proportion to the charges of the two particles. Hence, it is much more probable for particles with lower charge to overcome the Coulomb barrier and react. Thus, stars begin by fusing the nuclei with the

Table 1.1: The three primary reactions in the PP-chain.

Reaction	Q-Value (MeV)
$p + p \rightarrow d + e^+ + \nu$	1.44
$p + d \rightarrow {}^3He + \gamma$	5.49
${}^3He + {}^3He \rightarrow {}^4He + 2p$	12.86

smallest charges. The primary sequence of reactions through which a star converts hydrogen into helium is known as the PP-chain. The three most prominent reactions in the PP-chain and the energy that they release are listed in Table 1.1. Because there are no stable isotopes with atomic number 5, the chain terminates with the $^3He + {}^3He$ reaction, and no elements heavier than ^4He are synthesized.

Second generation stars (Population I) contain significant abundances of elements other than hydrogen and helium which could react through proton-capture with the vast supply of hydrogen. We would expect the next most prominent reactions to involve nuclei with the next largest charges: lithium, beryllium, and boron. However, the abundances of carbon, nitrogen, and oxygen are so much greater than the abundances of the lithium, beryllium, and boron that the next most important sequence of reactions is the Carbon-Nitrogen-Oxygen (CNO) cycle.

The CNO cycle is very nearly a closed cycle. A schematic of the cycle is shown in Figure 1.1. Because there are no stable nuclei with atomic number 5 or 8, the CNO nuclei cannot be made by proton-capture reactions. This means that there is no mechanism in the stellar interior to produce these nuclei, at least not until the later stages of stellar evolution. Although some catalytic material can be lost through the sequence $^{18}O(p,\gamma)^{19}F(p,\gamma)^{20}Ne$, this fraction is small because of the comparatively large rate of the $^{18}O(p,\alpha)^{15}N$ reaction. Thus, the net effect of the CNO cycle is to convert hydrogen into helium. Note that if we follow the cycle around any of the closed loops, we turn 4

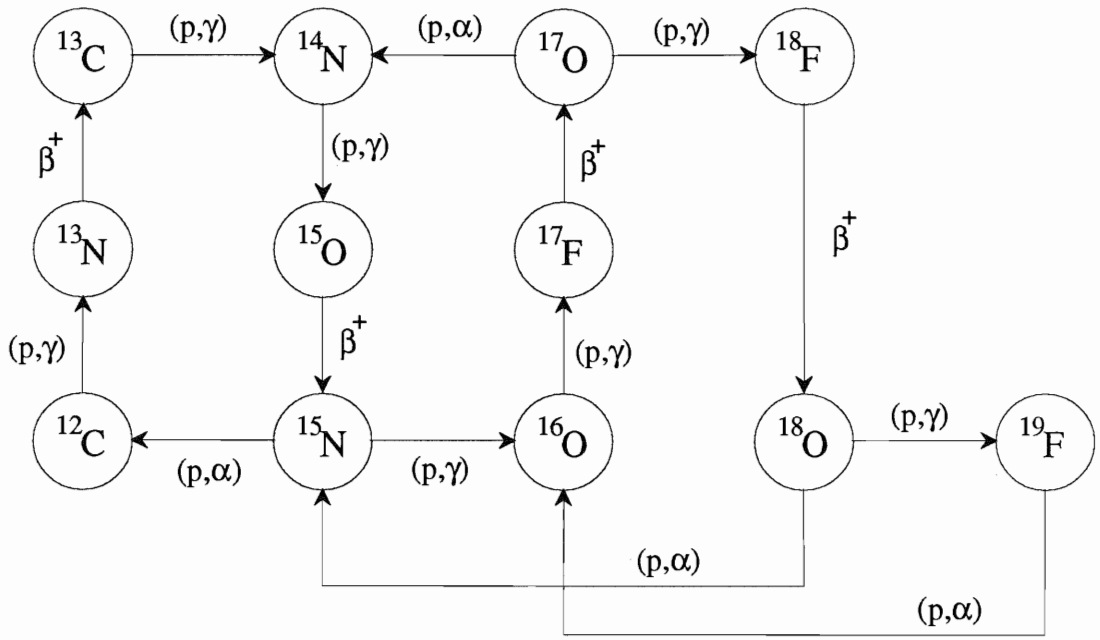

Figure 1.1: Schematic representation of the reactions in the CNO cycle.

protons into an alpha particle and end with the same nucleus with which we started! The CNO nuclei serve as a catalyst for hydrogen fusion. Stars that are heavier than the sun have a higher central temperature. If the central temperature of a star is more than about 20×10^6 K, then the CNO cycle and not the PP-chain will be the dominant method of energy production.

While the total mass in the CNO cycle is approximately constant, the mass is redistributed among the different isotopes. The cycle "bottlenecks" at nuclei which have smaller destruction rates, such as ^{14}N. A Population I star typically begins its main sequence life with most of its CNO mass as carbon and oxygen. The primary redistribution of mass in the CNO cycle is to make nitrogen from carbon and oxygen [Cla83]. The ratios of the abundances of the CNO isotopes depends significantly upon the temperature of the environment and the nuclear reaction rates, and not upon the initial distribution of mass. Because of the strong energy dependence of nuclear reactions, the

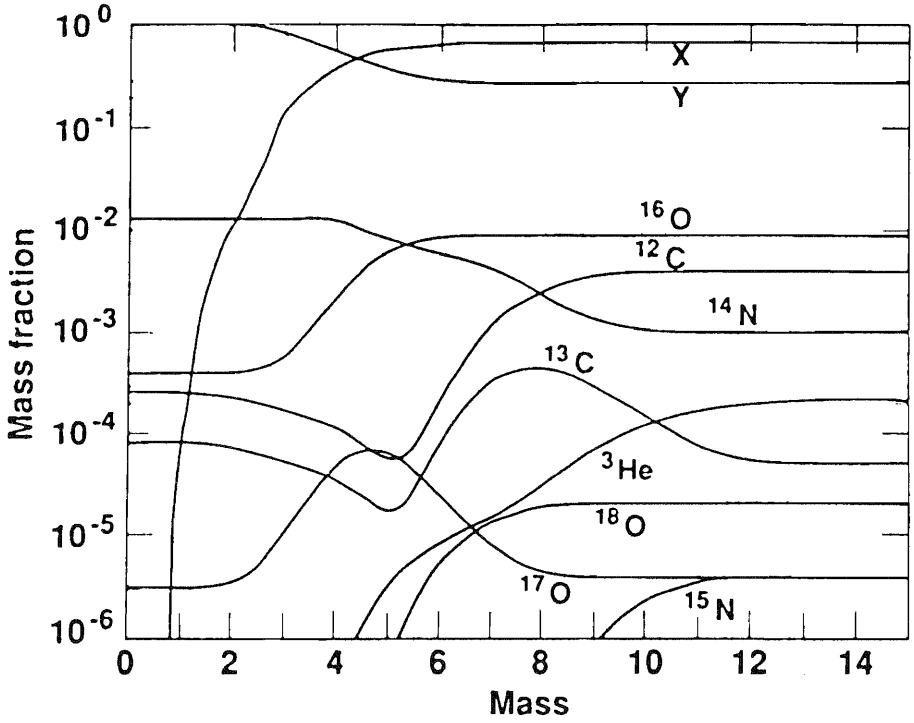

Figure 1.2: The composition structure of a 15-solar-mass model [Dea90].

concentrations of the CNO elements varies dramatically as a function of depth in the stellar interior. The internal composition of a 15-solar-mass star from the calculations of Dearborn [Dea92] is shown in Figure 1.2. The initial composition of the star is effectively the composition on the surface, at Mass = 15, since no nuclear processing has taken place here. As we move to the interior, the overall effect is an increase in the amount of ^{14}N at the expense primarily of ^{16}O and ^{12}C, which are the most abundant isotopes initially. The observed features in the isotopic distributions are a result of the temperature dependence of the nuclear reaction rates.

One limitation in astrophysics is the lack of astronomical observables. Even determining the mass or absolute luminosity of a star can be a tremendous challenge. The only data we have are the light (or sometimes particles) that an object emits or absorbs. This is not a tragedy, since the energy spectrum of light from an object gives us a wealth of information. Every atom and molecule has distinct emission and

absorption lines. By measuring the intensities of these lines, the relative abundances of elements or even isotopes can be determined. However, these observations are limited to the luminous part of a star, its photosphere. All of the nuclear processing that occurs in a star occurs deep in its interior. The abundances of the isotopes in the atmosphere of a star are typically the abundances from which the star was formed and are not sensitive to the nuclear processing that occurs in the interior. Luckily, there are a few exceptions.

One exception occurs when a star begins to exhaust the hydrogen fuel in its core. As the mass fraction of core hydrogen decreases, so does the nuclear power output that provides the pressure support for the core. The core begins to collapse, and the central temperature and pressure increase. This increases the rate at which the remaining hydrogen in the core burns, until all of the hydrogen in the core is virtually exhausted. The hydrogen that remains is in a shell outside the helium core, burning at high temperatures. This dramatic rise in the central temperature of the star causes the atmosphere of the star to expand and cool. This shifts the light from the star towards red in the electromagnetic spectrum, and consequently such stars are called red giants [Cla83].

When the temperature gradient in a star becomes very large, the star cannot be in hydrostatic equilibrium, but is convectively unstable. In this case, an element of gas which is displaced in the radial direction will not feel a restoring force, but will continue to be accelerated in the same direction until it can thermalize with the surrounding medium. This gives rise to the macroscopic motion of mass in the star as a coherent fluid, which serves as a means of energy transport. The distance that gas will travel before it is thermalized is the characteristic length for convection, called the mixing length. This is the distance over which material within the star will be mixed by convection [Boh89].

When a star moves off the main sequence to the giant branch, the large thermal gradient between the hot interior and cool exterior drives convection. The outer envelope

becomes fully convective, mixing material from the surface deep into the interior. This process is called *first dredge-up*, and this is the first evolutionary stage where we can observe changes in the composition of the star caused by nuclear burning in its core [Ick91]. The convective mixing causes dramatic changes in the abundance ratios of the carbon and nitrogen isotopes in the atmosphere. Two of the primary effects of this mixing, as can be seen from Fig. 1.2, are that the ratio of $^{12}C/^{13}C$ will be significantly decreased, while the ratio of $^{17}O/^{16}O$ will be significantly enhanced.

At this stage the temperature in the very outer atmosphere is low enough that a significant fraction of the CNO isotopes are formed into molecules such as CO and CN. The presence of these molecules is evidenced by absorption lines in the spectrum, in the case of CO near $\lambda = 5$ μm. These lines correspond to the different vibrational and rotational states of the molecules. Lines from molecules with a different isotopic composition will appear at slightly different wavelengths because of their different masses. In theory, the isotopic abundance ratios can be inferred from the relative strength of these lines. For example, the ratio of $^{17}O/^{16}O$ in the star would be given by the relative strengths of the vibrational lines from the $^{12}C^{17}O$ and $^{12}C^{16}O$ molecules. In practice, these are extremely difficult determinations to make. There are so many lines in this region of the spectrum that there do not exist distinct lines that correspond to a single molecular species. One instead observes an overall depression of the continuum, with structures evident that are due to several different molecules. In order to make a determination of the $^{17}O/^{16}O$ ratio, one must have very high-resolution spectra and match the spectra with model atmospheres. Despite the difficulties, there have been enough good determinations made to allow a quantitative comparison between the observed abundance ratios and those predicted from stellar models [Dom86, Har84a, Har84b, Har88]. Observations of the $^{12}C/^{13}C$ ratio for 13 stars ranging in mass from 1 to 15 solar masses is shown in Figure 1.3. The initial ratio of $^{12}C/^{13}C$ is about 90, so the stars show a depletion in the $^{12}C/^{13}C$ ratio by a factor between 4 and 10. A calculation of this

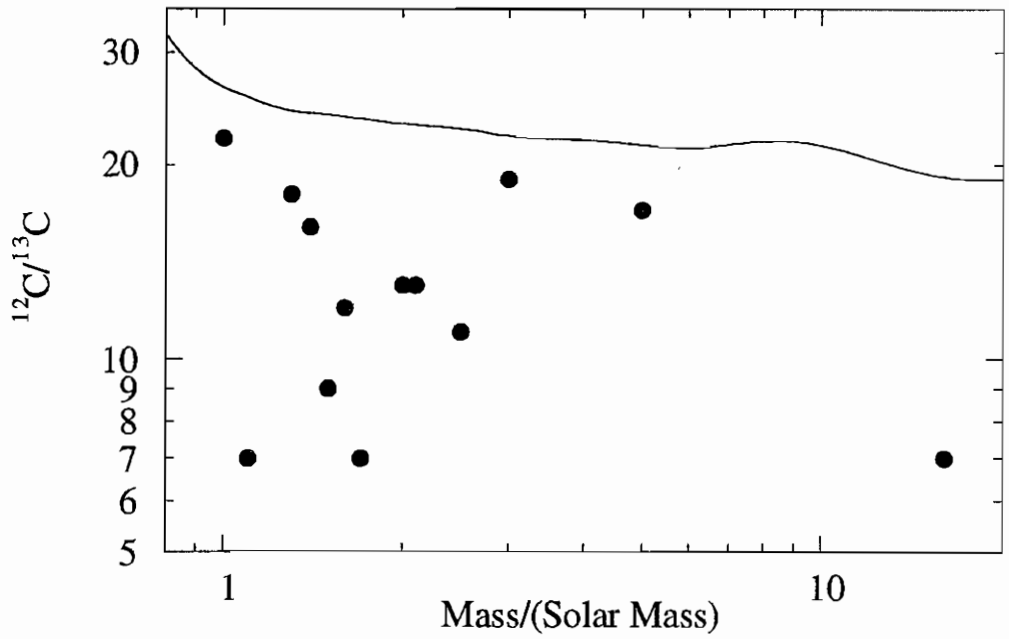

Figure 1.3: Measured $^{12}C/^{13}C$ ratios in 13 red giants [Dom86, Har84a, Har84b, Har88]. The smooth curve is the calculated abundance by Dearborn [Dea92].

ratio by Dearborn is also shown in Fig. 1.3 [Dea92]. The observed depletion is consistently lower than predicted.

The reason for the lower $^{12}C/^{13}C$ ratio is uncertain. The abundance of the ^{13}C isotope reaches a maximum relatively far from the center of the star. The convective envelope extends completely through this region, effectively mixing all of the ^{13}C isotope with the outer envelope. Thus, the ratio of $^{12}C/^{13}C$ is very insensitive to the depth of the convective envelope. It is also insensitive to the temperature. This can be seen by the insensitivity of the calculated $^{13}C/^{12}C$ ratio to the mass of the star (see Fig. 1.3). If the central temperature were higher, the primary effect would be to move the location of the ^{13}C abundance peak to larger radii, while not substantially changing the total production.

In order to lower the ratio of $^{12}C/^{13}C$, we must either make more ^{13}C or get rid of some of the ^{12}C. One way to dispose of ^{12}C is through mass loss on the main sequence.

However, if we are to change the $^{12}C/^{13}C$ ratio by a significant amount via mass loss, then a significant fraction of the atmosphere of the star must be lost. No mechanism has been demonstrated to account for such mass loss. A more likely scenario for lowering the $^{12}C/^{13}C$ ratio would be through nonconvective mixing on the main sequence. If there were a slow mixing of the material in the atmosphere down to the core of the star, then the production of ^{13}C could be substantially enhanced. Such mixing could be driven by rotation. Several mixing mechanisms have been developed, but they require significant assumptions to be made about the distribution of angular momentum within the star.

The $^{16}O/^{17}O$ ratio in these stars is important for two reasons. First, while the $^{12}C/^{13}C$ ratio shows clear evidence of convection occurring in red giants, it is not sensitive to the depth of convection. The abundance of the ^{17}O isotope peaks much deeper in the stellar interior (see Figure 1.2) than does the ^{13}C isotope. This means that the ratio of $^{16}O/^{17}O$ can be used to fix the depth of convection, and hence the mixing length. The deeper the convection zone, the more ^{17}O is mixed with the atmosphere, and the smaller the $^{16}O/^{17}O$ ratio. Second, the $^{16}O/^{17}O$ ratio is also important because it can be used to constrain models of nonconvective mixing. In addition to changing the $^{12}C/^{13}C$ ratio, nonconvective mixing also changes the ratio of the $^{16}O/^{17}O$ isotopes. In addition to predicting the lower $^{12}C/^{13}C$ abundances, a successful model of nonconvective mixing must also calculate the correct values for the $^{16}O/^{17}O$ ratio.

In the past decade, a significant number of observations of the $^{16}O/^{17}O$ ratio in red giants have been made by Harris and Lambert [Har84a, Har84b, Har88] These observations can be used to test the current models of convection and to set constraints on the types of nonconvective mixing that are occurring on the main sequence. Such a comparison is currently limited by large uncertainties in the rates of the $^{17}O(p,\alpha)^{14}N$ and $^{17}O(p,\gamma)^{18}F$ reactions which are responsible for destroying ^{17}O in the CNO cycle. If these rates are large, then the peak in the abundance of ^{17}O inside the star will be significantly smaller, and ratio of $^{16}O/^{17}O$ seen after dredge up will be larger. On the

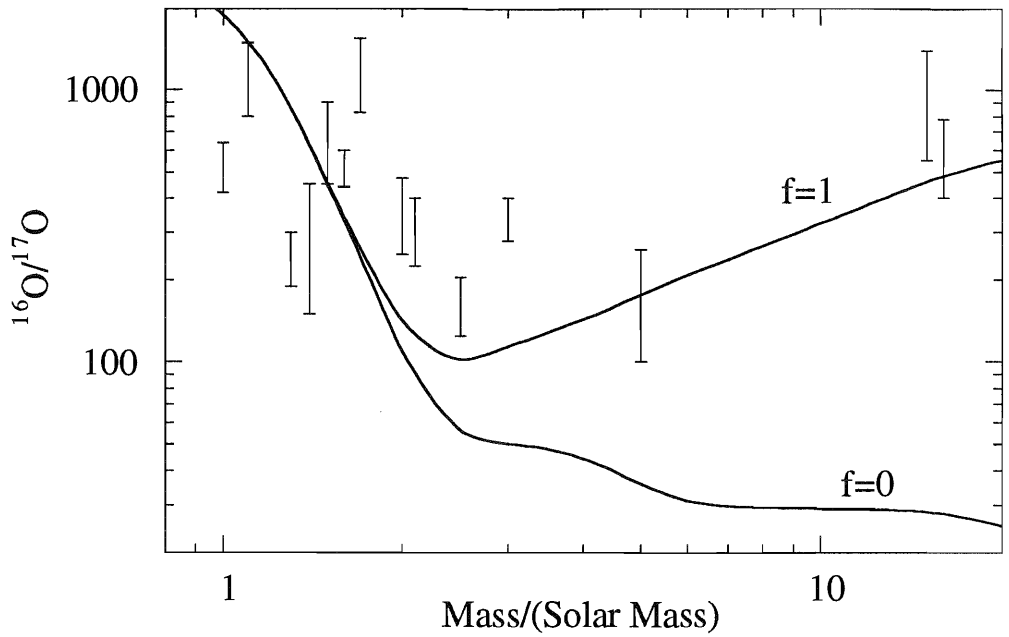

Figure 1.4: Measured $^{16}O/^{17}O$ ratios in 14 red giants [Har84a, Har84b, Har88]. The smooth curves are calculated abundances by Dearborn using the high and low rates for the $^{17}O(p,\alpha)^{14}N$ reaction rate [Dea92].

other hand, if these rates are small, there will be more net ^{17}O produced, and the converse will be true. The relative size of these rates is also important. If the rate of the $^{17}O(p,\alpha)^{14}N$ reaction is significantly less than the rate of the $^{17}O(p,\gamma)^{18}F$ reaction, then the reaction will favor the ^{18}F branch, which increases the possibility of CNO mass loss through the $^{19}F(p,\gamma)^{20}Ne$ reaction.

Observations of the $^{16}O/^{17}O$ ratio for 14 red giants are shown in Figure 1.4. These are the same stars shown in Figure 1.3, with the addition of Alpha Sco, a 15-solar-mass star. Also shown are two calculations by Dearborn using standard stellar evolution, i.e. no mass loss or nonconvective mixing [Dea92]. The higher curve appears to agree with observations, while the lower curve does not. These two theoretical curves were calculated using two different values for the $^{17}O(p,\alpha)^{14}N$ reaction rate, an upper bound (f=1 curve) and a lower bound (f=0 curve). The two curves are the same for low mass stars since the ratio of $^{16}O/^{17}O$ in these stars is limited

by the production of ^{17}O. In heavier stars a significant amount of ^{17}O is produced, and the $^{16}O/^{17}O$ ratio depends strongly on the destruction rate for ^{17}O. If the $^{17}O(p,\alpha)^{14}N$ rate is near its upper bound, then the current stellar models correctly predict the depth of the convective layer. One the other hand, if the $^{17}O(p,\alpha)^{14}N$ reaction rate were closer to its lower bound, then stellar models would over-predict the amount of ^{17}O that is being mixed during dredge up. This would indicate that they convective layer does not extent as deeply as believed. It would also spell trouble for many models of nonconvective mixing. Since the ^{13}C and ^{17}O isotopes have similar mass distributions, it is difficult for mass-flow mechanisms to enhance one (^{13}C) without enhancing the other (^{17}O). Most mixing models which produce a lower $^{12}C/^{13}C$ ratio, also produce a smaller $^{16}O/^{17}O$ ratio. If the $^{17}O(p,\alpha)^{14}N$ reaction rate is much lower than its upper bound, it will make the low $^{12}C/^{13}C$ abundances difficult to explain.

This situation leads Dearborn to conclude that either the $^{17}O(p,\alpha)^{14}N$ reaction rate must be near its upper bound or that the depth of convection on the main sequence is smaller than predicted [Dea92]. Independent calculations by Boothroyd *et al.* [Boo94] and El Eid [Ele94a], using the most current opacities and reaction rates, confirm the results of Dearborn and suggest that the former condition is the correct one. However, this may not be the case. Recent measurements [Ber92] have claimed upper limits on the $^{17}O(p,\alpha)^{14}N$ reaction rate that are significantly below the upper bound of Fowler *et al.* [Fow75]. The purpose of this study is to determine the $^{17}O(p,\alpha)^{14}N$ reaction rate at stellar energies. In doing so, a quantitative treatment of stellar convection, mass-flow and mixing becomes possible.

II. The $^{17}O(p,\alpha)^{14}N$ Reaction Rate: Past Work

It is difficult to measure nuclear cross sections near stellar energies because of the large Coulomb repulsion between nuclei. The cross section for a nuclear reaction is roughly proportional to the probability that the two parties involved will get close enough together to be within the limited range of the nuclear force. This probability is called the *penetrability*, and it decreases exponentially with decreasing energy. To determine the cross section for a reaction at stellar energies, one typically measures the cross section as low in energy as possible, then extrapolates. This extrapolation is made much easier by factoring out the non-nuclear dependence of the cross section. The astrophysical S-factor, S(E) is defined by

$$\sigma(E) = \frac{1}{E} P(E) S(E) \ , \qquad (2.1)$$

where P(E) is the Coulomb penetrability. The S-factor contains all of the nuclear dependence of the cross section, and it is often a smoothly varying function of energy. Instead of extrapolating the exponential cross section it is much easier to extrapolate the typically linear S-factor.

However, the S-factor is not always a smooth function of energy. A resonant nuclear reaction has an S-factor that is strongly energy dependent. A resonance occurs whenever the total energy of the two reactants is very nearly equal to the energy of an excited state in their compound nucleus. The cross section near a resonance may be enhanced by orders of magnitude over the nonresonant cross section within a small energy range. If a cross section is resonant, one cannot simply extrapolate the S-factor

from higher energies, but must either measure the cross section around the resonance energy directly, or one must determine the properties of the resonance by other means.

2.1 The reaction rate for a narrow resonance

In astrophysics we are interested not in the cross section itself but in the thermonuclear reaction rate. The reaction rate, r, is the number of reactions which occur per unit volume per time. It is given by the convolution of the cross section, $\sigma(v)$, and the relative velocity, v, with the Maxwell-Boltzmann velocity distribution. For the generic reaction A(a,b)B, the reaction rate is given by

$$r = N_a N_A \langle \sigma v \rangle = N_a N_A \int_0^\infty \phi(v)\sigma(v)v dv \ , \tag{2.1}$$

where N_a and N_A are the number densities of the reactants in the astrophysical environment and $\phi(v)$ is the Maxwell-Boltzmann velocity distribution. The quantity $\langle \sigma v \rangle$ is the reaction rate per particle pair. When the term "reaction rate" is used by astrophysicists, it is usually this quantity that is intended, since it does not depend on the type of astrophysical environment.

We do not think of the cross section in terms of the relative velocity of the particles, so it is clearer to rewrite the integral in terms of the center-of-mass energy, E,

$$\langle \sigma v \rangle = \left(\frac{8}{\pi\mu}\right)^{1/2} \left(\frac{1}{kT}\right)^{3/2} \int_0^\infty \sigma(E) E \exp\left(-\frac{E}{kT}\right) dE \tag{2.2}$$

where μ is the reduced mass, k is Boltzmann's constant, and T is the temperature. We cannot proceed with our evaluation of the reaction rate until we know something about the form of the nuclear cross section. The cross section for an isolated resonance is described by the Breit-Wigner single-level resonance formula [Mer70]

$$\sigma_{BW}(E) = \pi\lambda\!\!\!^{-2}\omega \frac{\Gamma_a\Gamma_b}{\left(E - E_R\right)^2 + \frac{1}{4}\Gamma_T^2} \ , \tag{2.3}$$

where $\lambda\!\!\!^{-}$ is the wavelength of the incident particle divided by 2π and E_R is the resonance energy. The total and partial widths of the state are Γ_T, Γ_a, and Γ_b, and ω is the statistical spin factor, given by

$$\omega = \frac{(2J+1)}{(2J_a+1)(2J_A+1)} \ , \tag{2.4}$$

where J is the spin of the compound nucleus and J_a and J_A are the spins of the reactant particles.

If the cross section has the Breit-Wigner form, then the reaction rate is given by

$$\langle \sigma v \rangle = \left(\frac{8}{\pi\mu}\right)^{1/2}\left(\frac{1}{kT}\right)^{3/2}\pi\omega\int_0^\infty \lambda\!\!\!^{-2}\frac{\Gamma_a\Gamma_b}{\left(E - E_R\right)^2 + \frac{1}{4}\Gamma_T^2} E\exp\left(-\frac{E}{kT}\right)dE \ . \tag{2.5}$$

In general, this is not an enjoyable expression to evaluate, since the quantities $\lambda\!\!\!^{-}$, Γ_a, Γ_b, and E_R are all functions of energy. However, if the total width of the resonance is small compared to the resonance energy, $\Gamma_T << E_R$, then the Breit-Wigner cross section is a very sharply peaked function of energy. If the other functions contained in the integral, including the Maxwell-Boltzmann distribution, are approximately constant over a range of energies of several resonance widths about the resonance energy, then they can be factored out of the integral and replaced with their values at the resonance energy. Thus

$$\langle \sigma v \rangle = \left(\frac{8\pi}{\mu}\right)^{1/2}\left(\frac{1}{kT}\right)^{3/2}\omega\lambda\!\!\!^{-2}_R\Gamma_a\Gamma_b E_R\exp\left(-\frac{E_R}{kT}\right)\int_0^\infty \frac{1}{\left(E - E_R\right)^2 + \frac{1}{4}\Gamma_T^2}dE \ . \tag{2.6}$$

The integral is now easily evaluated to be $2\pi/\Gamma_T$. Replacing the integral with this value, and using the usual relation between the energy and deBroglie wavelength,

$$E_R = \frac{\hbar^2}{2\mu}\frac{1}{\lambda\!\!\!^{-2}_R}\ , \tag{2.7}$$

we obtain the reaction rate for an isolated narrow resonance,

$$\langle \sigma v \rangle = \left(\frac{2\pi}{\mu kT}\right)^{3/2} \hbar^2 \omega \frac{\Gamma_a \Gamma_b}{\Gamma_T} \exp\left(-\frac{E_R}{kT}\right). \tag{2.8}$$

The quantity $\omega\frac{\Gamma_a\Gamma_b}{\Gamma_T}$ is called the *resonance strength*, and it can be determined by measuring the cross section for the reaction at the resonance energy directly (see Chapter 3). Since these measurements are so difficult, it is often better to try to determine the resonance properties by other means. To determine the reaction rate for a narrow resonance, we need to know the resonance energy, E_R; the total width, Γ_T; the partial widths, Γ_a and Γ_b; and the spin of the compound nucleus, J_A. All of these quantities are properties of the state in the compound nucleus, and they can be probed with other reaction mechanisms.

If there is more than one resonance that contributes to the reaction rate, but the resonance separation is much greater than the width of either resonance, then the cross section can be approximated by the sum of the individual Breit-Wigner cross sections, and the total reaction rate will be given by sum of the reaction rates from the individual resonances. If the resonances are not well-separated, then there may be interference between the two states. Such interference can be either constructive or destructive, and one cannot determine the sign of the interference by the properties of the individual

resonances. In this case, the cross section must be measured in the region of the resonance to determine the sign of the interference.

2.2 The structure of ^{18}F

The $^{17}O(p,\alpha)^{14}N$ reaction is the only resonant reaction in the CNO cycle, and as such, its rate is far more uncertain than any of the other reactions in the cycle. The compound nucleus for this reaction is ^{18}F, and the energies of the excited states in the region of interest have all been accurately measured, primarily through the $^{14}N(\alpha,\gamma)^{18}F$ reaction [Bog89, Ajz87, Ber77]. There are four states that may contribute to the stellar reaction rate. A simplified energy level diagram showing only the states of interest is presented in Figure 2.1. All of the states that are higher in energy than the E_x = 5786 keV state are too narrow to contribute significantly to the reaction rate at stellar energies [Rol73]. The two states at E_x = 5603 and 5605 keV are below the proton threshold, but the high-energy tails of these resonances could make a significant contribution to the stellar reaction rate. The E_x = 5603 keV (1^-) state may also make a contribution through interference with the E_x = 5673 keV (1^-) state.

These states have been extensively studied [Rol73, Mak80, Bog89, Lan89, Ber92]. Except for the proton widths, all of their properties (the spins and parities, total widths, radiative widths and alpha widths) have been accurately determined. The known properties of these states are summarized in Table 2.1. Since the total widths of these states are very nearly equal to the alpha widths, the resonance strength is approximately equal to the proton width. Thus, an accurate determination of the proton widths of these states is essential for determining the reaction rate.

Three studies have contributed information on the proton widths of these states. Rolfs and Rodney populated the states of interest through the direct-capture reaction $^{17}O(p,\gamma)^{18}F$ at E_p = 1.36-1.65 MeV [Rol73, Rol75]. No direct-capture transitions were observed to the states of interest, and an upper limit was set on the proton spectroscopic

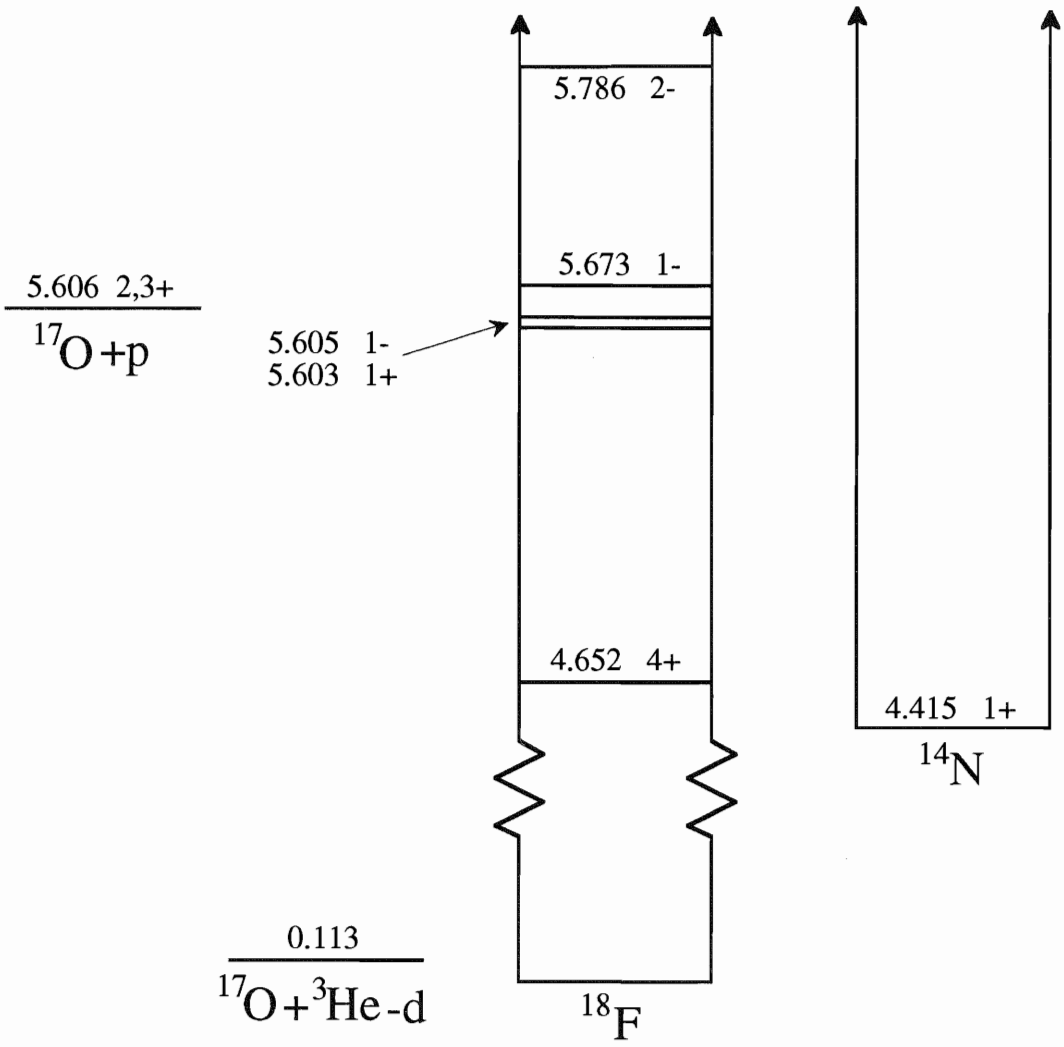

Figure 2.1: Energy level diagram showing states of interest in ^{18}F.

factors for each of these states. These limits are given in Table 2.2. The spectroscopic factor, C^2S_l, is related to the partial width by

$$\Gamma_p = C^2 S_l \Gamma_{sp} \ , \tag{2.9}$$

where Γ_{sp} is the single-particle limit. The single-particle limit is a theoretical upper limit on the width, which can be obtained by assuming a realistic Woods-Saxon type potential. This experiment was performed assuming an energy of E_x = 5668 keV for the 1^- state. Since this experiment was conducted, the excitation energy of the state has been accurately determined to be $E_x = 5672.57 \pm 0.32$ keV [Bog89]. When the correct value

Table 2.1: Known properties of the states of interest in ^{18}F.
(a = [Ajz87], b = [Mak80], c = [Rol73], d = [Bog89])

Energy (keV)	J^{π}	Γ_T (eV)	Γ_α(eV)	Γ_γ(eV)
5603.4 ± 0.3^a	1^+	43.4 ± 1.6^b	42.8 ± 1.6^b	0.48 ± 0.05^b
5604.9 ± 0.3^a	1^-	$\leq 1200^a$	$\leq 1200^a$	0.87 ± 0.07^a
5672.6 ± 0.3^d	1^-	131.4 ± 5^b	130 ± 5^b	1.4 ± 0.3^a
5786 ± 2.4^a	2^-	0.044 ± 0.03^a	0.022^c	0.022^c

for the resonance energy is used, it is found that the gamma-ray line from direct capture to the E_x = 5673 keV state is obscured by the second escape peak from direct capture into the E_x = 4.652 keV state. Thus, a limit on the proton width for the E_x = 5673 keV state cannot be determined from a study of the $^{17}O(p,\gamma)^{18}F$ reaction.

The reaction rates which are used in nearly all stellar models are the rates compiled by Fowler and collaborators [Fow75, Har83, Cau89]. The resonant rate for the $^{17}O(p,\alpha)^{14}N$ reaction as given in these references is based upon the results of the Rolfs and Rodney measurement. Uncertain reaction rates are quoted with a scaling factor. In the case of an upper limit, this factor varies from 0 to 1. The $^{17}O(p,\alpha)^{14}N$ reaction rate as compiled by Fowler *et al.* has significant contributions from three sources. Two contributions are the resonant reaction rates from the 5673-keV and 5786-keV levels. Both of these rates are quoted with a scaling factor ranging from 0 to 1, and the upper limit is derived from the Rolfs and Rodney experiment. The third contribution is from the nonresonant reaction rate which is known with relative certainty. It should be noted that the contributions to the reaction rate from the subthreshold states are rendered negligible by the upper limits given. Each of these contributions to the reaction rate is shown in Figure 2.2. Since only upper bounds are known for the resonant reactions, the lower bound to the reaction rate will be the rate

Table 2.2: Spectroscopic factors for the states of interest.

E_x (keV)	l	C^2S_l [Rol75]	C^2S_l [Lan89]
5603	2	≤ 0.002	0.12 ± 0.04
	4	≤ 0.06	----------
5605	1	≤ 0.0003	≤ 0.020
	3	≤ 0.009	≤ 0.024
5673	1	(≤ 0.0001)	0.006 ± 0.003
	3	(≤ 0.003)	----------
5786	1	≤ 0.0006	≤ 0.002
	3	≤ 0.002	≤ 0.004

from direct (nonresonant) reactions. The upper limit will effectively be given by the upper limit from the 5673-keV state.

The fact that the upper limit on the 5673-keV state is invalid is significant, since this resonance dominates the reaction rate. The two calculations by Dearborn shown in Fig. 1.5 were made with the strength of the 5673-keV resonance at its upper limit (f=1 curve) and with the strength of the resonance set to 0 (f=0 curve). This means that the curve for the upper bound is set arbitrarily.

Landre *et al.* populated the states of interest through the $^{17}O(^3He,d)^{18}F$ reaction using a 15-MeV ^3He beam [Lan89]. Angular distributions of the deuterons from the states of interest were measured using a split-pole magnetic spectrometer. The spectroscopic factors for the states were determined by fitting the measured differential cross sections with distributions calculated using the distorted-wave Born approximation. The results are also given in Table 2.2.

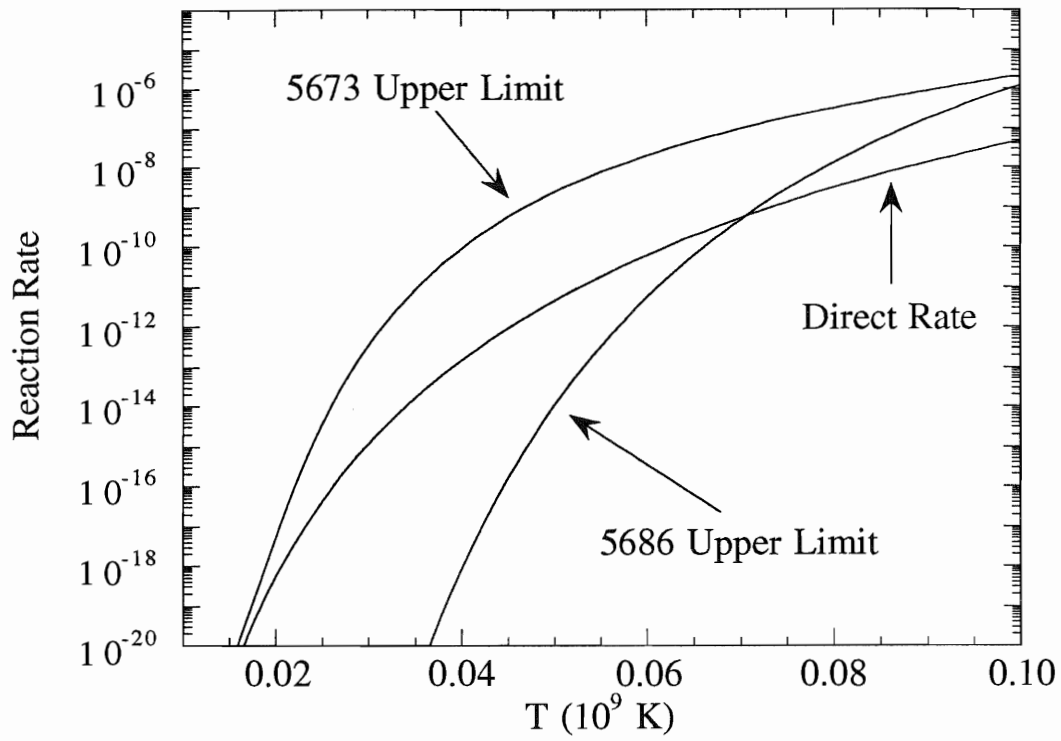

Figure 2.2: Contributions to the $^{17}O(p,\alpha)^{14}N$ reaction rate as given by Fowler *et al.* [Fow75].

Because of the model-dependent nature of these results, the errors on the deduced spectroscopic factors are large. However, even with the large error bars, these results imply a much larger $^{17}O(p,\alpha)^{14}N$ reaction rate than was previously believed. The resonance strength of the 5673-keV resonance was found to be 60 times greater than the upper limit set in the Rolfs and Rodney experiment. The strength of the 5603-keV resonance was also found to be 60 times greater. However, there is no reason not to believe the Rolfs and Rodney result for the 5603-keV state. These two measurements are in disagreement, but if the strength for the 5673-keV state measured by Landre *et al.* is correct, the contribution to the reaction rate from the 5603-keV state would be negligible at all but the lowest temperatures. For the states at 5605 keV and 5786 keV, Landre *et al.* was able only to set an upper limit on the width, but this limit confirms that

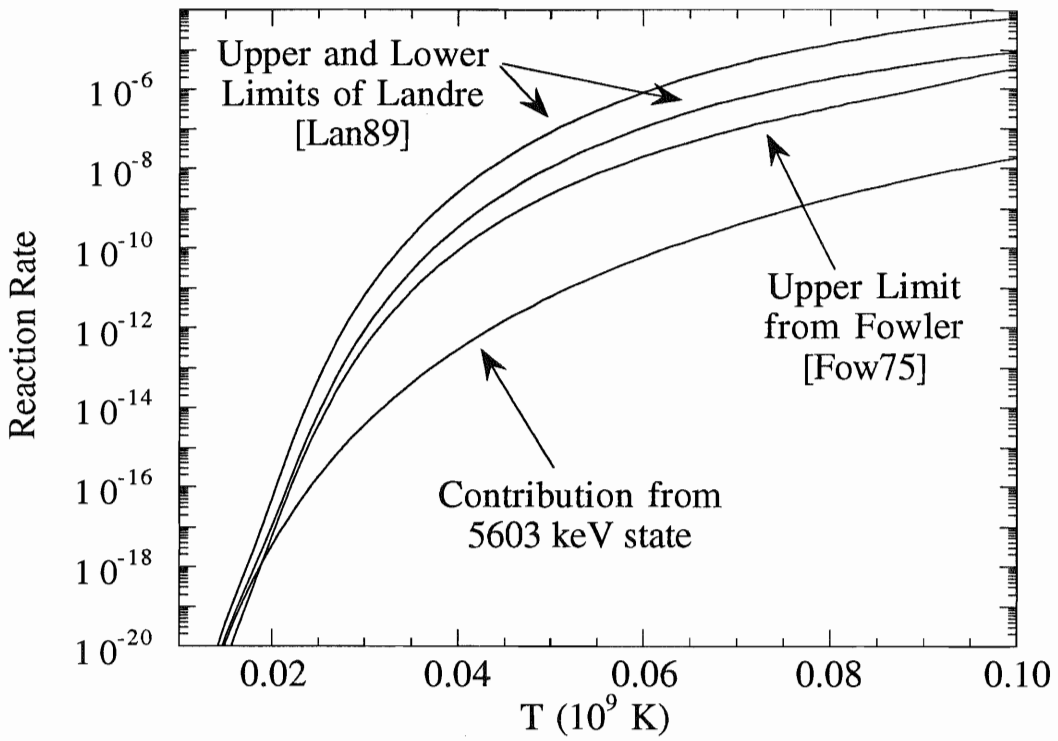

Figure 2.3: The $^{17}O(p,\alpha)^{14}N$ reaction rate as given by Landre [Lan89].

the contribution to the reaction rate from the 5605-keV level is negligible, and that the contribution to the 5786-keV state is negligible everywhere except at high temperatures. The upper and lower bounds for the $^{17}O(p,\alpha)^{14}N$ reaction rate, given the range of widths for the 5673-keV state as determined by Landre, are shown in Fig. 2.3. The upper limit from the tabulated rates of Fowler is shown for comparison.

A direct measurement of the strength of the E_x = 5673 keV resonance in the $^{17}O(p,\alpha)^{14}N$ reaction was attempted by Berheide *et al.* [Ber92]. The count rate from this reaction is very low because of the large Coulomb barrier at E_p = 70 keV. Intense beams of protons were used with thick ^{17}O enriched Ta_2O_5 targets and large-solid-angle detectors to maximize the count rate. A total of 483 C of charge was accumulated on target, but the resonance was not seen. An upper limit on the number of alphas, N_α, was determined from the background counts in the region of interest, N_c, by

$$N_\alpha \leq \sqrt{2N_c} \ . \tag{2.10}$$

An upper limit on the proton width of the 5673-keV state was thereby estimated to be

$$\Gamma_p \leq 3 \text{ neV } (1\sigma) \ . \tag{2.11}$$

This is in contradiction to the proton width of the state as determined by the $^{17}O(^3He,d)^{18}F$ reaction [Lan89] to be

$$\Gamma_p = 71^{+40}_{-57} \text{ neV} \ . \tag{2.12}$$

The upper limit set on the resonance strength set by the Berheide *et al.* measurement is almost the same as the erroneous upper limit set in the original Rolfs and Rodney experiment. Thus, the upper limit set on the reaction rate as determined by this measurement will be close to the original upper limit as given by Fowler *et al.* [Fow75], which is less than the lower limit set by Landre *et al.* Given these results, it is not clear what the strength of the 5673-keV resonance is, but it is clear that the rate of the $^{17}O(p,\alpha)^{14}N$ reaction is dominated by its value.

III. The Experimental Design

We have performed a direct measurement of the alpha-particle yield from the E_p = 70 keV resonance in the $^{17}O(p,\alpha)^{14}N$ reaction, and from the measured yield we have deduced the proton width of the E_x = 5.673 MeV state in ^{18}F. In order to make a direct measurement of such a small resonance strength, it was important to maximize the yield from the state of interest and to decrease the yield from other sources. In this chapter we discuss the factors that affect the measured yield and how we designed the experiment to maximize the counts versus background.

3.1 The measured yield from a narrow resonance

When a projectile enters a target it loses energy through successive collisions with atoms and nuclei. It is in some of these collisions that the nuclear reactions of interest take place. Owing to the energy loss in the target, the yield that is measured in a charged-particle induced nuclear reaction is always an integrated yield over some range of beam energies. The measured yield, N_b, from the nuclear reaction A(a,b)B occurring in some thin slice of the target of thickness dx is given by

$$N_b = \Omega N_a \sigma(E) W(\theta,E) \eta_A dx \ , \qquad (3.1)$$

where Ω is the detector efficiency, N_a is the number of incident particles, $\sigma(E)$ is the nuclear cross section, $W(\theta,E)$ is the angular distribution of the scattered particles, and η_A is the number density of A atoms.

The total yield from a finite thickness of target is obtained by integrating Eqn. 3.1. Instead of integrating over the thickness, it is more convenient to transform the

integral to an integral over energy, since the cross section is a function of energy. The quantity $\eta_A dx$ is the number of atoms of A per unit area in this thin section of target. This can be equivalently expressed as

$$\frac{dE}{\varepsilon_{\text{eff}}(E)} = \eta_A dx \ , \tag{3.2}$$

where $\varepsilon_{\text{eff}}(E)$ is the effective stopping cross section, which is the defined as the amount of energy lost by the particle in passing through a unit areal density of the target atoms. Its typical units are eV/(atoms/cm^2), and it is a function of the energy of the particle. Substituting Eqn. 3.2 into Eqn. 3.1 and integrating over the thickness of the target, gives the total reaction yield. If the beam current is not substantially reduced in the target, and the detector efficiency is constant over the range of energies of the particles being detected, then the total yield may be expressed as

$$N_b = \Omega N_a \int \frac{\sigma(E)}{\varepsilon_{\text{eff}}(E)} W(\theta, E) dE \ , \tag{3.3}$$

where the integral extends over the range of beam energies that applies to the target thickness.

If the cross section is described by the Breit-Wigner cross section (Eqn. 2.3) for an isolated resonance, then the total yield becomes

$$N_b = \Omega N_a \pi \omega \int \frac{\lambda\!\!\!^{-2} W(\theta, E)}{\varepsilon_{\text{eff}}(E)} \frac{\Gamma_a \Gamma_b}{(E - E_R)^2 + \frac{1}{4}\Gamma_T^2} dE \ . \tag{3.4}$$

Although the quantities $\lambda\!\!\!^{-}$, ε_{eff}, Γ_a, Γ_b, E_R, and $W(\theta,E)$ are all functions of energy, they are typically slowly varying functions of energy. Thus they can be replaced by their values at the resonance energy and factored out of the integral. This leaves

$$N_b = \Omega N_a \pi \omega \lambda\!\!\!^{-2} \frac{W(\theta, E_R)}{\varepsilon_{\text{eff}}(E_R)} \Gamma_a \Gamma_b \int \frac{dE}{(E - E_R)^2 + \frac{1}{4}\Gamma_T^2} \,. \tag{3.5}$$

The maximum yield is obtained by integrating over all possible energies. This is called the thick target yield, and is given by

$$N_b = \frac{1}{2} \Omega N_a \omega \lambda\!\!\!^{-2} \frac{1}{\varepsilon_{\text{eff}}(E_R)} \frac{\Gamma_a \Gamma_b}{\Gamma_T} \tag{3.6}$$

Since the integrand in Eqn. 3.5 falls off rather quickly away from the resonance energy, the thick target yield is a good approximation even if the target thickness is only a few times Γ_T. The ratio of the integrated yield over a range of energies to the thick target yield is shown in Fig. 3.1. The yield has been integrated from an energy which is effectively infinitely high above the resonance to a final energy, E_f. The ratio is plotted

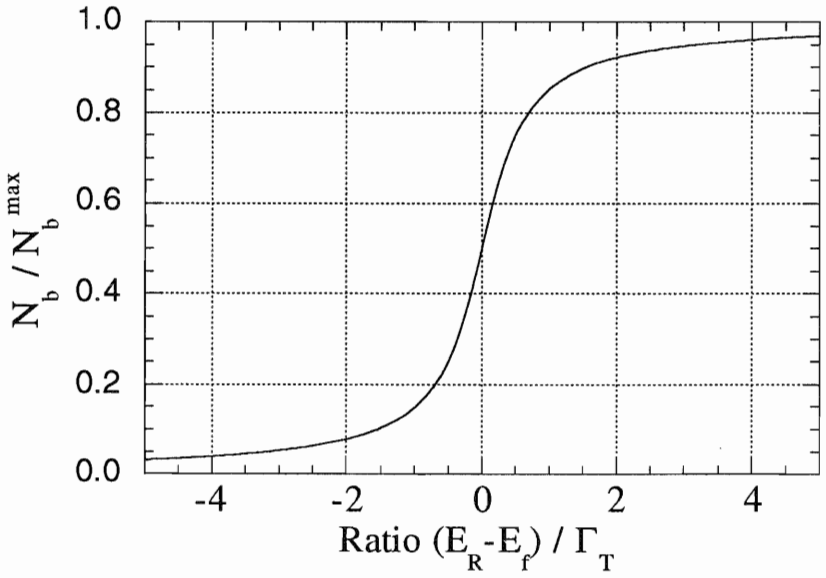

Figure 3.1: The ratio of the yield from a narrow resonance to the total yield as a function of target thickness.

against the final energy in relation to the resonance energy. About 90% of the thick target yield can be obtained from a target whose width is only 6 times the resonance width, if the incident beam energy is $E_R + 3\Gamma_T$.

The total width of the E_x = 5673 keV resonance in ^{18}F is 131.4 eV. Protons with an energy of 70 keV lose hundreds of eV per nanometer in solid matter. Thus any target which we produce will be orders of magnitude thicker than the width of the resonance. Also, this width is only 0.2% of the resonance energy, and the quantities λ, ε, Γ_p, and Γ_α do not vary significantly over such a short energy range. Therefore Eqn. 3.6 is valid for the measured yield from the E_x = 5673-keV resonance in the $^{17}O(p,\alpha)^{14}N$ reaction.

3.2 The Low Energy Astrophysics Facility

There are only three quantities affecting the yield from a narrow resonance over which we have experimental control. They are the detection efficiency, Ω, the number of incident particles, N_a, and the effective stopping cross section, ε_{eff}. Because of the small proton width of the E_x = 5673 keV state, it was very important that we maximize the yield by optimizing each of these quantities. Maximum yield is obtained by increasing the number of incident particles and the detection efficiency, while decreasing the effective stopping cross section. In addition to increasing the yield, it is also important to reduce the background from other sources. The lower the background rate, the smaller the yield to which we are experimentally sensitive.

The experiment was conducted at Triangle Universities Nuclear Laboratory (TUNL) on the Duke University campus using an unpolarized beam from the TUNL Atomic Beam Polarized Ion Source (ABPIS). A schematic of the low-energy bay at TUNL is shown in Figure 3.2. Our beam line was constructed on the 90°-right port of the TUNL ABPIS inflection magnet. Protons of energy up to 80 keV are available directly from the polarized source.

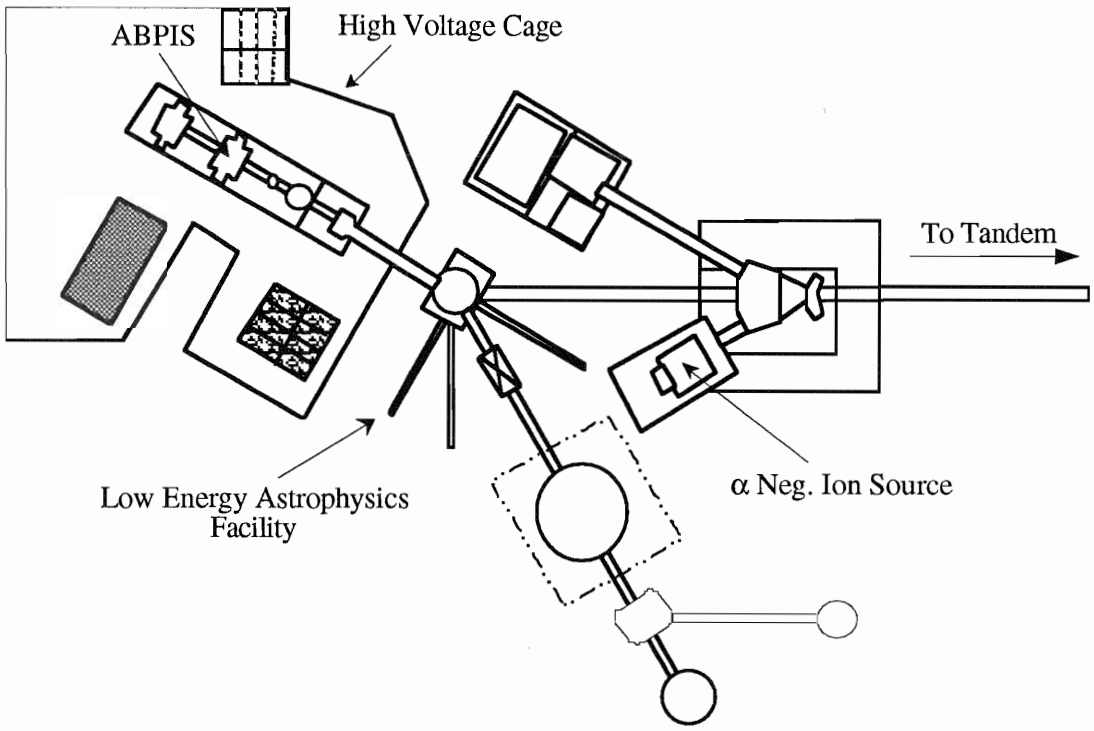

Figure 3.2: Layout of the low-energy bay at TUNL.

The yield depends upon the total number of incident particles and not the beam current, but it was important to maximize the beam current, since a major contribution to the background was from sources that were not beam related, i.e. cosmic rays and natural radioactivity. Increasing the beam current increased the yield, but did not increase the background from these sources. It was also important that the beam currents be high so that a sufficient charge could be collected in a reasonable amount of beam time.

Our primary objective in construction of the beam line was to obtain the highest beam currents possible on target. Optics calculations indicated that there would be a large divergence of the beam from the 90° bend in the inflection magnet. We compensated for this by placing a quadrupole focusing device immediately after the inflection magnet. Following the quadrupole, there is a drift space of about 0.7 m

before the beam enters a nickel-plated copper shroud which collimates the beam. The shroud had a diameter of 2.5 cm and a length of 0.5 m. A circular beam collimator with an aperture size of 1.2 cm was located 8 cm from the downstream end of the shroud. The 2.5 cm entrance to the shroud and the 1.2 cm collimator served as the beam defining apertures. The beam exits the shroud inside the target chamber less than 3 cm from the target. A schematic of the target chamber showing the shroud and beam collimator is shown in Figure 3.3. With this arrangement, we were able to get 90% transmission from the ABPIS beam stop, located about 1 meter before the inflection magnet, to target.

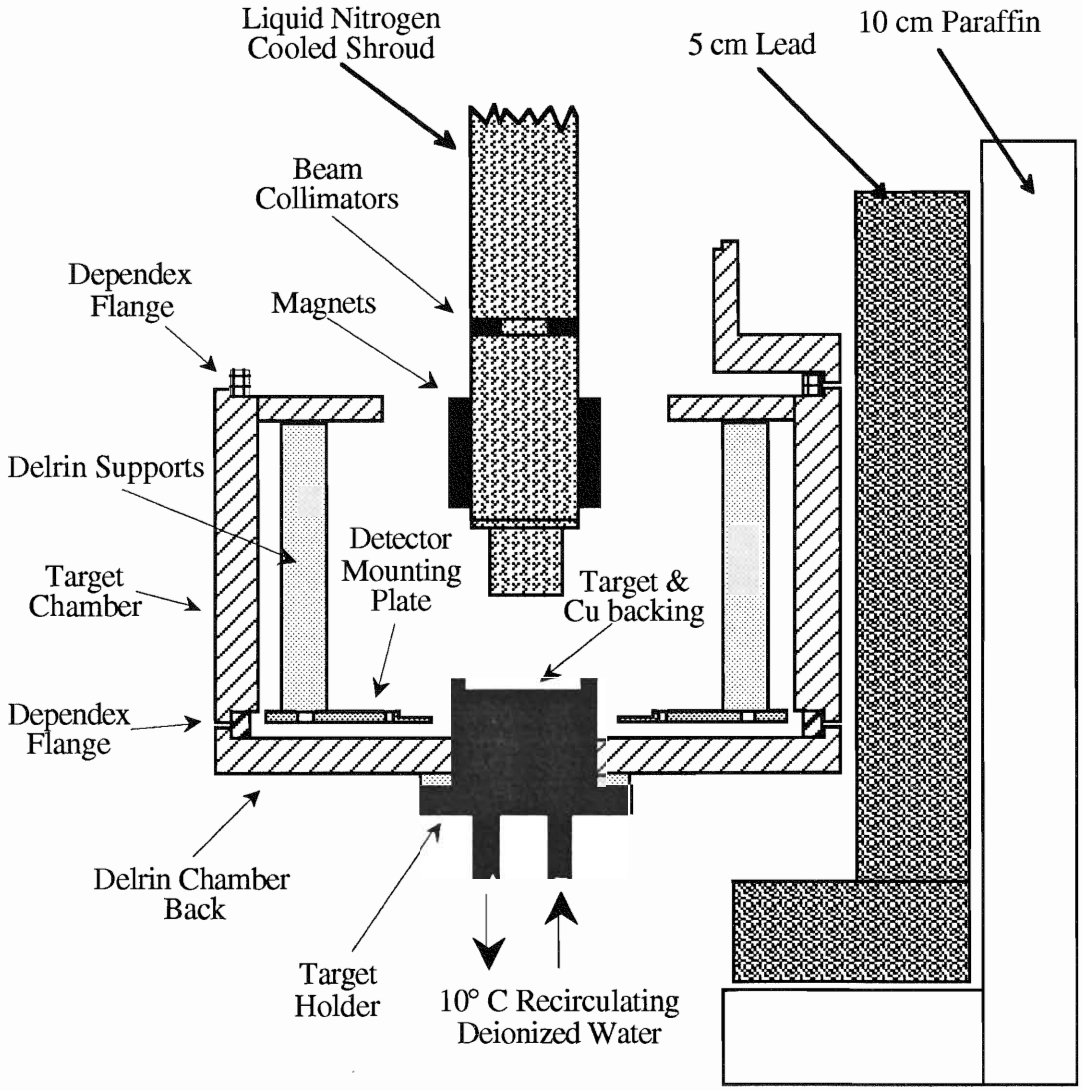

Figure 3.3: Schematic of the target chamber. The shielding is shown only on one side of the chamber.

John Dunham and Tom Clegg worked closely with us to try to maximize the beam current from the polarized source. Various changes in the beam optics of the polarized source were attempted, including the installation of gridded extraction lenses and the installation of a quartz containment tube for the ECR RF ionizer. These drastic changes to the optics of the polarized source resulted in either marginally better or worse beam currents. Ultimately, we returned to the original optics of the polarized source.

Significant gains in beam current were gradually achieved as we learned how to optimize the operating parameters for unpolarized beams. The most important elements were the ECR RF ionizer and extraction lenses. We ran the source by closing off the atomic beam system, and bleeding gas directly into the ionizer. We found that maximum beam current was achieved by bleeding gas at as fast as allowed by the leak valve, a setting of 1000 sccm. With such high pressures in the ionizer, it was necessary to run the forward power at significantly higher settings than normal. Typical polarized source operating parameters are given in Table 3.1. Typical beam currents on target ranged from 400-450 μA over the course of the experiment. This represented an increase of 250% over the beam currents that we first achieved on target.

The target was connected to a current integrator through a battery which biased the target to +300 V relative to ground, i.e. the scattering chamber. This bias suppressed the scattering of electrons from the target. Our beam current integration was not sensitive to the amount of bias on the target. We reduced the bias to +90 V and found no measurable change in the beam current. An added bias of -300 V to the shroud also did not change the beam current measurably.

We checked the accuracy of our beam current integration by mounting a Faraday cup onto a target holder and comparing the integrated current with the current as measured in our normal configuration (see Figure 3.3). Since we had to bring the target chamber up to air to change from a normal target to the Faraday cup, there was a time delay of about 10 minutes between when the measurements were made in each

Table 3.1: Typical ABPIS operating parameters at E_p = 80 keV.

Source Parameter	Typical Value
Gas Flow	1000 sccm
HG4 Pressure	3 x 10^{-6} Torr
HG5 Pressure	1.5 x 10^{-6} Torr
TWTA Pot. Setting	2.97
Ionizer Coil C_1	125 A
Ionizer Coil C_2	162 A
Ionizer Coil C_3	98 A
ECR RF Ionizer Forward Power Setting	-0.3590
ECR RF Ionizer Frequency Control	2.952 V
Cs Oven Temp	90° C
Lens 1	10 kV ; 1 mA
Lens 2	0.2 kV ; 6 mA
Lens 3	0.3 kV ; 3 mA
Lens 4	0.7 kV ; 26 mA
Lens 5	0.7 kV ; 3 mA
Lens 6	3.5 kV ; 0 mA
Lens 7	12 kV ; 1 mA
Wien filter Magnetic Field Current	80 A
Wien filter Electric Field Setting (A)	5.84
Wien filter Electric Field Setting (B)	5.91
Beam Current on PIS Cup	0.50 mA
Beam Current on Target	0.44 mA

configuration. To be sure that any changes in beam current were not the result of drifts in the beam current from the polarized source, we changed from the normal target to the Faraday cup then back to the target several times. The beam current was measured in many short (30 second) intervals in each configuration. The results of the test are shown in Figure 3.4. There were three sets of runs taken with the Faraday cup and three with the regular target. The Faraday cup was assumed to measure the real beam

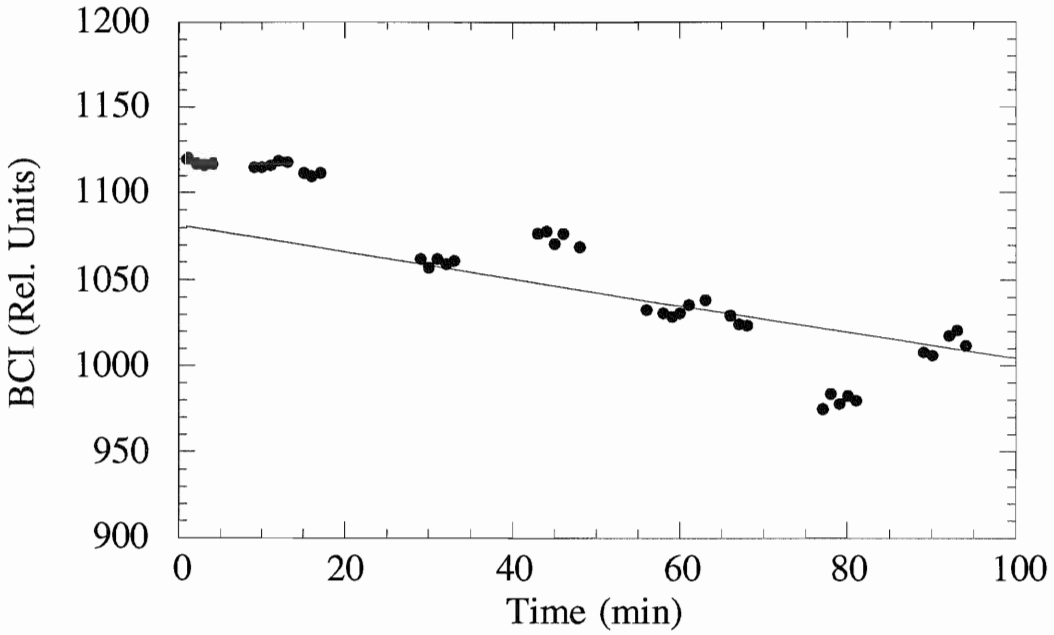

Figure 3.4: Results of beam current integration test using a Faraday cup. The data points which fall around the line are points taken with the Faraday cup. The other groups of points were taken with a regular target. Note the y-axis offset.

current, and a linear fit to these sets of measurements is shown. There was a net downward trend in the measured beam current with time. The beam current measured on targets fluctuated within about 3% of the value measured with the Faraday cup. While this may be caused by non-linear fluctuations in the beam current from the polarized source, we adopt 3% as the uncertainty in our beam current integration.

There is one additional effect which was not addressed by this test. It is possible that some beam may be scattered off of our beam collimators and reach the target, but with a significantly reduced energy. If the energy of these particles is less than the resonance energy, then they will be integrated, but will not contribute to the yield. This spurious current should certainly be less than the total current on the entire shroud. The current on the shroud was about 10% of the beam current on target. We estimate the error in the beam current from scattered beam to be 6% of the total beam current. This error is only in the direction of lower beam current. We add this error in quadrature

with the 3% error obtained from the previous test, and adopt a total error in the beam current integration, σ_I, of

$$\sigma_I = \begin{matrix} +3\% \\ -7\% \end{matrix} . \tag{3.7}$$

It was important to raise the beam current because there was a significant contribution to the background that was not beam related. We found that this background could be lowered by surrounding the chamber with lead and paraffin. A steel support table was constructed under the target chamber, and a 5 cm-thick lead "house" was stacked around the target chamber. The lead surrounded the chamber on both sides and on the top and bottom. The lead was then surrounded by a 10 cm-thick layer of paraffin (see Figure 3.3). It was found that this reduced the nonbeam related background by about a factor of 2. We tried doubling the thickness of this shielding, but this did not reduced the background further.

Besides reducing the background and increasing the amount of charge collected, it was important to have a low effective stopping power for the targets combined with a high detection efficiency. Much effort was expended in optimizing both of these parameters. We discuss the development of the targets and detection system in detail in the next two chapters.

IV. The Targets

4.1 Possible target materials

There were three important considerations in selecting a target material for this measurement. Foremost was the relative concentration of ^{17}O. The yield, given by Eqn. 3.8, is inversely proportional to the effective stopping cross section, which is the energy lost per areal density of ^{17}O atoms as the projectile traverses the target. Consider a target which is divided into thin slices, each containing the same number of ^{17}O atoms/cm^2, as illustrated in Figure 4.1. The effective stopping power is proportional to the energy lost by the particle in each of these regions. For a specific particle energy, the effective stopping power for the first two regions, Δ_1 and Δ_2, is the same (and likewise for Δ_3 and Δ_4), since the particle will experience the same collisions in these regions. The effective stopping power only depends on the composition and not the density. However, the effective stopping power for the last two regions is greater than for the first two regions, since the particle will lose additional energy in collisions with the inert atoms. As expected, the maximum yield is obtained for a target that is pure ^{17}O. In this case the effective stopping cross section is just the elemental stopping cross section for oxygen, ε_O. At $E_p = 70$ keV this is given by

$$\varepsilon_O\left(E_p = 70 \text{ keV}\right) = 16.7 \frac{\text{eV}}{10^{15} \text{ atoms/cm}^2} \tag{4.1}$$

from the stopping power tables of Anderson and Ziegler [And77a].

Maximum yield requires a pure ^{17}O gas target. However, standard gas cells cannot be used in measurements at such low energies because of the large energy loss in the windows of the cell. Even in unrealistically thin windows (2 μm havar perhaps), the

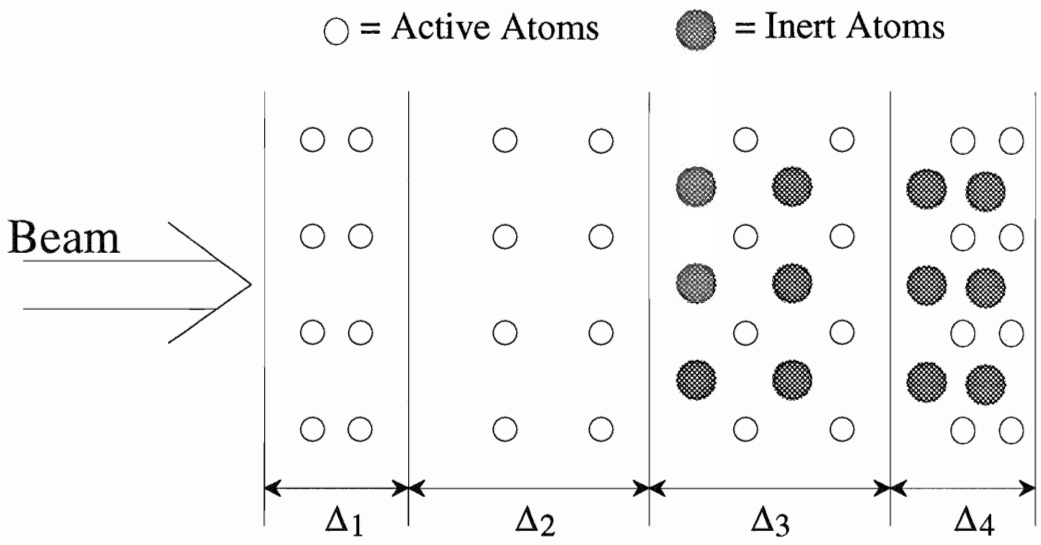

Figure 4.1: Illustration of the effective stopping cross section.

energy loss in the foil is several hundred keV, and the energy straggling is almost as large as the resonance energy itself. This problem has been overcome by the use of recirculating, windowless, differentially-pumped gas jet targets [Rol88]. A measurement was attempted using such a target by the Bochum group [Ber92], but it was found that oxygen was rapidly lost from the system, probably from oxidation of the metallic inner surfaces. Owing to the extreme expense of enriched ^{17}O gas ($7,000 per liter), such targets are not economical.

The alternative to gas targets is to use a solid target made of some compound containing ^{17}O. The stopping cross section for these targets is larger because of the presence of inert atoms, but it is much easier to control their thickness. Bragg's rule states that the stopping cross section for a compound target is given in first approximation by just adding the elemental stopping cross sections weighted by their stoichiometric coefficients. In this approximation, the effective stopping cross section, ε_{eff}, will be given by

$$\varepsilon_{\text{eff}} = \sum_j r_j \varepsilon_j = \sum \frac{\eta_j}{\eta_{17}} \varepsilon_j \ , \qquad (4.2)$$

where ε_j is the stopping cross section for element j, r_j is the ratio of the number density of atoms of isotope j to the number density of atoms of ^{17}O, and the sum extends over all of the isotopes in the target. Bragg's rule treats the target as if it was a mixture of atoms rather than a molecular compound. It neglects any effects that arise from the molecular structure of the target. Erroneous results for the stopping cross section can be obtained for crystalline substances where there exists regular structural patterns over many atomic spacings; however, we will assume the validity of Bragg's rule in calculating stopping cross sections for compound targets.

Three different metallic-oxide target materials were studied for use in this measurement. They were aluminum-oxide (Al_2O_3), tungsten-oxide (WO_3), and tantalum-oxide (Ta_2O_5). The effective stopping cross section for each of these targets is listed in Table 4.1. These three compounds have similar effective stopping powers, and thus will have similar yields. Although the ratio of oxygen to inert atoms in aluminum-oxide is smaller than for the other compounds (1.5 as compared to 3.0 or 2.5), the atomic stopping cross section for aluminum is significantly less than for tantalum or tungsten. The stopping cross section for aluminum-oxide was also calculated assuming an enrichment of 100% ^{17}O, while the stopping cross sections for tantalum-oxide and tungsten-oxide were calculated assuming an enrichment of 77% ^{17}O. This is because the aluminum-oxide targets that we considered were implanted targets, whereas the tantalum-oxide and tungsten-oxide were produced by oxidation, and 77% ^{17}O is the highest enrichment commercially available.

The second property that was very important in the selection of a target material was its resiliency. The targets were required to hold up to beam currents of 450 μA for the better part of a day without a significant change in target stoichiometry. At proton

Table 4.1: Effective stopping cross sections for the three targets studied.

Target	$\varepsilon_{eff}\left(\frac{eV}{(10^{15}\text{atoms/cm}^2)}\right)$	^{17}O Enrichment
Al_2O_3	31	100%
WO_3	39	77%
Ta_2O_5	36	77%

energies of 75 keV and beam currents of 450 μA, 34 W of power are dumped into the first couple of microns of the target. Although the targets were mounted against a copper backing that was cooled with 10° C water, it was uncertain whether they would conduct the heat away from the bombardment region quickly enough to prevent significant heating and possible loss of oxygen.

In addition to local heating, sputtering was also a potential source of target loss. The sputtering yield from a compound depends upon the molecular properties of the substance [Bet80]. However, if we assume that the sputtering rate will be limited by the rate of the heavier inert atoms in the target, then we can get a rough estimate of the sputtering rates of each of the targets from the sputtering yields of monatomic aluminum, tungsten and tantalum. The sputtering yields from each of these elements from 75 keV protons are all about $4x10^{-4}$ atoms/ion [Mat84]. If we take a conservative estimate of the sputtering yield to be 10^{-3} inert atoms/ion then we find a sputtering rate of at most 0.01 μm/hr at our beam currents. While this is not an insignificant sputtering rate, it is small in comparison to our target thickness which is on the order of a micron. We anticipated local heating in the front surface of the target and the effects of hydrogen implantation to be the principle factors in changing the target stoichiometry, but we carefully checked all three target materials for their resiliency to oxygen loss by any means.

The third criterion in choosing a target material was the concentration of contaminants. Proton induced reactions on ^{6}Li and ^{10}B, even if found in trace quantities, could produce significant backgrounds at the energies of interest. Thus, it was very important to test each of our potential targets for stability of oxygen composition and for contamination from other light isotopes.

4.2 Cold neutron depth profiling

4.2.1 General description

We tested these three target materials using two methods. The primary technique was Cold Neutron Depth Profiling (CNDP) which we performed at the Cold Neutron Research Facility of the National Institute of Standards and Technology (NIST), Gaithersburg, MD [Dow93]. A schematic of the CNDP set-up is shown in Figure 4.2. Neutrons from the heavy-water reactor at NIST are moderated by a D_2O ice cold source which produces neutron fluxes of 10^9 neutrons/cm^2/s at a temperature of 65 K. The density of certain nuclear isotopes as a function of depth in a target can be determined by utilizing this beam to study neutron induced charged particle reactions, such as the $^{17}O(n,\alpha)^{14}C$ reaction. A summary of some light isotopes which can be profiled by CNDP, and are of interest to the current experiment, is shown in Table 4.2. In addition to providing an accurate determination of the ^{17}O concentration in the target, CNDP is also sensitive to lithium and boron contamination through the $^{6}Li(n,\alpha)^{3}H$ and $^{10}B(n,\alpha)^{7}Li$ reactions.

Since there is little neutron attenuation in the target, the neutron induced reactions occur throughout the target. The charged particles emitted in these reactions lose energy in leaving the target, and by measuring the energy spectrum of these charged particles, the isotopic composition of the first few microns on the surface of the sample can be determined simultaneously. The small neutron attenuation also allows for two samples to be mounted back-to-back and profiled at once, as shown in Figure 4.2. A slight

Figure 4.2: Schematic representation of the NIST CNDP facility.

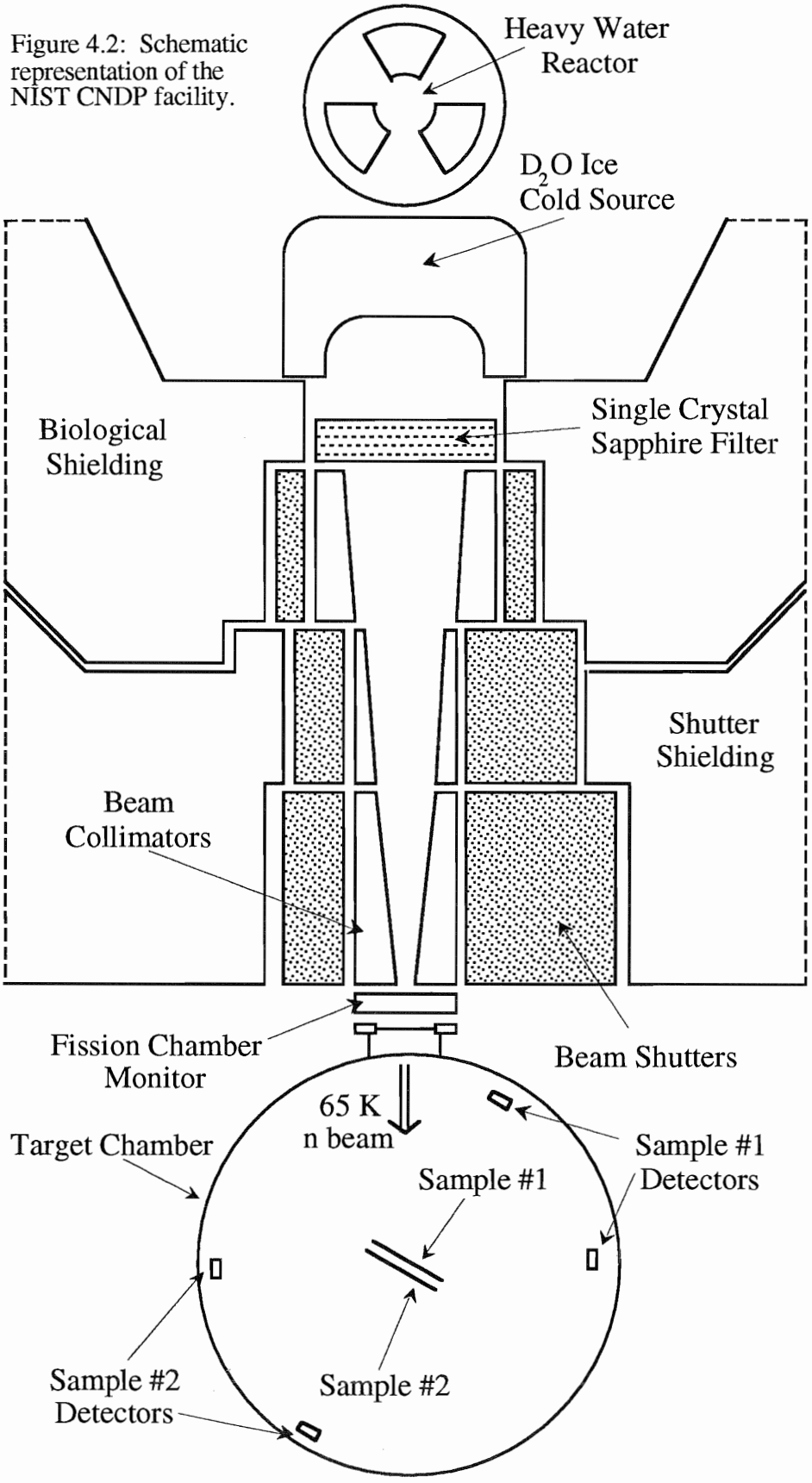

Table 4.2: Summary of light isotopes measured by CNDP.

Isotope	Reaction	Cross Section (barns)	Particle Energy α (keV)	Recoil (keV)
^{6}Li	^{6}Li(n,α)^{3}H	940	2055	2727
^{10}B	^{10}B(n,α)^{7}Li	3837	1472 (94%)	840
			1776 (6%)	1013
^{17}O	^{17}O(n,α)^{14}C	0.24	1413	404

correction for neutron attenuation was applied to the second sample. A fission-chamber monitor was mounted just upstream of the CNDP target chamber to serve as a relative measure of the neutron flux. Because of the high intensity and extremely low neutron energy of the NIST cold neutron source, it has been the only facility able to measure oxygen compositions by CNDP.

The energy of a charged particle emitted in a neutron induced reaction is related to its detected energy by the stopping power of the target, dE/dx. If the energy of the emitted particle is E_0, and the reaction occurs at a depth d, then the detected energy of the particle, E(x), is given by

$$E(x) = E_0 - \int_0^d \frac{dE}{dx} dx \ . \tag{4.3}$$

The stopping power is the energy lost per distance traveled in the target. Since the stopping power depends upon the composition, one must assume a composition for the target in order to relate the energy of the observed alphas to a depth in the target. However, after assuming a composition, one can then determine the number of counts as a function of depth. This can then be used to determine the density of ^{17}O atoms in the target. If the measured density does not agree with the composition assumed in

calculating the stopping power, then the composition is changed, and the processes repeated until a self-consistent composition is found. Since one typically has a good guess what the target composition is before doing the profile, this is not a laborious process.

In order to arrive at a determination of the ^{17}O density with depth, the CNDP system must be calibrated in two ways. An absolute energy calibration for the detector is performed using a sample of borosilicate glass. There are two alpha groups seen from the $^{10}B(n,\alpha)^{7}Li$ reaction, since the reaction can proceed either to the ground state or first excited state of ^{7}Li (see Table 4.2). The known energies and measured channels for these two groups are used as an absolute gain calibration. This allows the number of counts per energy, N_A/E, to be determined as a function of particle energy.

The neutron flux and efficiency of the detection system must also be calibrated. The fission-chamber monitor serves as a relative measure of the neutron flux between runs, but an absolute calibration was made using a ^{10}B standard of known composition. By comparison to the standard run, the number of atoms of isotope A per area per energy, χ_A (where A is ^{6}Li, ^{10}B or ^{17}O), is given by

$$\chi_A = \kappa_B \frac{N_A/E}{N_B} \frac{f_B}{f_A} \frac{\sigma_B}{\sigma_A} , \qquad (4.4)$$

where κ_B is the areal density of ^{10}B atoms in the standard, N_B is the total number of counts detected in the standard run, f is the number of counts in the fission chamber monitor for each run, and σ is the cross section for each of the reactions. The quantity χ_A is determined in a direct manner from the number of counts in the spectrum. The only significant uncertainty which enters into the determination of χ_A is the uncertainty in the number of counts, N_A/E. Given χ_A, one then searches for a target composition which has a stopping power consistent with measured yield.

If the substance being profiled is a diatomic compound, then the ratio of the number densities of the two elements can be determined directly without having to

assume a composition and density for the sample. Consider a sample that is known to contain only tantalum and oxygen in significant amounts. The stopping power for the sample can be written in terms of the number density of oxygen in the sample, η_O, as

$$\frac{dE}{dx} = (\varepsilon_O + r\varepsilon_{Ta})\eta_O \ , \tag{4.5}$$

where r is the ratio of tantalum atoms to oxygen atoms in the sample. The density of ^{17}O atoms in the sample is related to the measured number of counts/cm^2/keV by the stopping power

$$\eta_{17} = \chi_{17}\frac{dE}{dx} = \chi_{17}(\varepsilon_O + r\varepsilon_{Ta})\eta_O \ . \tag{4.6}$$

Solving for the ratio, r, then gives

$$r = \frac{1}{\varepsilon_{Ta}\chi_{17}}\frac{\eta_{17}}{\eta_O} - \frac{\varepsilon_O}{\varepsilon_{Ta}}. \tag{4.7}$$

This is a useful approach, since the elemental ratio can now be determined without having to make any assumptions about the density of the target. In addition, only the ratios are needed to compute the effective stopping power which is used in extracting the width of the resonance. The only quantity that must be measured is the ratio of the fractional abundance of the isotope studied by CNDP, in this case the ratio η_{17}/η_O.

4.2.2 Implanted Al_2O_3 targets

Implantation is a particularly attractive method of target production because targets can be produced with an oxygen composition of nearly 100% ^{17}O using gas with relatively small enrichments. This is important, since oxygen gas with high enrichments of ^{17}O is difficult to obtain. At the time we began this experiment, the highest enrichment available on the commercial market was 50%. The effective stopping power for aluminum-oxide given in Table 4.1 is lower because of the 100% enrichment. We considered aluminum as a substrate for implantation, since it has been shown that a uniform subsurface layer of amorphous Al_2O_3 can be formed by implantation of high

doses of oxygen into aluminum [Che84, Mus85]. A target was produced by implantation of 2 x 10^{18} ions of ^{17}O at an energy of 80 keV into a 2 mm thick aluminum backing (99.99+%). The implantation was done by Implant Sciences Co. of Wakefield, MA at a cost of $700.

We collected data on the Al_2O_3 target for a one-day period at a proton energy of 80 keV and at a beam current of 130 μA. The beam current was low because at the time of the run we had not yet optimized the optics for maximum transmission. A total of 9 C of charge was collected on the target. At this point, we took the target to NIST and performed a CNDP. The result of the profile is shown in Figure 4.3. The composition of ^{17}O very close to the surface was somewhat ambiguous owing to the background from the $^{10}B(n,\alpha)^7Li$ reaction; however, there was a uniform number of counts between particle energies of 1300 to 1380 keV. A linear fit to this region gives 28 ± 2 counts/channel. Both closer to the surface and deeper in the target the number of counts falls off slowly. Applying this count rate to Eqn. 4.4, results in $\chi_{17} = 1.4 \pm 0.1$ (x10^{16} atoms/cm^2/keV). If we assume the target composition to be Al_2O_3, then we find a density of ^{17}O given by

$$\rho_{17} = 7.1 \pm 0.5 \left(\text{x}10^{22} \frac{\text{atoms}}{\text{cm}^3} \right) \tag{4.8}$$

at depths between 0.1-0.4 μm. This is in agreement with the density of oxygen expected from Al_2O_3 which is 6.8x10^{22} atoms/cm^3.

There was a surface boron contamination in the target of 5x10^{13} ^{10}B atoms/cm^2. While this is a small amount, it will produce roughly 100 counts/Coulomb into 4π. We exposed the target to an additional 14 C of beam and then analyzed the target again by CNDP. The second profile showed a much larger boron contamination of 10^{16} atoms/cm^2, and there was no ^{17}O observed. The upper limit on the ^{17}O concentration was set at $\kappa_{17} \leq 3\text{x}10^{16}$ atoms/cm^2.

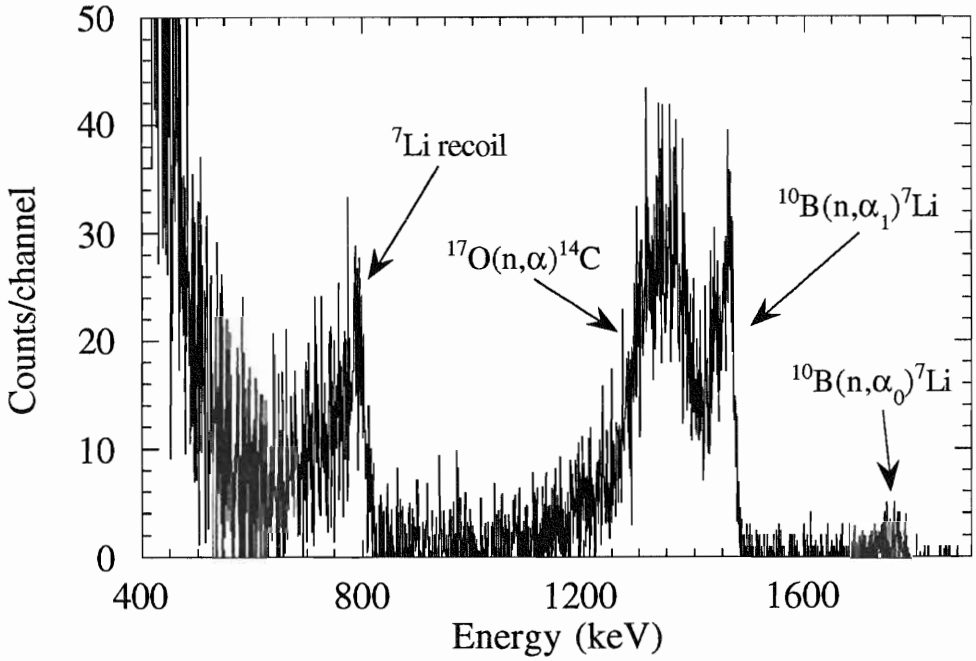

Figure 4.3: Cold neutron depth profile of Al_2O_3 target after 15 C of protons.

Although the back of the target was cooled with 10° C water throughout the run, the dramatic loss of oxygen and the large boron contamination suggests that the target may have experienced significant heating during the course of the run. Because of the expense of implantation, it was not possible to have a sufficient number of targets implanted so that they could be changed regularly in the event of oxygen loss or contamination. We therefore decided to use targets made by metal oxidation since these targets were easy to make and relatively inexpensive, a tenth the cost of implantation. It was fortuitous that at the time we made this decision, a supply of 77% enriched ^{17}O gas became available, and 0.5 liters were generously purchased by Oak Ridge National Laboratory for our use in this experiment.

No definitive source of the boron contamination was identified. While it is possible that the target was contaminated at some time other than during data collection, we seriously considered any possible source of impurity in the system and tried to eliminate it. The vacuum in the target chamber during data collection was maintained at

or below 10^{-6} Torr. The chamber is pumped by a turbo pump which is in turn backed by a mechanical pump. A molecular sieve was installed between the backing pump and the turbo pump to insure that no vapors could flow back through the turbo pump. We also isolated our system from the comparatively dirty vacuum in the tandem injection line by installing a gate valve after the inflection magnet. However, the CNDP showed that the boron contamination occurred deep in the target. The largest concentration of boron occurred at a depth of about 0.4 μm, which is consistent with implantation at the beam energy. This led us to the hypothesis that the boron is a significant parasite beam of the ECR ionizer. A charge-changing collision would allow a small fraction of the accelerated beam to pass through the inflection magnet and reach the target. In all future runs we ran with the ABPIS Wien filter at high field settings to insure selection of proton beams only. No significant boron contamination on the targets was encountered again.

4.2.3 Ta_2O_5 and WO_3 targets

Targets made of tungsten-oxide and tantalum-oxide were produced by resistive heating of 0.1-mm-thick metal sheets (99.9+% purity) in an oxygen atmosphere. The metal sheets were machined to 1.5" diameter disks. Before oxidation, the sheets were sanded with fine sandpaper on a lathe, then cleaned thoroughly with ethyl alcohol. A disk was then placed in a bell jar between two electrodes, and the chamber was evacuated to a pressure of less than 10^{-5} Torr. The disk was then resistively heated to a brilliant white to drive off any surface impurities. For tungsten, the applied current was about 370 A, while for tantalum it was about 200 A. The current was raised very slowly to these values over several minutes, then the current was held at the maximum value for about one minute, then reduced. Once the current was reduced to zero, the disk was allowed to cool for several minutes. The pumping to the jar was then closed off, and the chamber was back-filled with oxygen to a pressure of between 600 and 900

microns. It was found that the thickness of the oxide layer was substantially less if the oxidation was performed at a pressure of less than 500 microns. However, the thickness of the layer did not increase significantly for pressures greater than 500 microns. The disk was then heated slowly to a dull red color. The target began to glow red at currents of 240 A for tungsten and 120 A for tantalum. As the oxide layer formed, the target radiated less, and the current was gradually increased to keep the targets radiating a dull red color. At a current of about 300 A for tungsten and 180 A for tantalum, the red glow became constant. The current was held at this peak value for about one minute, then slowly reduced. The target was allowed to cool for several minutes, then the chamber was brought to atmospheric pressure with nitrogen gas. The target was transferred to a desiccator until ready to use.

Tungsten targets have the nice property that the targets change color when oxidized. The targets begin by turning a yellowish-green, then become bluer as the oxide layer gets thicker. Ultimately the targets become a deep purple. With a little experience we found it easy to gauge the quality of the target by visual inspection. The tantalum targets change from a shiny silver to a dull gray, but it was difficult to notice the change while the target was in the bell jar.

Boron is a common contaminant found in tantalum [Ber92]. To test the targets for boron contamination, a tantalum-oxide and tungsten-oxide target were produced by the manner described using oxygen of natural isotopic composition. We then analyzed these targets by CNDP. The count rates from these targets was so low that the background arising from neutron induced reactions on the collimators, natural radioactivity, cosmic rays and other sources was a significant fraction of the count rate. A background run of a comparable amount of time, about 24 hours, was taken without the targets in place. This background was normalized by the fission chamber monitor counts and subtracted from the profiles. The results are shown in Figure 4.4.

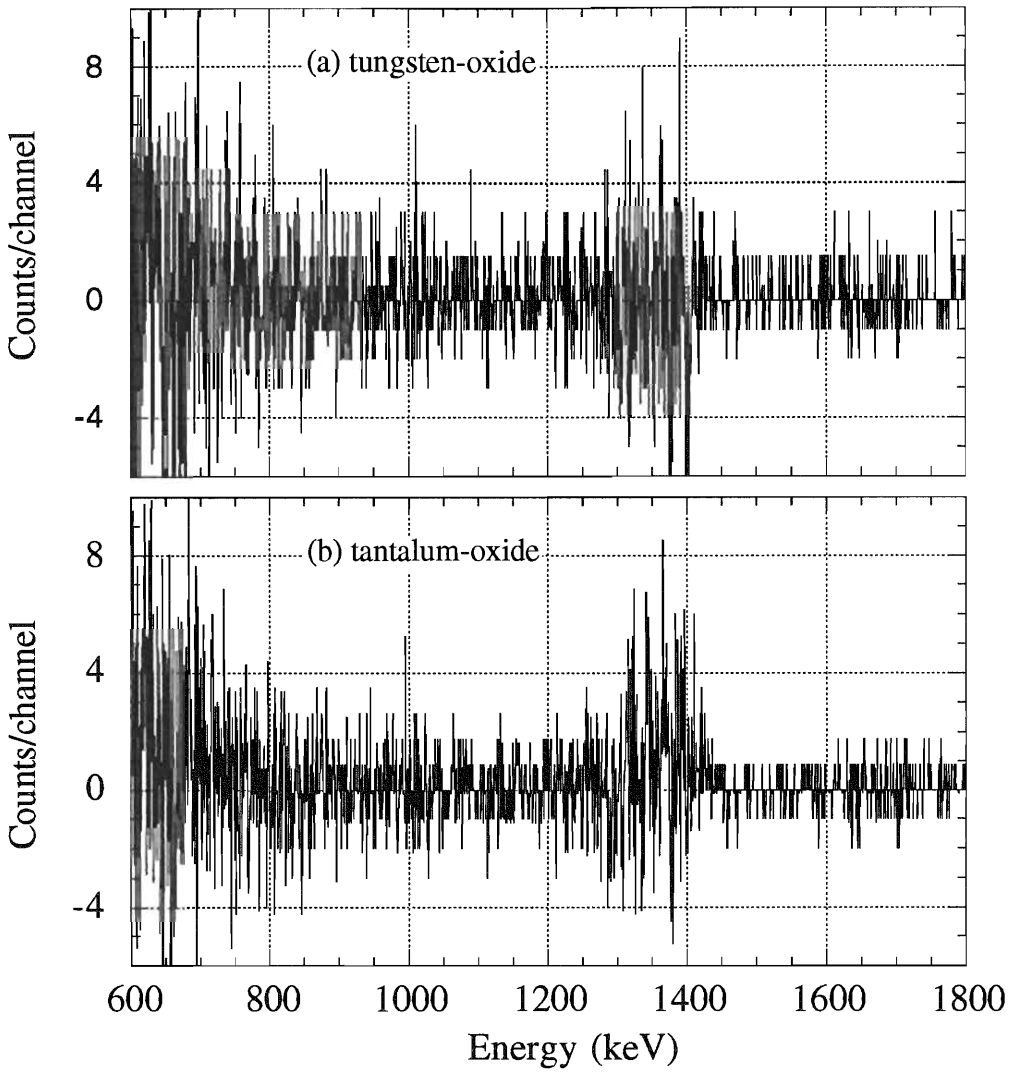

Figure 4.4: Cold neutron depth profile of (a) tungsten-oxide and (b) tantalum oxide targets (natural isotopic composition). A background run without the samples in place has been subtracted.

For the tantalum-oxide target there was an excess of 185 counts in the energy region between 1250-1460 keV. This is an excess of about 1 count/keV of energy. If we assume these counts to arise from the $^{10}B(n,\alpha)^{7}Li$ reaction, and assume a stopping power of the target for tantalum-oxide, this count rate corresponds to a density of ^{10}B atoms of $2x10^{17}$ atoms/cm^3. If we assume that the boron is of natural isotopic composition, then this corresponds to a total boron contamination of 2 parts per million (ppm) by weight. For the tungsten-oxide target there were no counts observed above

background, however, there was a factor of 1.7 times more data taken on the tantalum target. If we assume an upper limit on the number of boron alphas to be 0.5 counts per channel, then the upper limit on the boron contamination is $9x10^{16}$ atoms/cm^3. Thus, there is a detectable boron contamination in the tantalum-oxide target, but not in the tungsten-oxide target. It should be noted that the contamination is seen only in the first micron of the target, and is not seen deeper in the target. This would indicate that the contamination is a product of the oxidation process and is not a natural contaminant in the tantalum. Even if this contamination is inherent in the tantalum, it is at the ppm level and would not produce a significant background in the $^{17}O(p,\alpha)^{14}N$ experiment. Note also that there is no lithium contamination observed in either target. By the same analysis we can also set an upper limit on the lithium contamination in both targets of about $1x10^{17}$ atoms/cm^3.

We concluded from this analysis that there are not significant boron or lithium impurities inherent in either type of target. We tried using both tungsten-oxide and tantalum-oxide targets in the experiment, but we found that tungsten-oxide was not resilient to the high proton beam currents. After a dose of a few Coulombs, the oxide layer was totally depleted on the surface. This was visually evident since the area of the beam spot was no longer purple, but was again a silvery color. Because the oxide layer was found to be undepleted on the back side of the targets, we believed that the oxygen depletion was caused by local heating on the surface of the target. The depletion of oxygen in tungsten-oxide targets has been previously noted by Domingo [Dom63, Dom65]. Domingo found that attaching the targets to a water cooled copper plate dramatically reduced the oxygen depletion. We did not find this to be true, but we also had 7 times more incident power into a much smaller region of our target than did Domingo.

Since the depletion of the oxide was so dramatic, WO_3 targets actually provided a nice way to measure the size and location of the beam spot. This was important, since

the finite size of the beam spot contributes significantly to the resolution of the detection system and is needed to calculate the expected line-shape of the $^{17}O(p,\alpha)^{14}N$ peak. The beam spot consisted of a central oval-shaped region which was fully depleted in oxide, and a larger, very well-defined, circular region of radius 2 cm where the oxide was only partially depleted. The beam spot was centered on the target to within about 1mm. The sharp definition of the circular region indicates that the halo of the beam is being cut off by the circular collimators in the shroud, and that little beam is scattered onto other regions of the target.

The targets that were ultimately used in the experiment were made of tantalum-oxide. Tantalum-oxide has been proven to be very robust against intense proton bombardment [Ber92]. We analyzed two tantalum-oxide targets enriched to 77% ^{17}O by CNDP. One target was not exposed to any proton beam, while the other target had an accumulated charge of 15 C of protons at $E_p = 75$ keV from the $^{17}O(p,\alpha)^{14}N$ experiment. The CNDP of the target irradiated with protons is shown in Figure 4.5. The spectrum shows a flat distribution of alphas coming from the $^{17}O(n,\alpha)^{14}C$ reaction, but there are also a measurable number of counts arising from the $^{10}B(n,\alpha)^{7}Li$ reaction and the $^{6}Li(n,\alpha)^{3}H$ reaction. The counts from the boron reaction are localized near the surface of the target at 1472 keV, however the lithium contamination appears to be spread nearly uniformly throughout the target. We performed a linear fit to the counts from the lithium reaction. This fit is also shown in Figure 4.5.

The profile of the unirradiated target is shown in Figure 4.6. This target also shows the flat distribution of counts arising from the $^{17}O(n,\alpha)^{14}C$ reaction, but the counts from the $^{10}B(n,\alpha)^{7}Li$ and $^{6}Li(n,\alpha)^{3}H$ reactions are very different than what is seen in the CNDP of the irradiated target. There are a significant number of counts between energies of 1500 and 1800 keV, but there are no counts above background between 1800 and 2700 keV. Since we expect alphas and tritons from the ^{6}Li reaction

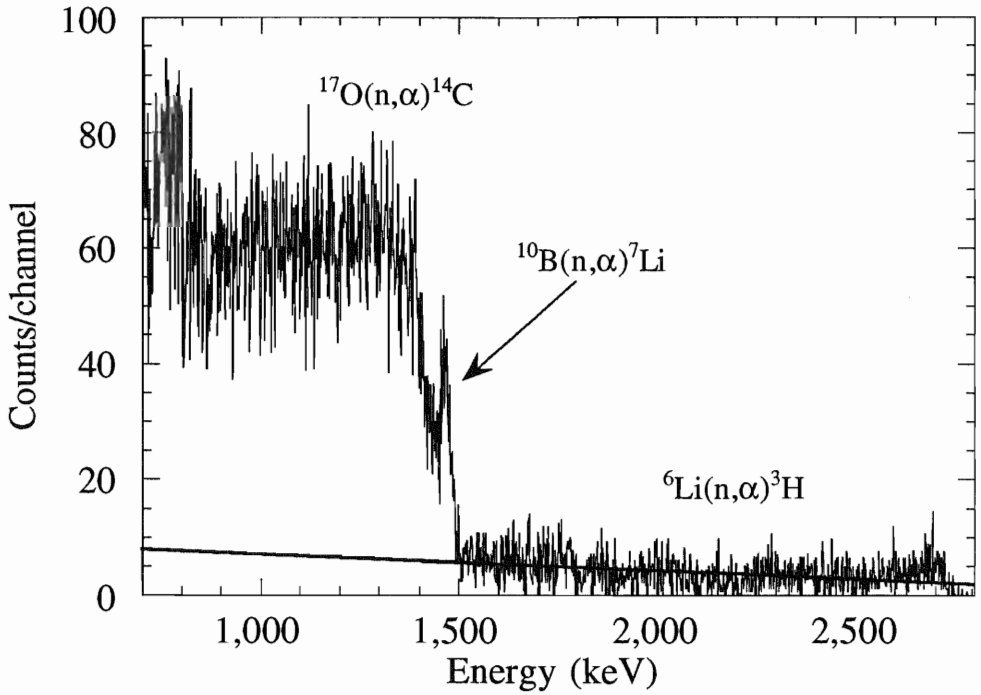

Figure 4.5: Cold neutron depth profile of $Ta_2[^{17}O]_5$. The target has been irradiated with 15 C of protons at E_p = 75 keV. The straight line indicates the fit to the lithium contribution.

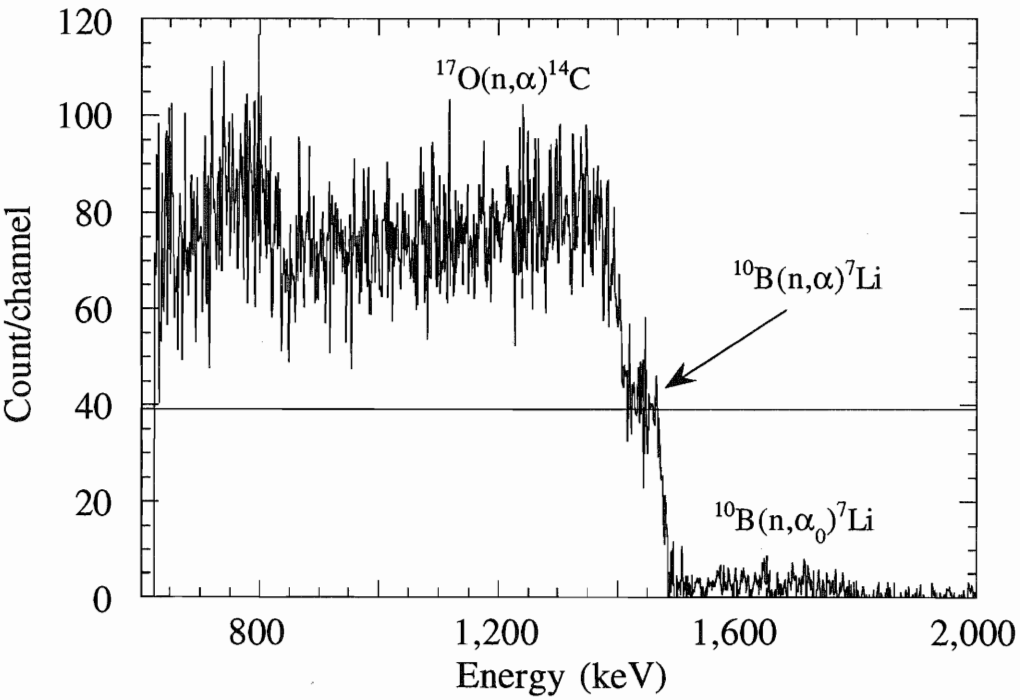

Figure 4.6: Cold neutron depth profile $Ta_2[^{17}O]_5$ target. The target has not been exposed to any proton flux. The straight indicates the bestguess for the contribution from the boron reaction.

to have energies up to 2700 keV, we conclude that all of the counts between energies of 1500 and 1800 keV are alphas from the 6% ground state branch of the ^{10}B reaction, which has a maximum energy of 1776 keV. We also conclude that there are no significant counts (< 1 count/channel) arising from the ^{6}Li reaction.

The large number of counts seen from the ground-state branch of the ^{10}B reaction indicates that there is substantially more ^{10}B in the unirradiated target. Although the statistics are poor, the counts seem to be distributed rather uniformly, indicating that the boron may be uniformly distributed in the target. The number of counts from the ^{10}B reaction is somewhat uncertain because of our limited information. We assumed that the number of counts from the ^{10}B reaction was constant with energy, and then estimated its value based upon the number of counts in the decays to the ground state branch and on the number of counts between energies of 1413-1472 keV. We estimate the number of counts from the boron reaction to be 38 ± 9 counts/channel.

The counts from the $^{17}O(n,\alpha)^{14}C$ reaction were determined by subtracting the indicated contributions from the ^{6}Li and ^{10}B reactions from each target. The density of ^{17}O atoms, as well as ^{6}Li and ^{10}B, was calculated by assuming the stopping power of the target to be that for Ta_2O_5. The density of ^{17}O atoms as a function of depth in the targets is shown in Figure 4.7 for the irradiated target and Figure 4.8 for the unirradiated target. A target which is Ta_2O_5 with 77% of the atoms being ^{17}O, should have a ^{17}O density of 4.2×10^{22} atoms/cm^3. The ^{17}O composition of the irradiated target agrees with this prediction. Although the ^{17}O density for the unirradiated target is somewhat lower than expected, there is a large systematic uncertainty in the density, which arises from the uncertainty in the boron subtraction.

The densities of the ^{17}O, ^{10}B and ^{6}Li isotopes determined by cold neutron depth profiling for the two targets are summarized in Table 4.3. Except for the surface boron contamination in the irradiated target, the densities of all these isotopes are roughly constant as a function of depth in both targets. Although the number of counts from the

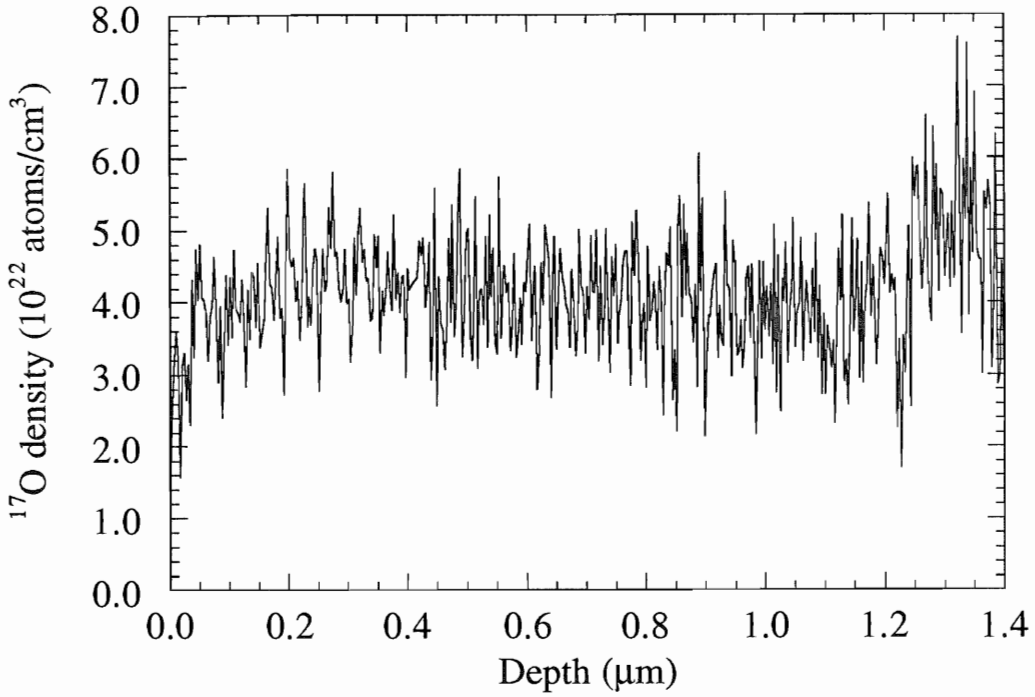

Figure 4.7: Density of ^{17}O in the irradiated target assuming a stopping power for the target for Ta_2O_5.

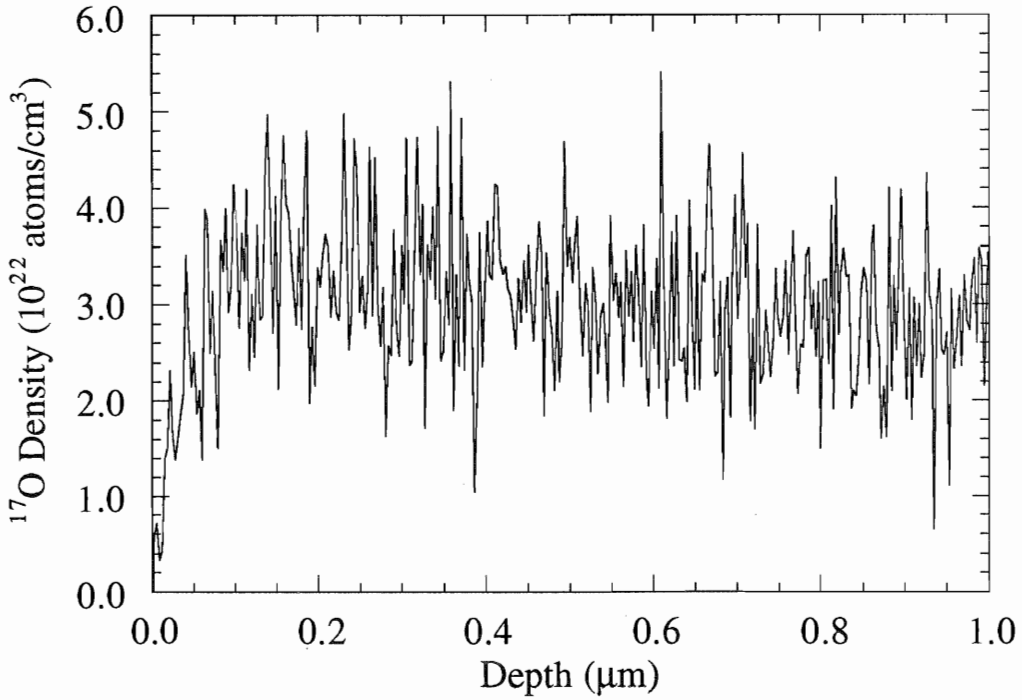

Figure 4.8: Density of ^{17}O in the unirradiated target assuming a stopping power for the target for Ta_2O_5.

Table 4.3: Densities of isotopes in $Ta_2[^{17}O]_5$ targets determined from CNDP. (*Surface concentration)

Isotope	Density (atoms/cm^3)	
	Irradiated Target	Unirradiated Target
^{17}O	$4.1 \pm 0.3 \times 10^{22}$	$3.2 \pm 1.2 \times 10^{22}$
^{6}Li	$1.2 \pm 0.2 \times 10^{18}$	$\leq 2 \times 10^{17}$
^{10}B	$(1.0 \pm 0.2 \times 10^{18})^*$	$2.0 \pm 0.5 \times 10^{18}$

$^{6}Li(n,\alpha)^{3}H$ reaction in the irradiated target and the $^{10}B(n,\alpha)^{7}Li$ reaction in the unirradiated target were significant compared to the number of counts from the $^{17}O(n,\alpha)^{14}C$ reaction, the cross section for the ^{6}Li reaction is 4,000 times that of the ^{17}O reaction, and the cross section of the ^{10}B reaction is 16,000 times that of the ^{17}O reaction. The densities of these contaminants in the targets is actually quite low.

The fact that the contaminants appear to be uniformly distributed in the first microns of the target indicated that they were probably introduced into the targets during oxidation. Both targets were made from the same piece of tantalum, thus it is not likely that the contamination was present in the tantalum initially. One target was made immediately after the other target, and the targets were made following the same prescription, with as little deviation as possible. However, these levels of contamination are at the part per million level, and it would be difficult to fully eliminate contaminates at this level without dramatic precautions. Such steps are not necessary. By being particularly cautious, i.e. cleaning the bell jar thoroughly, pumping it down for an extended time, etc., we could easily keep the level of contamination in the targets below 10^{18} atoms/cm^3. At this level, the background in the $^{17}O(p,\alpha)^{14}N$ experiment from other sources, such as cosmic rays, was more significant than the background from the contaminant reactions.

If we assume that the isotopic abundance of ^{17}O in the targets is 77% as quoted, then the ratio of tantalum to oxygen atoms can be calculated by Eqn. 4.7. After subtracting the lithium contribution from the profile of the irradiated target, we arrived at a ratio of tantalum to oxygen atoms of 0.42 ± 0.04. This results lends further evidence, though not independent of the previous analysis, that the structure of our targets is Ta_2O_5 with 77% of the oxygen atoms being ^{17}O. We will take the effective stopping power of the targets to be that of Ta_2O_5, as given in Table 4.1.

4.3 Rutherford back-scattering

Cold neutron depth profiling provided an accurate method for determining the concentrations of the isotopes in which we were most interested; however, it was not a convenient method of target analysis. The targets had to be taken to the NIST Cold Neutron Research Facility in Gaithersburg, MD. Because of the small neutron-capture cross section for ^{17}O, between one and two days of beam time were required to profile a pair of targets. The tantalum and tungsten targets become activated by this procedure and could not be used in the $^{17}O(p,\alpha)^{14}N$ experiment after being profiled. For this reason, targets were also analyzed by measuring elastic scattering of alpha particles at back angles, i.e. Rutherford Back Scattering (RBS).

Because of the large background from the elastic scattering off of the heavier inert atoms, this technique was not very sensitive to the isotopic composition of the light elements in the targets. The elastic scattering was most useful as a relative measure of the density of the inert atoms. All of the compound targets we studied consisted of a layer of oxide on the surface of a thick, pure substrate. Since the density of the inert atoms in the oxide is less than in the pure substrate, this is seen as a decrease in the elastic scattering yields.

Elastic scattering was particularly advantageous because it was easy and nonintrusive. We performed RBS using the alpha negative-ion source and FN tandem

accelerator at TUNL. Elastic scattering yields were measured at 165° and E_α = 6 MeV. Targets were periodically removed taken from the low-energy experiment and profiled using RBS in the high-energy target chamber. This allowed us to monitor the oxide layer for changes in composition with accumulated beam.

Two RBS profiles of the tantalum-oxide target which was irradiated with protons and profiled by CNDP (see Figure 4.5 and 4.7) are shown in Figure 4.9. The first profile was taken before the target was exposed to any proton beam, while the second profile was taken after 15 C of integrated beam. There is no noticeable difference between the two profiles. Both profiles show a decrease in the count rate from the tantalum atoms at energies greater than 4.0 MeV. This indicates an oxide layer with a thickness of about 3 μm. The peak from the alphas scattered from oxygen is evident at about 2.5 MeV.

A FORTRAN code was written to calculate the elastic scattering yields from compound targets. The program is interfaced with the RKIN relativistic kinematics routine and calculates stopping powers based upon the coefficients of Anderson and Ziegler [And77b]. The code will calculate profiles for any chemical compound, but assumes the Bragg sum rule to hold. Also, only uniform compositions can be entered in layers.

We found that the ratio of the yields from elemental targets to the yields from compound targets do not agree with the known composition of the targets. A calculated profile is shown with the measured profile for the enriched tantalum-oxide target profiled by CNDP in Figure 4.10. The profile was calculated assuming a 3 μm layer of Ta_2O_5 on the surface of pure Ta. Note the sharp step at the interface. The height of this step is proportional to the ratio of O atoms to Ta atoms in the surface layer. The computed step height for Ta_2O_5 is significantly greater than the measured height. The CNDP of this target shows that the composition is Ta_2O_5 to within 10% error. This same effect was seen in all the compound targets we profiled. The step heights were

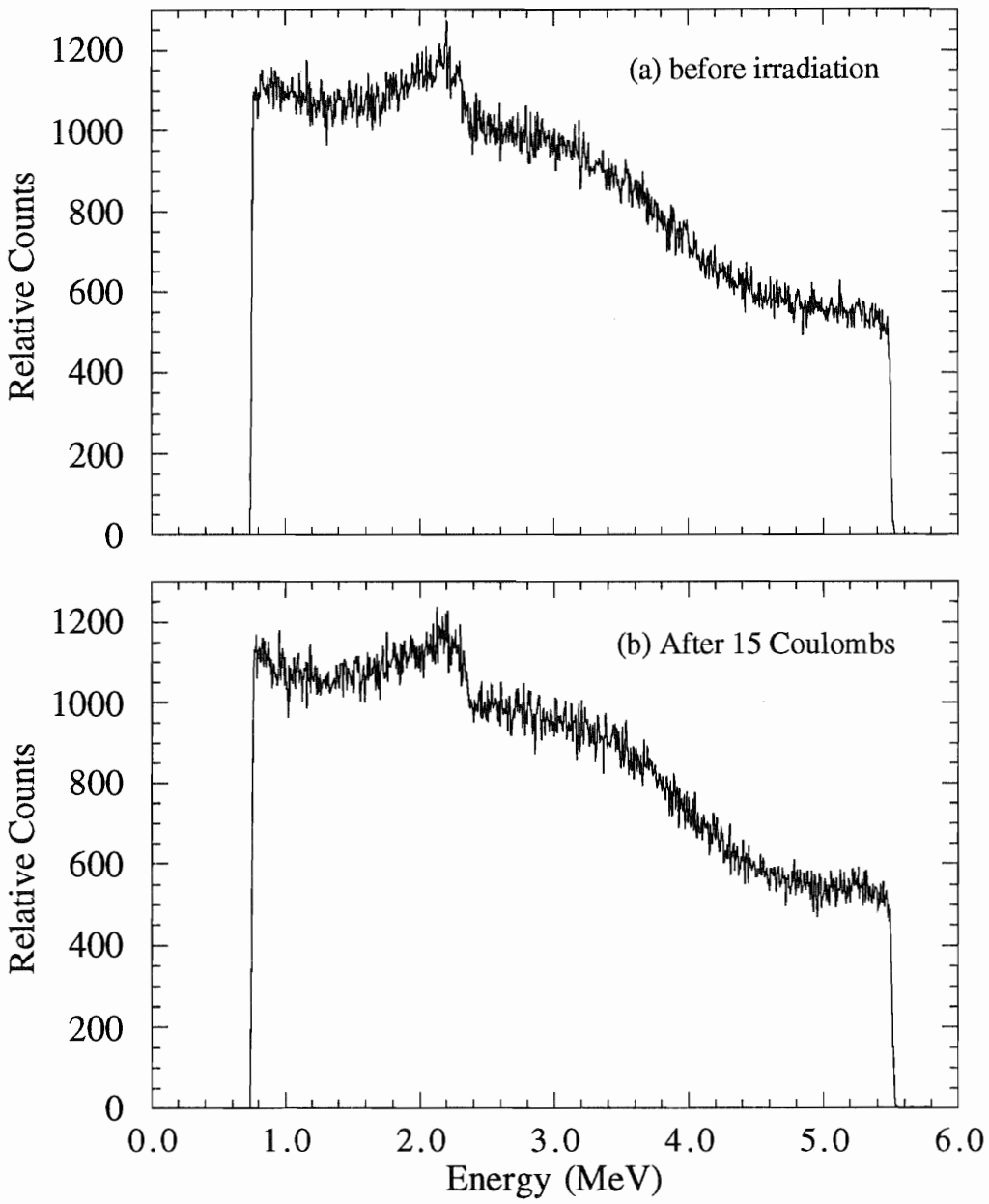

Figure 4.9: Elastic scattering of 6 MeV α's on a Ta_2O_5 target (same target profiled by CNDP in Figure 4.5) before and after proton bombardment (I_{beam} = 150 μA).

consistently smaller than predicted by theory. There are only a limited number of things that could cause this.

One possibility is that the cross section is non-Rutherford. Because the oxide layer was so thick, we had to run at an alpha energy of 6 MeV in order to fully see the step. The cross section for light elements is certainly non-Rutherford at this energy. Note the much larger height of the oxygen peak in the measured spectra than in the calculated spectra. Another possibility is that the tabulated stopping powers for oxygen are incorrect. All of the targets we profiled were oxide compounds, so this could be a problem specific to oxygen. Also shown in Figure 4.10 is a calculated profile where the stopping power for oxygen has been lowered by 20%. Another possibility, related to this one, is that the Bragg sum rule is wrong. This would also lead to incorrect stopping powers for the compounds.

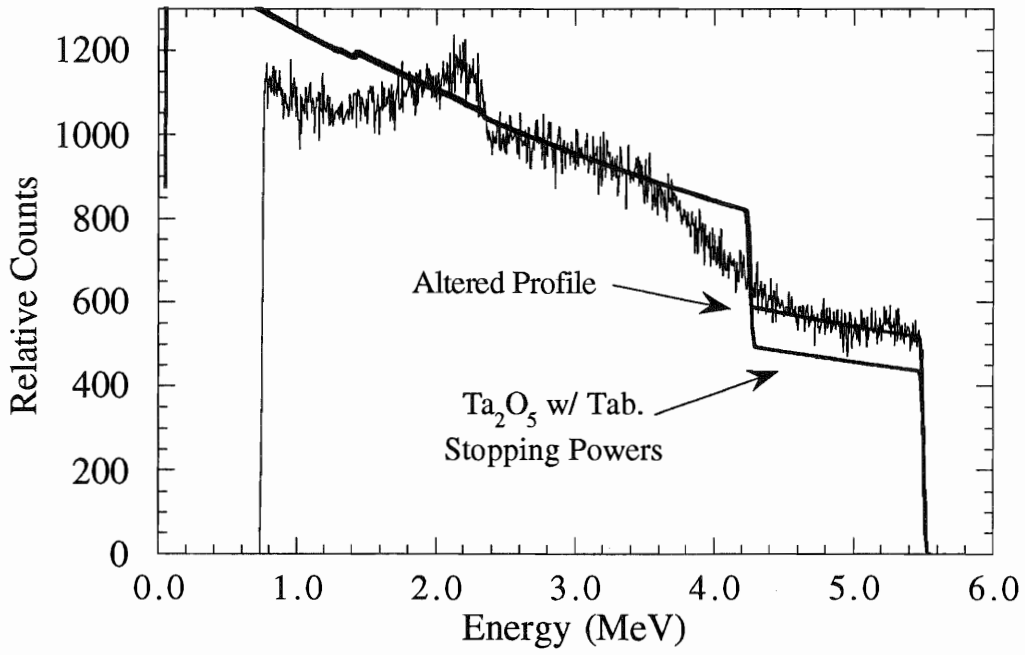

Figure 4.10: Comparison of calculated elastic scattering of 6 MeV α's on Ta_2O_5 target with profile of Fig. 4.9b. Both calculated curves have been normalized to the measured spectrum at 3 MeV.

Ultimately, we used the RBS profile of the Ta_2O_5 target that was also profiled by CNDP as standard for comparison, since there was a reasonable degree of confidence that this target was Ta_2O_5. All targets were profiled by RBS before use, and after regular intervals during the experiment. These profiles where then compared with the RBS profile of our "standard" target. All targets showed a step height which was consistent with that measured for the target profiled by CNDP. We take this as evidence that the composition of all the targets was Ta_2O_5, and we adopt an effective stopping power for the targets of

$$\varepsilon_{\text{eff}} = \varepsilon_O + \frac{23}{77}\varepsilon_O + \frac{2}{5}\frac{1}{0.77}\varepsilon_{Ta} = 39 \ \frac{\text{eV}}{10^{15} \text{ atoms/cm}^2} \ . \qquad (4.9)$$

The elemental stopping powers used in Eqn. 4.9 were taken from [And77a].

The CNDP of the tantalum-oxide target confirmed its composition to within an uncertainty of about 7%. In addition to the error in composition of the target, there is also the error in the elemental stopping powers. The errors in these elemental stopping power ranges between 5 and 20% depending on the element. There is a reasonable data set used in computing the stopping powers for both these elements, so the error should be on the smaller end of the error range. We adopt a total uncertainty in the effective stopping power of ± 10% to include the uncertainty due to the elemental stopping powers.

V. The Detection System

5.1 Design

Because the count rate from the $^{17}O(p,\alpha)^{14}N$ reaction is so low, it was important to devise the most efficient detection system possible. Equally important was the energy resolution. There were limitations to both. Since the targets were thick, particles were not emitted from the target in the forward direction. Hence, the maximum efficiency was somewhat less than 50%. The resolution of the detection system was limited by kinematics. Alphas which are emitted from the reaction at 150° have 40 keV less energy then alphas which are emitted at 100°. A larger detector might have a higher detection efficiency; but it also detects particles with a larger range of energies. The challenge was to construct a detection system that covered as much of 2π solid angle as possible, but to do so with the best resolution and the lowest background counting rate possible.

One complication was the intense flux of elastically scattered particles. The count rate from elastic protons is a factor of 10^{15} greater than that from the $^{17}O(p,\alpha)^{14}N$ reaction. We needed to count as many alphas as possible, at the same time rejecting a very high percentage of the protons. This was accomplished by using implanted silicon detectors with a nickel foil mounted in front of the detectors to stop the protons. The thickness and uniformity of the foil were crucial. The protons have a maximum energy of 75 keV, and we needed to detect alphas with energies as low as 700 keV, from the $^{10}B(p,\alpha)^{7}Be$ reaction. The mean energy loss of a 75 keV proton and a 700 keV alpha particle as a function of foil thickness is shown in Figure 5.1. The mean range of a 75 keV proton in nickel is 0.54 μm, but it was necessary that the foil be somewhat thicker than this to stop a high percentage of the protons. Since the background from cosmic

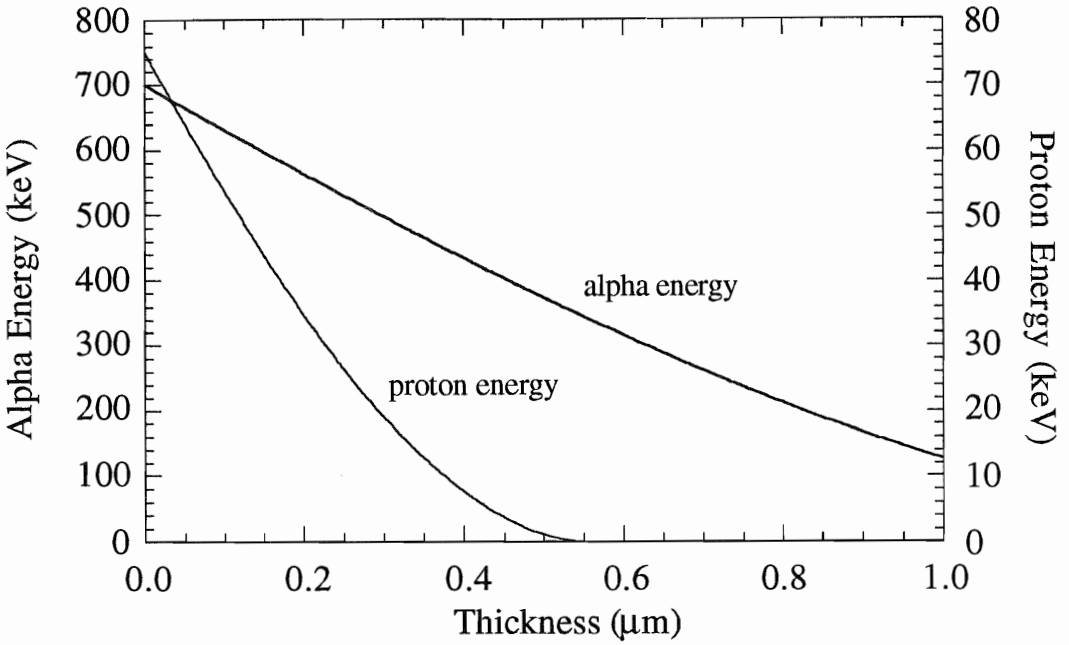

Figure 5.1: Energy loss of a 700 keV α-particle and a 75 keV proton in nickel.

rays and detector noise rises exponentially at low energies, the foil had to be no thicker than necessary, to minimize the degradation of the alpha-particle energy. Nickel foils of the highest grade were purchased from Chromium Corporation in Cleveland, Ohio, for mounting in front of the detectors. Foils of thickness 0.64 μm were used since Chromium could not guarantee thinner foils of this grade.

Not only does the foil decrease the energy of the alpha particle, but it also degrades the resolution of the detection system significantly. This is due in part to the energy straggling of the particle in passing through the foil, but more important for large area detectors are the different thickness of foil which particles traverse at different angles. In order to help determine the best practical detector configuration, a FORTRAN code was written to calculate response functions of the detection system. Some important effects that are considered in the calculation include the energy loss of

the beam in the target, the energy loss of the alpha particle in the detector and foil, the finite size of the beam, the intrinsic detector resolution, and the angular distribution of the scattering cross section. One effect which is not explicitly taken into account in the calculation is the energy straggling of the alpha particles in passing through the foil. We calculated the straggling of the particles separately using the STRAGL code from the TUNL software library. The straggling at these energies is Gaussian with a FWHM of the straggling distribution between 5% and 10% of the mean energy loss. This is significantly smaller than the variation in the energy loss for particles traversing the foil at different angles. In first approximation we included the energy straggling by increasing the intrinsic resolution of the detector.

The program assumes a rectangular detector, but any size and orientation may be specified. Any combination of foil layers of any composition may also be specified. The code is interfaced with the RKIN relativistic kinematics routine from the TUNL software library and computes stopping powers based upon the coefficients of Anderson and Zeigler [And77a, And77b]. The input parameters are passed to the code in an input file, so the detector configuration may be easily changed. Detector response functions were calculated for various detector sizes in different geometries. The best detector configuration is one which subtends the greatest solid angle in the smallest kinematic range. We limited our consideration to detectors with a 0.64 μm Ni foil in front of the detectors.

The most important factors in determining the response function were the range of angles subtended by the detector and the orientation of the foil with respect to the detector and target. If the detector subtends a large range of angles, then the particles it detects travel through a large range of distances in the foil. The range of angles subtended by the detector in the azimuthal direction was nearly as important as the range in the polar angle. Smaller detectors have proportionally better resolution, but at the

expense of efficiency. The ideal situation was to have many small detectors. It was also very important that the detector and foil be "square" to the target. This means that a line connecting the center of the target to the center of the detector should be nearly perpendicular to the plane of the detector and foil. This minimizes both the range of angles that the detector accepts and the mean distance through the foil.

The detector response function also depends upon the angular distribution, $W(\theta)$. We have taken the angular distribution of the alpha-particles to be isotropic. The spin and parity of the 5673 keV state in ^{18}F are known to be 1^-, and the spin and parity of the ground state of ^{17}O are known to be $\frac{5}{2}^+$. Thus, the incident channel spin must be 2^+ or 3^+, and the only possible orbital angular momentum in the incident channel is $l = 1$ or $l = 3$. The penetrability for a proton in a $l = 3$ state is much less than the penetrability for a proton in a $l = 1$ state at these energies, and the contribution to the yield occuring through $l = 3$ in the incident channel can be neglected. If we assuming that the reaction proceeds through $l = 1$ in the incident channel with a channel spin of 2^+, then we find by appropriate coupling of angular momenta that the angular distribution for the alpha particles is isotropic in the center-of-mass frame. Transfering to the lab frame from the center-of-mass introduces a change of only few percent, so we take the angular distribution to the spherically symmetric in the lab frame as well.

One thing which can often be done to improve resolution, particularly when the resolution is limited by kinematics, is to use position-sensitive detectors. Particles which are detected at further back angles will have less energy, and a correction to the energy as a function of angle can be made. That there would be any significant improvement in resolution by using position-sensitive detectors in this situation is questionable. It should first be noted that the detectors would have to be position-sensitive in two directions, since the spread in energies in the azimuthal direction is almost as large as the spread in energies in polar angle. This is possible; however, a bigger problem arises because the beam spot is of comparable size to the distance

between the target and detector. Thus, any point on the surface of the detector will see a range of angles coming from different positions on the target. This problem is compounded by the angle straggling of the particles in passing through the foil.

We found the optimum practical system to use six 2 cm x 2 cm detectors. With larger detectors it is possible to cover significantly more solid angle, but the net increase in the number of counts per energy bin of the detected particle does not significantly increase. It is theoretically possible to make significant gains by using smaller detectors, but increasing the number of detectors. The best detection system would be a group of 20 to 30 rear-mounting detectors of area about 1 cm^2 arranged in a soccer ball geometry. The two problems with such a design are its complexity and cost. Using six 4 cm^2 detectors, we achieved a detection system with comparable efficiency and resolution at only a moderate expense.

Figure 5.2 shows three of the detector configurations which we considered. The first two configurations are for a 2 cm x 2 cm square detector, while the third configuration is for a 5 cm x 5 cm square detector. Configuration #1 was the detector placement used in the experiment. The plane of the detector makes an angle of 67.5 degrees with the plane of the target. In Configuration #2, the side of the detector at large theta is in the same location as in Configuration #1, but the detector has been rotated so that it is perpendicular to the plane of the target.

A comparison of the peak shapes for these three different detector configurations is shown in Figure 5.3. The calculated alpha particle energy distributions from $^{17}O(p,\alpha)^{14}N$ and $^{10}B(p,\alpha)^{14}N$ are plotted. Configuration #2 has a greater total solid angle than Configuration #1, but because of the greater range in values of the energy loss in the foil, the height of the signal is actually less. With the 25 cm^2 detector (Configuration #3), this effect is even more dramatic. The total solid angle for this detector is almost 3 times as large as the total solid angle for the 4 cm^2 detector in Configuration #1, but the height of the signal is about the same. The counts which are

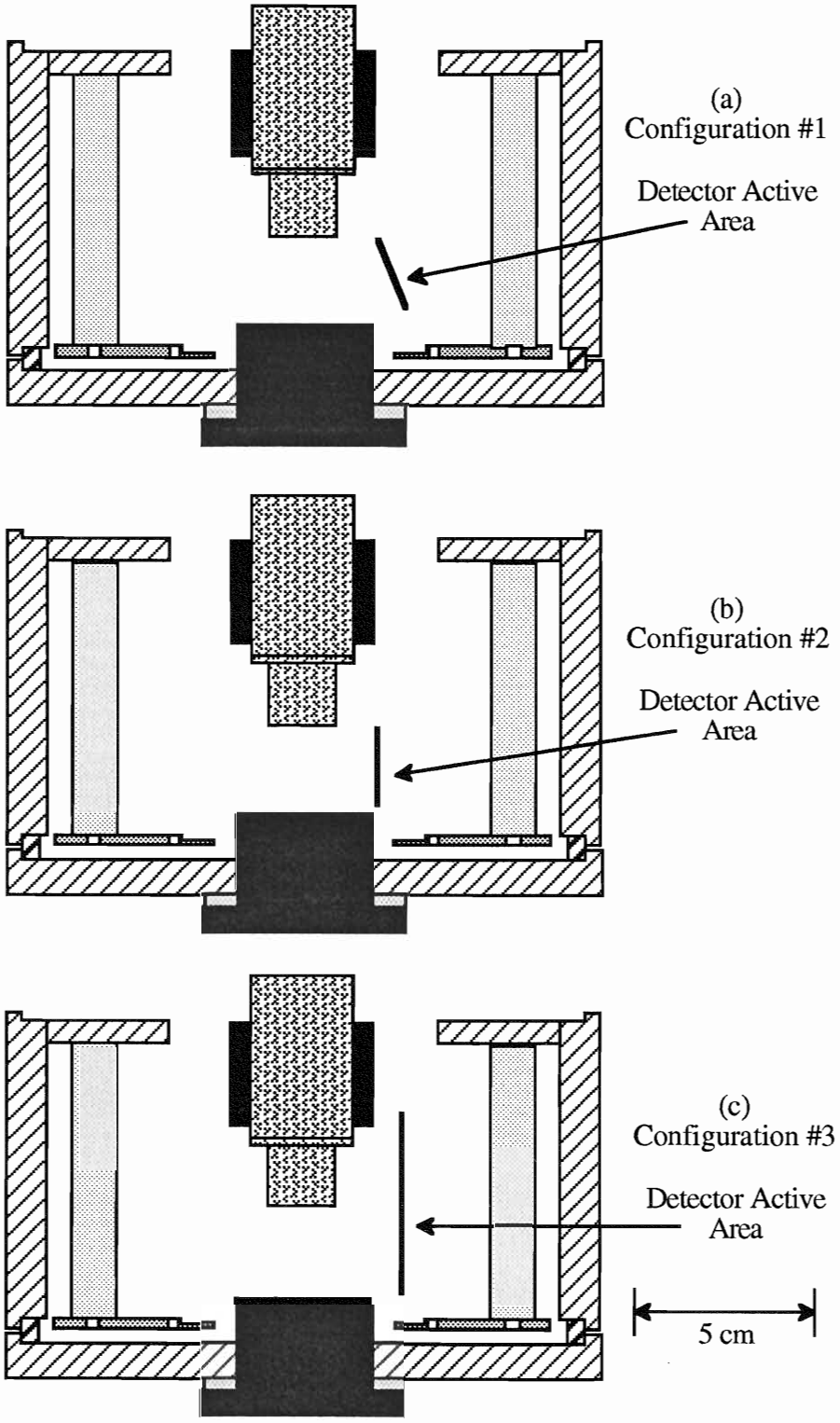

Figure 5.2: Detector configurations used in calculating the line shapes shown in Figure 5.3.

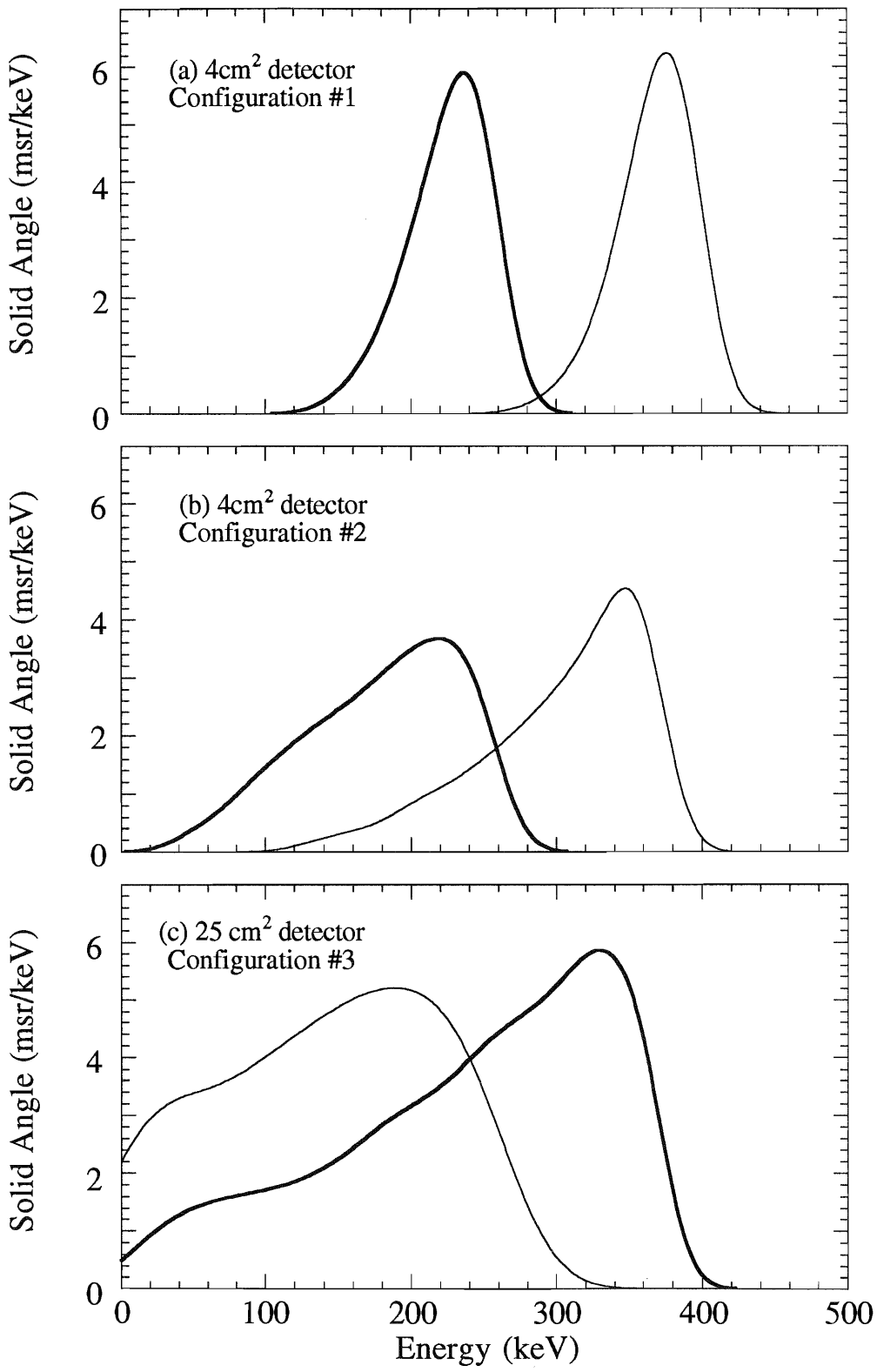

Figure 5.3: Calculated line shapes for the $^{10}B(p,\alpha)^{7}Be$ and $^{17}O(p,\alpha)^{14}N$ reactions for the three different detector configurations as illustrated in Figure 5.2. The higher energy peak is the ^{17}O reaction.

Table 5.1: Comparison of calculated peak shapes for 3 detector configurations. The configurations are illustrated in Figure 5.2.

Config #	Detector Size (cm^2)	$\angle$ w/ Target (degrees)	Efficiency (% of 4π)	Height (keV/msr)	FWHM (keV)
1	4	67.5	3.3	6.2	60
2	4	90	4.1	4.5	95
3	25	90	9.5	5.9	187

collected in the larger detector which are not collected with the 4 cm^2 detector in Configuration #1 all have energies which are far from the mean value. A summary of the important properties of the signal shapes for these three configuration is given in Table 5.1.

The detection system we used in the $^{17}O(p,\alpha)^{14}N$ experiment consisted of six 2 cm x 2 cm square detectors placed around the target in the location given by Configuration #1. The detectors were custom-built without an aluminum contact layer, so that the energy lost by the alpha particle before entering the active region of the detector would be minimized. The detectors were placed at evenly spaced intervals of 60° in the phi direction. Each detector subtends 3.3% of 4π in solid angle, giving a total efficiency for the system of 20% of 2π. This is almost half of the theoretical maximum efficiency.

The plate on which the detectors were mounted was made of brass. A six-sided pyramid, also made out of brass, was constructed and soldered onto the detector plate. This pyramid is completely enclosed except for a circular opening at the apex, through which the shroud protrudes, and the holes which were cut in front of the detector positions. The nickel foils were mounted on 0.8-mm-thick aluminum frames which were attached by screws to each face of the pyramid, so that the foil covers the opening in front of the detectors. The detectors were held in a slot machined into rectangular pieces of delrin, which were in turn mounted to the back plate by screws. A schematic

of the target chamber showing the locations of two of the 6 detectors and the detector plate with the pyramid is given in Figure 5.4.

5.2 Efficiency calibration

The efficiency of the detection system was measured with a calibrated ^{241}Am source, but first the quoted calibration of the source was checked. The source was mounted in a large chamber opposite a 1.50 cm^2 silicon surface barrier detector which was collimated to 0.60 ± 0.01 cm^2. The distance to the source was measured to be 26.73 ± 0.01 cm, so the efficiency of the detector was $6.7 \pm 0.1 \times 10^{-5}$. A total of 115000 ± 1000 counts were collected in 30650 seconds. The counts from the source had a small, but long, tail to low energies. The uncertainty in the number of counts is a result of the uncertainty in how much of this tail was to be included. With these results the activity of the source was found to be 3.36 ± 0.07 Mdpm (million decays per minute). This efficiency was measured on August 26, 1994. The quoted efficiency of the source is 3.4 Mdpm, measured on March 7, 1985. Taking into account the 432.7 year half-life of ^{241}Am, the activity should be reduced to 3.35 Mdpm at the time the new calibration was made, in excellent agreement with the measured value.

The efficiency of the detectors as used in the $^{17}O(p,\alpha)^{14}N$ experiment was measured by mounting the calibrated ^{241}Am source onto the target holder and measuring the count rate. One difficulty in making this measurement was in insuring that the source be located at the same position as the targets in the $^{17}O(p,\alpha)^{14}N$ experiment. Because the source has a different thickness than the targets used in the experiment, the target holder had to be shimmed in order to put the source in the proper location. It is also possible that the source was not centered on the location of the beam spot. To account for these uncertainties, the efficiencies of each of the detectors was measured three times. Between each measurement the target holder was removed from the

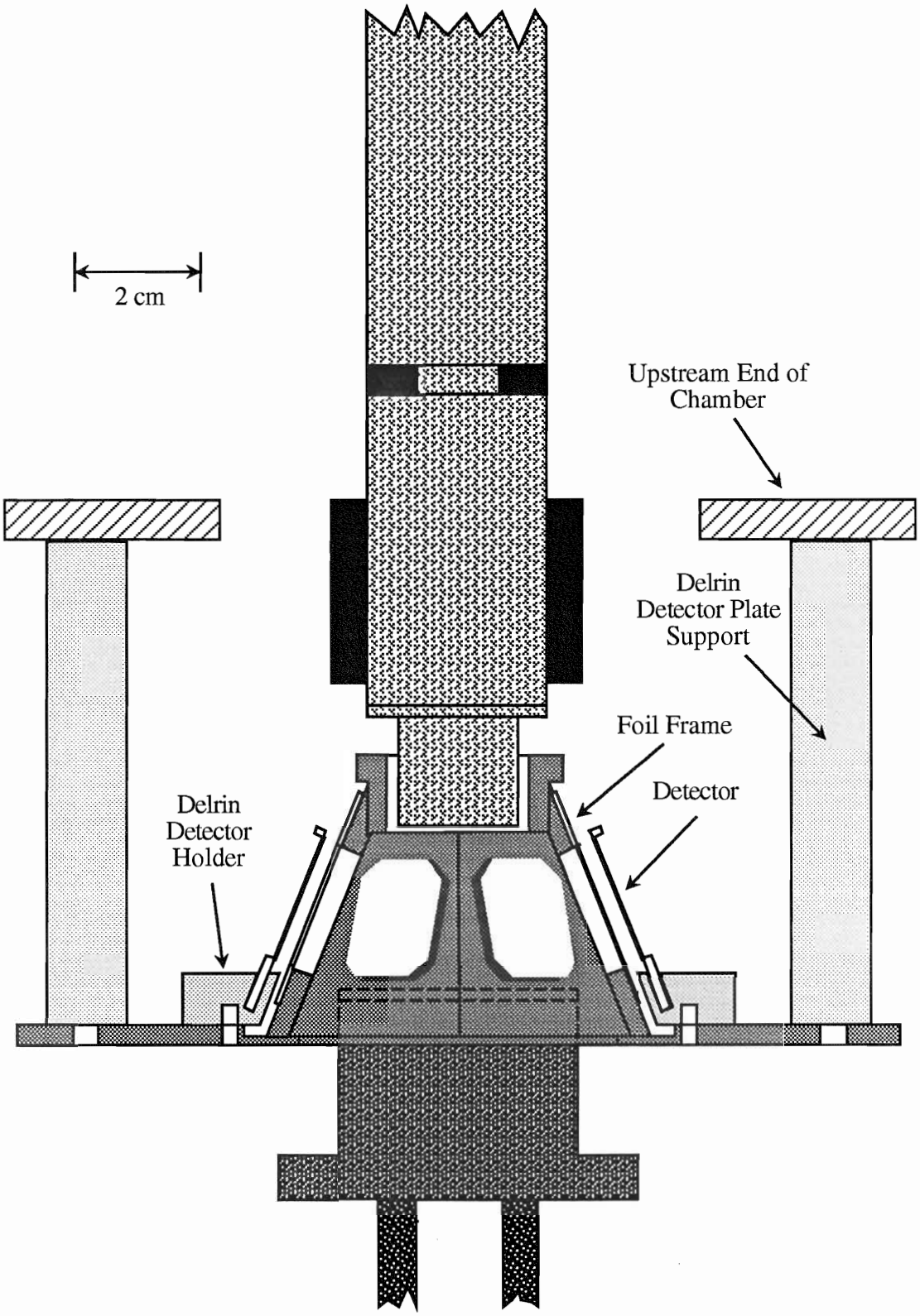

Figure 5.4: Schematic of target chamber showing the location of the pyramid and two of the six detectors. Note that the walls of the target chamber are not shown.

chamber, then returned in a different orientation and shimmed in a different manner. The measured count rate for each detector is summarized in Table 5.2.

The average efficiency per detector from these measurements was found to be 0.0249 ± 0.0007. However, there is an additional uncertainty in this measurement that arises in the determination of the count rate. The alphas from the ^{241}Am source have an energy of 5.5 MeV, while the alphas from the $^{17}O(p,\alpha)^{14}N$ reaction have an energy of between 0.7 and1.0 MeV. The energy distribution of alpha particles detected from the ^{241}Am source had a low energy tail extending all the way down to zero energy. In determining the efficiency, a decision had to be made as to how much of this tail was to be included. The results provided in Table 5.2 were determined by accepting alphas in energy down to about 4.5 MeV. This resulted in discarding 3% of the counts, but it is also possible that we have overcounted. We assume an additional systematic error in this determination of the efficiency of 3%, and take the total error from this measurement to be 0.0249 ± 0.0011.

The efficiency determined from the ^{241}Am measurement was in disagreement with calculations of the efficiency given the size of the detectors (2x2 cm) and their measured location (see Table 5.1). The calculated efficiency from geometry was 0.0329 $\pm$ 0.0005. This difference was found to arise because the active area of the detectors

Table 5.2: Measured count rates (1,000's per minute) for each detector using the calibrated ^{241}Am source.

	Trial #1	Trial #2	Trial #3	Average	σ
Det #2	84.5	84.1	85.0	84.5	0.5
Det #7	82.9	83.6	83.5	83.3	0.4
Det #8	84.8	86.6	82.9	84.8	1.9
Det #9	80.7	79.3	80.9	80.3	0.9
Det #10	85.3	87.7	85.4	86.1	1.4
Average	83.6	84.3	83.5	83.8	2.3

was significantly smaller than 4 cm^2. The active area of the detectors was measured by placing an uncollimated detector in a large chamber far from the calibrated ^{241}Am source. The active area, A, was calculated from the measured distance, d, from the source to the detector and the count rate by

$$A = 4\pi d^2 \frac{\text{Counts/time}}{3.36\text{x}10^6 / \text{min}} \tag{5.1}$$

Two detectors were measured in such a manner, and the results are summarized in Table 5.3. The average active area per detector was found to be 3.12 ± 0.05 cm^2. This is consistent with a 2.3-mm wide strip around the edge of the detector being inactive. The peak shape was recalculated using the PALPHA code for a detector with an active area of 3.12 cm^2. The total efficiency was found to be 0.0258 ± 0.0010. We varied the location of the active area among the 4 cm^2 of the detector and found no significant change in the total efficiency. The final efficiency per detector was determined by taking the average of the calculated value and the measured value and was found to be

$$\Omega = 0.0254 \pm 0.0006 \ . \tag{5.2}$$

There was some deviation in the calculated shape of the peak as a function of the

Table 5.3: Measured active area of two detectors.

Detector #	Distance (cm)	Counts	Time (sec)	Active Area (cm^2)
2	50.8 ± 0.3	3890 ± 60	730	3.09 ± 0.07
10	44.2 ± 0.2	6460 ± 80	900	3.14 ± 0.05

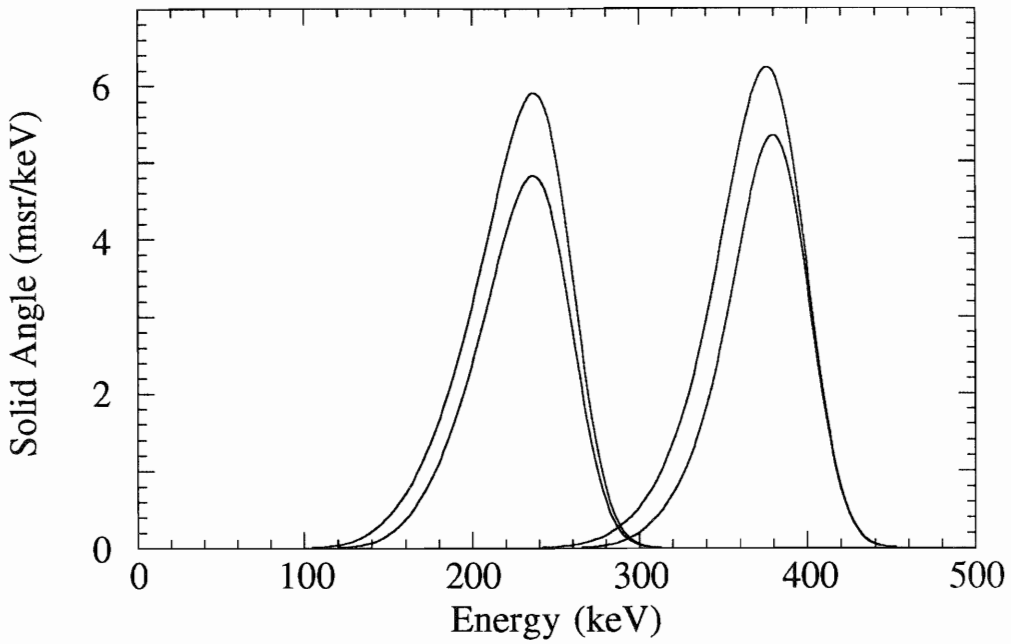

Figure 5.5: Calculated line shapes for the $^{10}B(p,\alpha)^{7}Be$ and $^{17}O(p,\alpha)^{14}N$ reactions for detectors of active area 3.12 cm^2 and 4 cm^2. The higher energy peaks are the peaks from the ^{17}O reaction.

position of the active area. However, it is most likely that the active area is located at the center of the detector. The calculated peak shape assuming the active area to be located at the center of the detector is shown in Figure 5.5. For the purpose of comparison, the calculated peak shape for the 4 cm^2 detector is also shown.

5.3 Energy calibration

The gains of the detectors were approximately matched in hardware by using a calibrated pulser; however, it was very important that the gains of the detectors be matched carefully, since the data collected in all the detectors were to be added together. As discussed in Chapter 4, the $^{10}B(p,\alpha)^{7}Be$ and $^{6}Li(p,\alpha)^{3}He$ reactions have large cross sections and produce alphas in the energy region of interest. One detrimental result of the very high purity of our targets was that there were no structures evident in our

spectra which would assist in gain calibration. To accurately calibrate the gains of the detectors, we decided to use the (p,α) reactions on ^{10}B and ^{6}Li to our advantage.

Targets of ^{10}B and ^{6}Li were fabricated by evaporation of enriched ^{10}B powder and LiF of natural isotopic composition onto 2-mm-thick aluminum backings. Periodically (after about every 6-10 hours of data collection) we would stop collecting data on Ta_2O_5 targets and would put in the LiF and ^{10}B targets. A spectrum was taken on each of these targets to check for any shifts in the gains of the detectors. No noticeable shifts (< 3 channels) in the locations of either the lithium or boron peaks were noticed over the course of the experiment. A sample spectrum taken using the ^{10}B target is shown in Figure 5.6, and a sample spectrum taken using the LiF target is shown in Figure 5.7.

The locations of the peaks from the ^{10}B and ^{6}Li reaction could not only be used to set the relative gains of the detectors, but they could also be used to determine the absolute gain calibration, and hence to predict the location of the peak from the $^{17}O(p,\alpha)^{14}N$ reaction. This was not quite straightforward, since the yields from both the ^{10}B and ^{6}Li reaction are thick-target yields. In order to determine the absolute gain calibration, the measured yield from the reactions had to be deconvoluted from the target thickness.

Deconvolution of the boron peak was aided by the fact that we had a CNDP of the ^{10}B target which we used for most of the run. The result of the CNDP is shown in Figure 5.8. The target had an areal density of ^{10}B atoms of $3x10^{16}$ atoms/cm^2, with most of the boron in the first 0.2 μm of the target. This combined with the fact that the $^{10}B(p,\alpha)^{14}N$ cross section is a direct cross section and falls exponentially with proton energy, means that all of the reactions take place very near the surface of the target. We visualize the target as being made of seven regions of varying ^{10}B density. The number of counts coming from each region of the target is proportional to the product of the

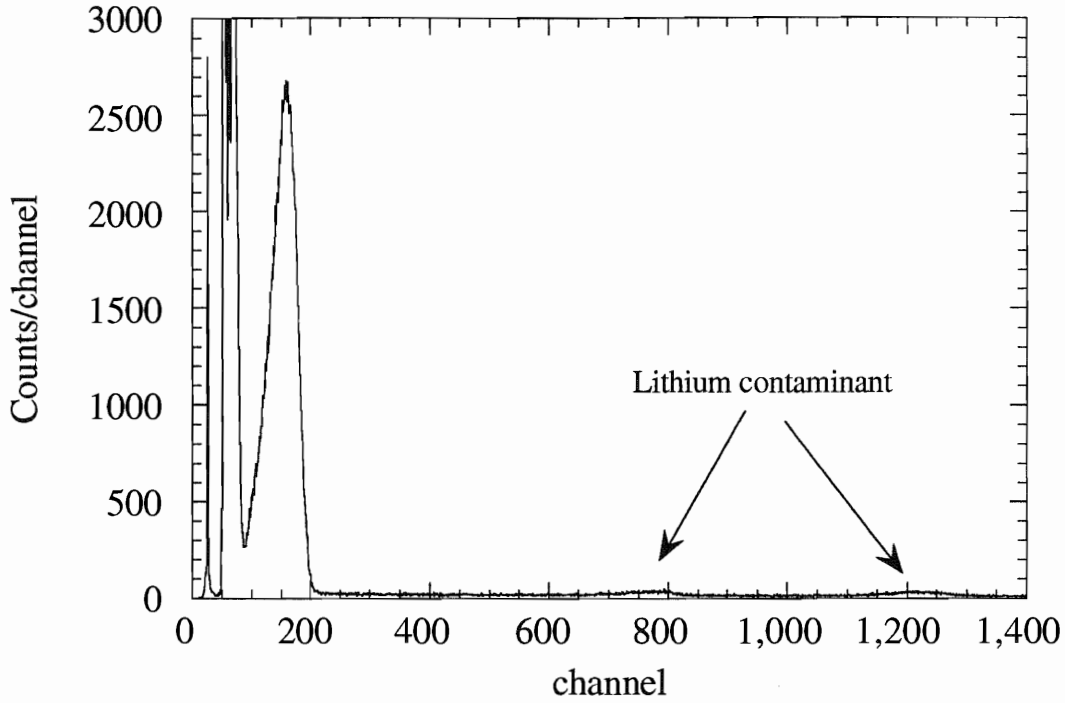

Figure 5.6: Typical energy spectrum taken on ^{10}B target. Shown is the sum of five detectors.

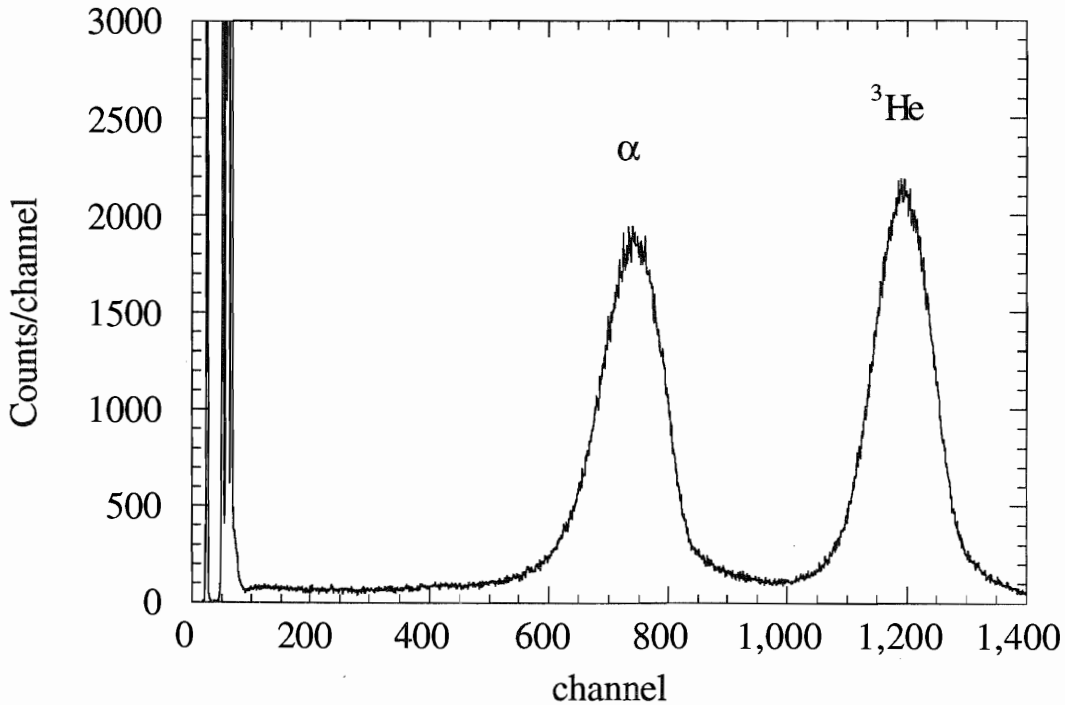

Figure 5.7: Typical energy spectrum taken on LiF target. Shown is the sum of five detectors.

cross section and the areal density of ^{10}B atoms. We denote this weighting factor by w_i. The regions of the target that we used and their appropriate weighting factors are given in Table 5.4. The cross section for the $^{10}B(p,\alpha)^{14}N$ reaction was taken from Angulo *et al.* [Ang93], and the density of ^{10}B atoms, η_{10}, was determined from the CNDP (Figure 5.8). It should be noted that the regions closest to the surface of the target have a lower weight because they correspond to thinner sections. The total line shape for the $^{10}B(p,\alpha)^{7}Be$ reaction, B(x), is then given by

$$B(x) = N\sum_{i=1}^{7} w_i b_i(x) = N\sum_{i=1}^{7} \sigma_i \eta_{10}^i b_i(x) \ , \qquad (5.3)$$

where $b_i(x)$ is the calculated line shape for each region of the target. The contribution to the total line shape from each of the seven regions is shown in Figure 5.9a. The total line shape is shown in Figure 5.9b with a typical measured boron peak.

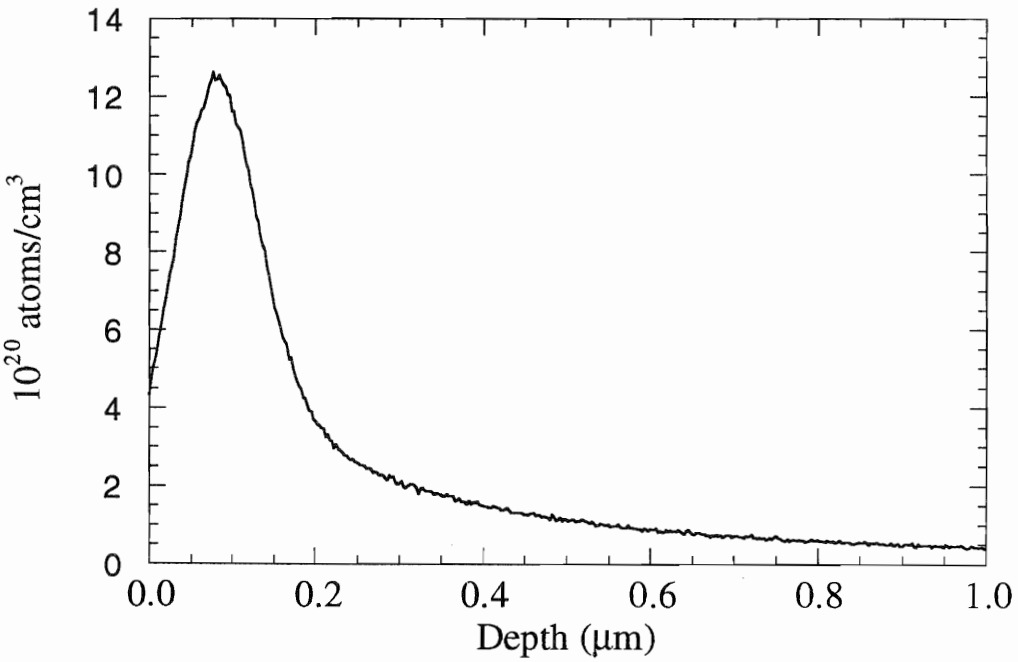

Figure 5.8: Density of ^{10}B atoms in the enriched ^{10}B target used for gain matching determined by CNDP.

Table 5.4: Regions of target used in deconvoluting alpha peak from $^{10}B(p,\alpha)^{14}N$ reaction. *From Angulo *et al.* [Ang93].

E Range (keV)	Mean E (keV)	Depth (nm)	σ (μbarns)*	(atoms/cm^2)	weight
74.8+	74.9		21	0.3	6.3
73-74.8	74	1	19	1.1	20.9
71-73	72	24	17	1.7	28.9
67-71	69	47	13	4.8	62.4
63-67	65	79	9.1	5.7	51.9
59-63	61	110	5.8	5.3	30.7
55-59	57	140	3.4	2.9	9.9

A similar procedure was followed for the lithium peak. However, a CNDP was not performed on the lithium target used, and we did not have a basis for determining the density of ^{6}Li atoms as a function of depth. Since the composition of the target was not known, we assumed that the lithium atoms are uniformly distributed in the target, and we weighted each region by the product of the cross section and its thickness. The regions of the target used in deconvoluting the lithium peak are given in Table 5.5, and the lithium cross sections were taken from Engstler *et al.* [Eng92]. The contributions to the lithium peak from each of these regions is shown in Figure 5.10a. The total lithium peak is shown in Figure 5.10b, along with a typical measured peak.

Several runs on the enriched ^{10}B and LiF target were chosen at random, and the spectra from each detector in these runs were summed to produce one composite spectra. A linear background, due primarily to the $^7Li(p,\alpha)^4He$ reaction, was subtracted from this spectra, and the result was fit with the composite peaks by varying the energy calibration of the spectra. From this procedure the gain was determined to be

$$E = 1.53\frac{\text{keV}}{\text{chan}}(chan) - 44\text{keV}. \qquad (5.4)$$

Table 5.5: Regions of target used in deconvoluting alpha peak from $^{6}Li(p,\alpha)^{3}He$ reaction. *from Engstler *et al.* [Eng92]

E Range (keV)	Mean E (keV)	Depth (nm)	σ (μbarns)*	thickness	weight
74.8+	74.9		900	1/8	110
73-74.8	74	1	870	3/8	330
71-73	72	24	750	1/2	380
67-71	69	47	630	1	630
63-67	65	79	480	1	480
59-63	61	110	360	1	360
55-59	57	140	250	1	250
51-55	53	170	160	1	160

This agrees with the gain of 1.5 keV/chan obtained with the calibrated pulser. The maximum of the oxygen peak was calculated to fall at an energy of 375 keV (see Figure 5.5). Given this gain calibration , we expect the maximum of the oxygen peak to fall in channel 275 in the spectrum.

The shape of the calculated ^{10}B peak agrees with the measured peak (Figure 9b). There are some deviations, but they are on the same order as the deviations between the boron peak shapes in different detectors. These deviations could arise from effects such as nonuniformities in the foil thickness or the uncertainty in the position of our detector. However, the calculated shape of the ^{6}Li peak has a much smaller width than the width of the measured peak (Figure 10b). The large width of the measured peak does not arise from shifts in the gain or incorrect gain matching, since the peaks for each individual detector during short runs have the same width. Since the cross section drops rapidly with energy, the only way to produce a yield over a much broader range of energies is for the concentration of Li atoms to increase with depth in the target. Since the targets were produced by evaporation, it is unlikely that the concentration will increase

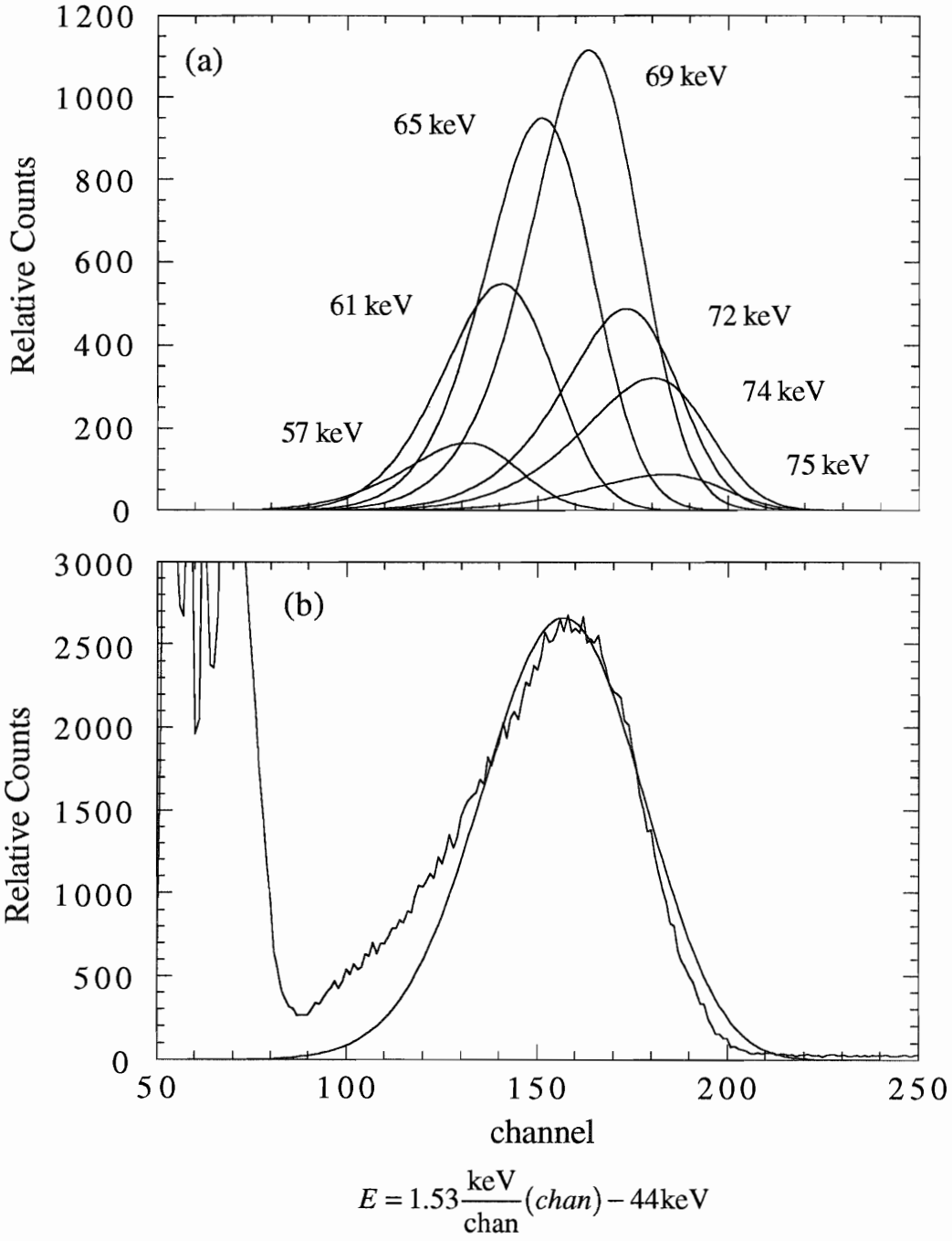

Figure 5.9: Deconvolution of alpha peak from $^{10}B(p,\alpha)^{7}Be$ reaction. (a) The calculated contributions to the total peak from each region of the target, as specified in Table 5.5. (b) The total peak compared to a typical measured peak.

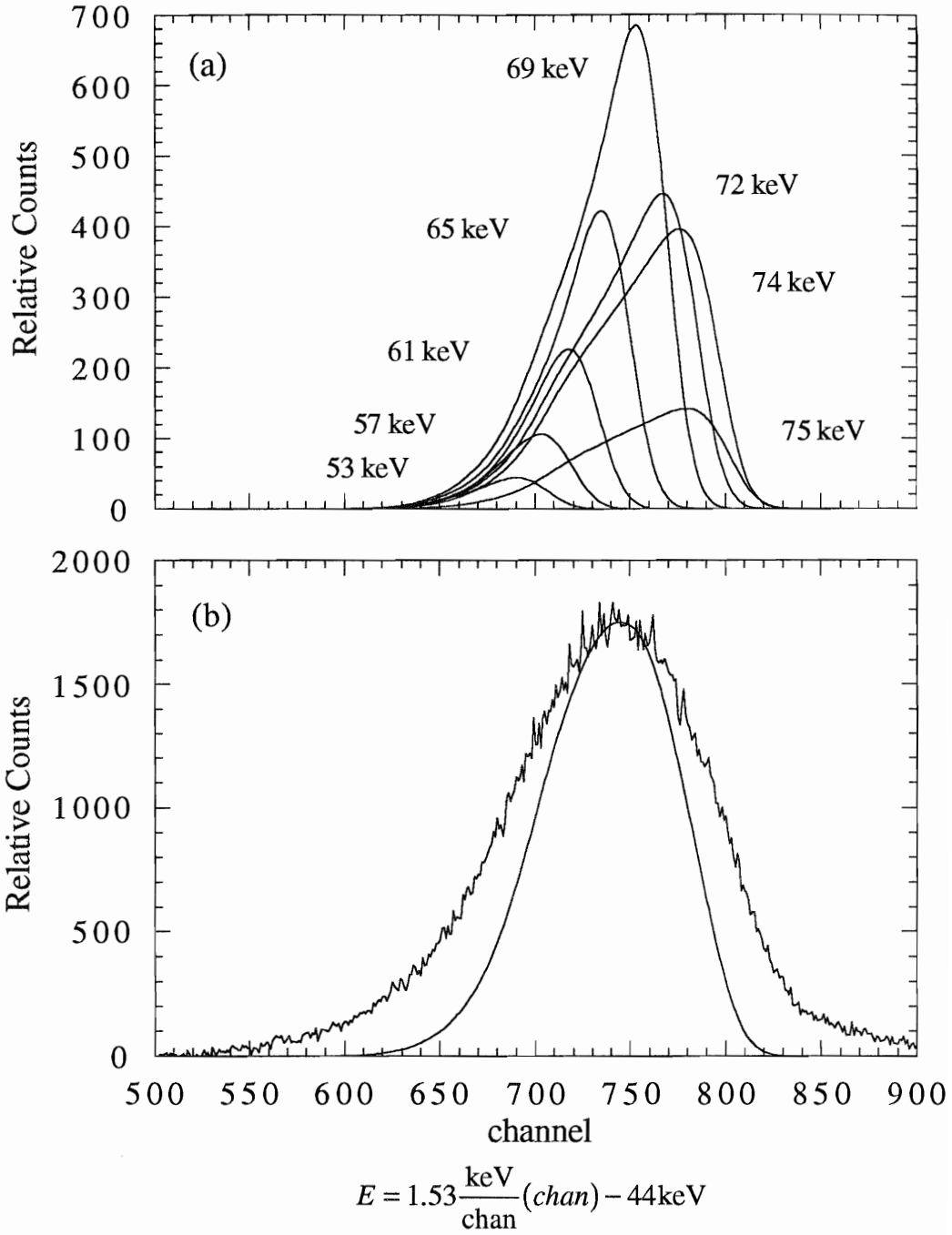

Figure 5.10: Deconvolution of alpha peak from $^{6}Li(p,\alpha)^{3}He$ reaction. (a) The calculated contributions to the total peak from each region of the target, as specified in Table 5.6. (b) The total peak compared to a typical measured peak.

significantly beyond the surface of the target. The origin of the discrepancy is therefore unresolved.

The uncertainty in the shape of the lithium peak introduces an uncertainty into our gain calibration. If the effect that is causing the larger width for the measured lithium peak is asymmetrical in energy, then the gain calibration would be off. We tookthe uncertainty in our gain calibration to be the full range of gains that would produce the calculated lithium peak within the wider, measured lithium peak. We then calculated the shift in the location of the oxygen peak with these different gains. The location of the maximum of the oxygen peak was found to stay at 275 ± 5 channels for all allowed gains.

VI. Results and Data Analysis

6.1 Data Collection

Data were collected during three experimental runs, consisting of one week of beam time each, during the months of May, June, and July of 1994. During the first run in May, we collected data solely on ^{17}O-enriched Ta_2O_5 targets at E_p = 75 keV. We had difficulties with two of our detectors in this first run. We quickly ascertained that the trouble with one detector was not with the detector itself, but was due to a tear in the nickel foil in front of the detector; however, the other detector would not take adequate bias without breaking down. We accumulated 13 C of beam on target with only 4 detectors operational, then we opened the chamber and switched the locations of these two detectors, moving the damaged detector behind the damaged nickel foil. This gave five detectors which performed admirably through the remainder of the May run and for the June and July runs. The damaged detector was left in the chamber and grounded.

Two Ta_2O_5 targets (^{17}O/a1 and ^{17}O/a2) were produced for the May run using oxygen gas enriched to 77% ^{17}O. A total of 80.6 C of charge was accumulated on target during the run, roughly half on each target. An RBS profile of one of the targets, ^{17}O/a2, taken before and after the run are shown in Figure 6.1. There was a partial depletion of oxygen observed in the targets, but the significant change in stoichiometry occurred at a depth of 0.7 μm. This is near where the protons stop in the target, and is deeper in the target than the resonance. We still adopt the effective stopping power for 77% enriched Ta_2O_5 as given by Eqn. 4.9 for the targets, but in the June and July runs we changed targets more frequently. No depletion was evident on the backside of the target which was pressed against a copper backing. This allowed us to flip the targets over, and collect data on both sides of the target.

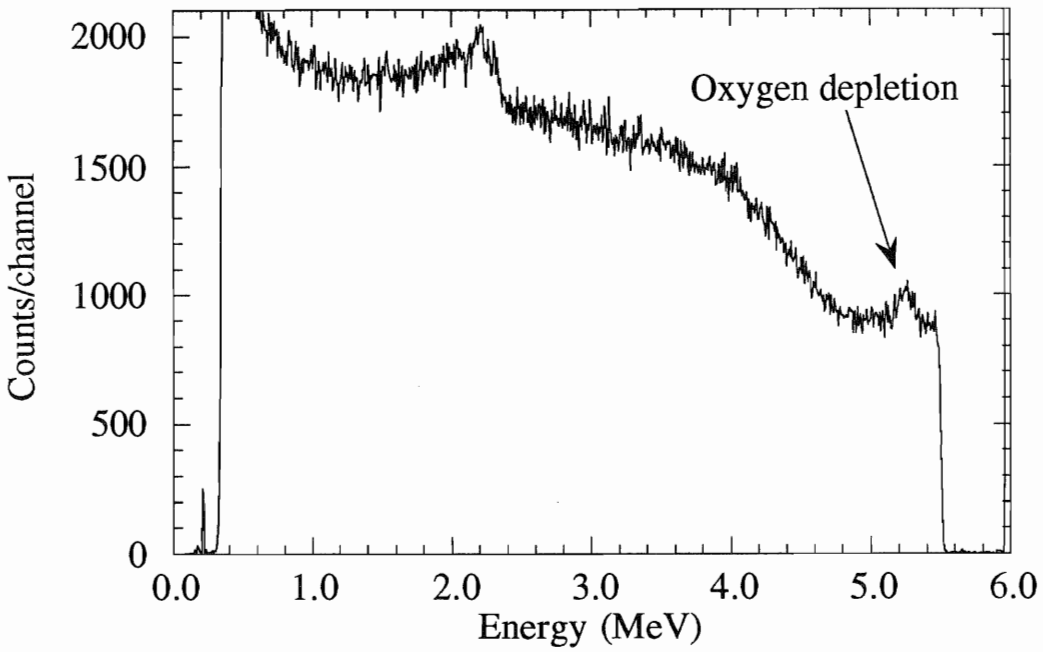

Figure 6.1: RBS profile of target $^{17}O/a2$ after an accumulated charge of 40 Coulombs.

We matched the detector gains using the $^{10}B(p,\alpha)^{7}Be$ and $^{6}Li(p,\alpha)^{3}He$ reactions and summed all of the data together. Adding the beam current on target for each detector gives a total of 391 C, since only 4 detectors were operational for the first 13 C of data taken. We were very encouraged by the results. There was a structure evident in the spectra at the energy where we expected the alphas from the resonance of interest to be. In order to determine if these counts were in fact alphas from the $^{17}O(p,\alpha)^{14}N$ reaction, we collected data during the June run using both targets made with oxygen enriched with ^{17}O and using targets made of natural isotopic composition. If the structure was due to a reaction involving ^{17}O, then it should not be observable in data taken on targets of natural isotopic composition.

Care was taken to ensure that the natural targets and the enriched targets were produced under equivalent conditions, e.g. all of the targets were cut from the same piece of tantalum, and the targets were stored in the same location. It was difficult to

duplicate precisely the pressure and temperature under which the targets were made. This resulted in some minor variations in the thickness and purity of the targets, but these are the same kinds of variations that were seen among the initial ^{17}O targets. Three targets of natural isotopic composition and two with enriched oxygen were produced for use in this run.

Data were collectedby alternating an enriched target with a target of natural isotopic composition after every 5-10 C of integrated beam, with slightly more beam time being giving to targets of natural isotopic composition. We did this to ensure that we would accumulate sufficient statistics to tell if the peak seen in the data from the May run was present in the data collected on targets of natural isotopic composition. A total of 41 C of charge was accumulated on the enriched targets, and 74 C of charge was accumulated on targets of natural isotopic composition, about 10 C per detector per side. The structure was again evident in the data taken on enriched targets, but it was not present in the data taken on targets of natural isotopic composition. This, and the energy of the peak, provide strong evidence that we detected alphas from the $^{17}O(p,\alpha)^{14}N$ reaction.

As a final test, in the July run we collected data at a beam energy of $E_p = 65$ keV. The uncertainty in the beam energy of the ion source is about 100 eV, so this energy is well below the resonance energy of $E_p = 70$ keV. If the counts are alphas from the $^{17}O(p,\alpha)^{14}N$ reaction, then they would not be present in the data taken at 65 keV. We again collected data, alternating targets with 77% ^{17}O with targets of natural isotopic composition. A total of 73 C of charge was accumulated on 4 targets (x2 sides) of enriched ^{17}O, and a total of 66 C of charge was accumulated on 3 targets (x2 sides) of natural isotopic composition. In addition, a small amount of data was also collected at $E_p = 75$ keV. The data accumulated in all of the runs is summarized in Table 6.1. Listed are the targets used and the sum of the beam current on target for all the detectors.

Table 6.1: Summary of data collected during May, June and July runs on targets of natural isotopic composition and targets enriched to 77% ^{17}O.

		May Run		June Run		July Run	
		BCI (C)	Targets	BCI (C)	Targets	BCI (C)	Targets
75 keV	^{17}O	391	^{17}O/a1*,2*	203	^{17}O/b1,2	30	^{17}O/c1
75 keV	^{16}O			364	^{16}O/b1-3	26	^{16}O/c3
65 keV	^{17}O					359	^{17}O/c1-4
65 keV	^{16}O					330	^{16}O/c1-3

6.2 Analysis

The total data collected at $E_p = 75$ keV on ^{17}O enriched targets is shown in Figure 6.2. This represents a total charge of 130 C on target. The background at higher energies arises primarily from cosmic rays and natural radioactivity, and is seen with no beam into the target chamber. At lower energies there is also pile-up of elastic protons that are not stopped in the foil. Note that there are no counts seen above background from the $^{6}Li(p,\alpha)^{3}He$ or $^{10}B(p,\alpha)^{7}Be$ reaction.

The location of the maximum of the $^{17}O(p,\alpha)^{14}N$ peak was determined from the absolute gain matching to be at channel 275 ± 5. The peak should drop to below 10% of its peak value below channel 230 and above channel 300 (see Fig. 5.5). The same data shown in Figure 6.2 have been expanded in Figure 6.3 to show the region of interest. The background was found to be well fit by an exponential plus a linear term. We excluded channels between 200-320, where the peak should be located, and channels below 150, where the exponential background gets large, and fit the remaining channels with the 4-parameter function

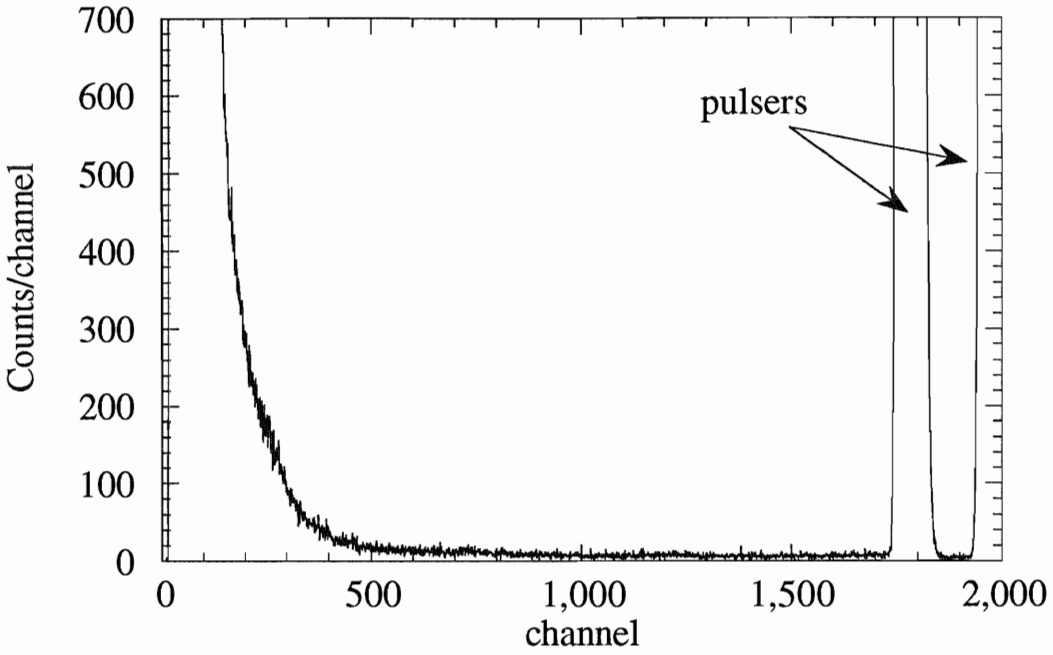

Figure 6.2: Total data (130 C) collected at E_p = 75 keV with enriched ^{17}O targets.

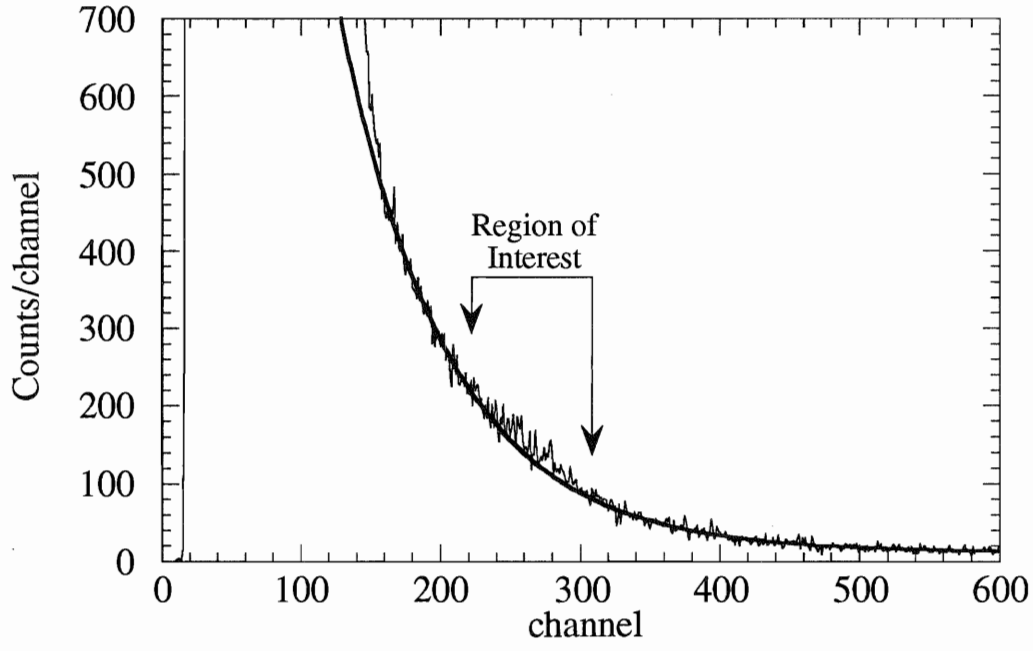

Figure 6.3: Enlargement of Figure 6.2 showing the region of interest. The smooth curve is the best fit curve to the background.

$$f(x) = \exp(p_1 + p_2 x) + p_3 + p_4 x \ . \qquad (6.1)$$

The best-fit curve to the background was determined using the MINUIT parameter optimization program with a χ^2 minimization [Jam75]. The best-fit curve is also shown in Fig. 6.3. This background was subtracted from the total data, and the result was binned by a factor of two. The background-subtracted spectrum was then fit with the calculated ^{17}O peak, where the position was fixed and the area was varied. The background-subtracted spectrum and the normalized oxygen peak are shown in Figure 6.4.

Although the location of the observed peak coincides with the predicted location, there is some uncertainty in the gain calibration. To determine the number of counts in the peak and its corresponding error, we fit the peak with the 6-parameter function

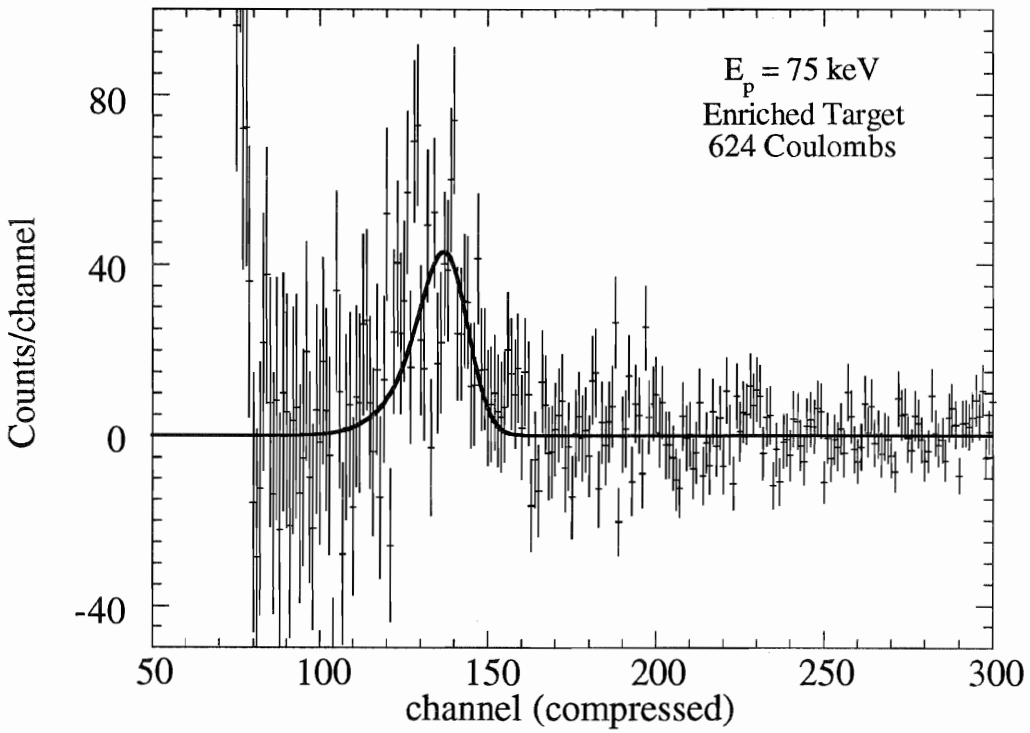

Figure 6.4: The total data subtracting the best-fit background as given by Eqn. 6.1.

$$f(x) = \exp(p_1 + p_2 x) + p_3 + p_4 x + p_5 b(x + p_6) \ , \qquad (6.2)$$

where b(x) is the calculated peak for the $^{17}O(p,\alpha)^{14}N$ reaction. The parameter p_5 is the number of counts in the peak and p_6 is the number of channels the peak is offset from its calculated position. The parameters and their corresponding errors determined from this fit are given in Table 6.2. The number of counts observed is 860 ± 130 counts. The best-fit location of the peak is 4 channels lower than predicted, but this is within the error of the gain-matching.

To determine if this structure is alpha-particles from the state of interest, we would like to compare data with comparable statistics taken from 3 different scenarios: (1) E_p = 75 keV with enriched targets, (2) E_p = 75 keV with natural targets, and (3) E_p = 65 keV with enriched targets. During the June run we collected 364 C of charge (sum of all detectors) on targets of natural isotopic composition. We collected only 203 C of charge on enriched targets. We randomly selected individual runs from the May run and added them to the total data from the June run until we had comparable statistics for both

Table 6.2: Best-fit parameter values to the total data using Eqn. 6.2.

parameter	best-fit	error
p_1	8.20	0.07
p_2	-0.012969	0.0003
p_3	16	1
p_4	-0.008	0.001
p_5	860	130
p_6	4	2

scenario (1) and (2). Roughly this same amount of data was collected at $E_p = 65$ keV on enriched targets.

We fit each of these sets of data with the 4-parameter function given in Eqn. 6.1. The channels fit were from 150-200 and from 320-900. The best fit background curves were then subtracted from the data, and the difference binned by a factor of two. We then fit each of these spectra with the calculated peak from the $^{17}O(p,\alpha)^{14}N$. The results of this analysis are shown in Figure 6.5. In the data taken at $E_p = 75$ keV on enriched targets, the area in the oxygen peak was found to be 465 ± 65 counts. For the data collected at $E_p = 75$ keV on targets of natural isotopic composition, the area was found to be 9 ± 54 counts. For the data collected at $E_p = 65$ keV on enriched ^{17}O targets, the area was found to be 44 ± 55 counts. Thus the signal was evident only for data collected at $E_p = 75$ keV on enriched ^{17}O targets. Also note that the number of counts determined from this analysis of a subset of the total data gives a number of counts which is consistent with that from the full set. Since the structure is seen at the correct energy and only in targets enriched with ^{17}O at a beam energy of 75 keV, we conclude that the counts seen are alphas from the $E_p = 70$ keV resonance in the $^{17}O(p,\alpha)^{14}N$ reaction.

The yield from a narrow resonance is given by Eqn. 3.6. However, this equation is evaluated in the center-of-mass frame. Both the effective stopping power and the detector efficiency have been determined in the lab frame. The detector efficiency in the center-of-mass was calculated assuming a detector placement as described in Section 5.2. It was found to be 0.0261 ± 0.0003, 97% of the efficiency in the lab frame. The effective stopping power can be changed from the lab frame to the center of mass frame by multiplying by the usual factor M/(M+m), where M is the mass of ^{17}O and m is the mass of the proton. Solving Eqn. 3.6 for the proton width, Γ_p, given these changes, results in

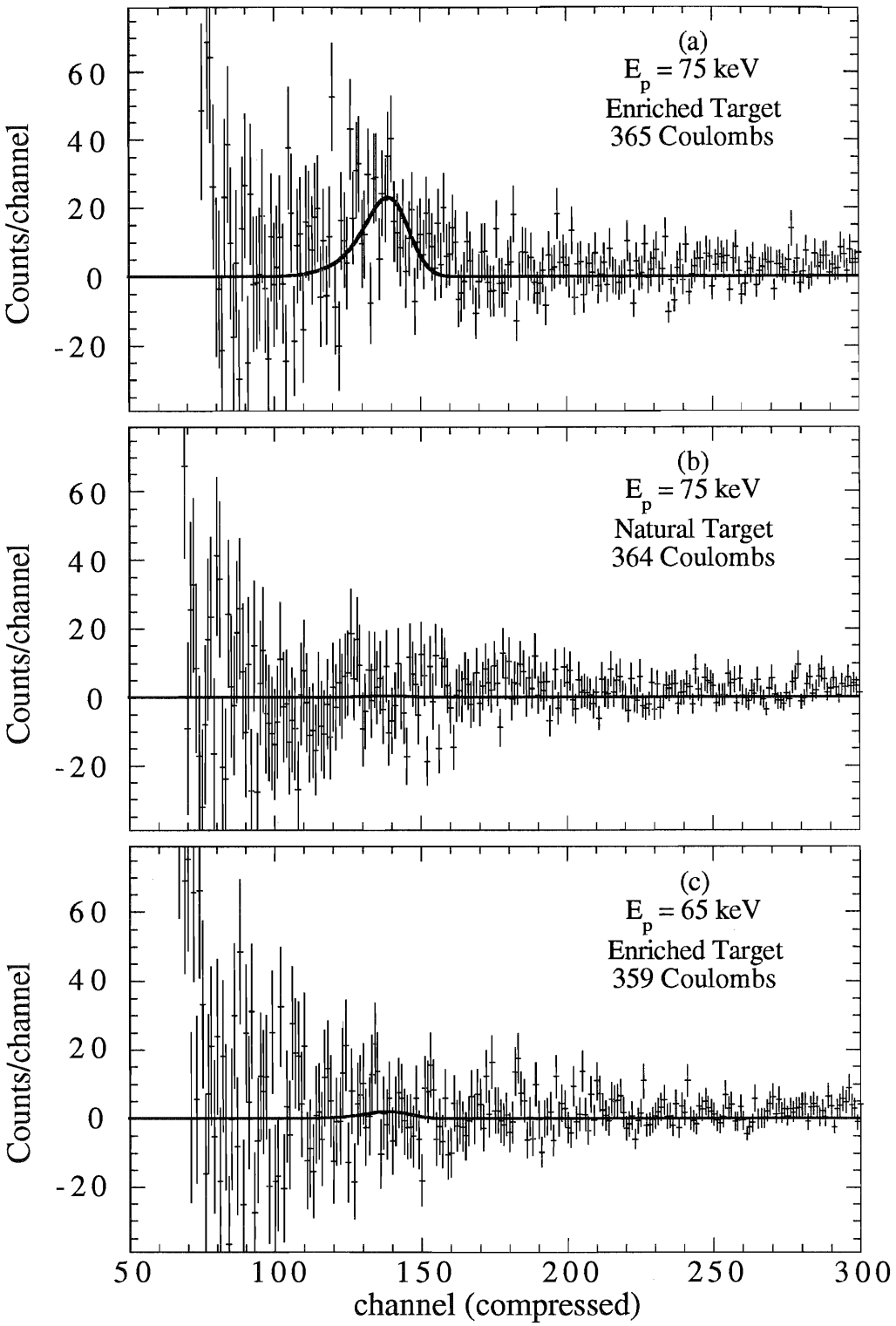

Figure 6.5: Comparison of background subtracted spectra from data taken at E_p = 75 keV on both enriched targets and targets of natural isotopic composition, and data taken at E_p = 65 keV on enriched targets. The smooth curve is calculated ^{17}O peak fit to the background-subtracted spectrum.

$$\Gamma_p = \frac{N_\alpha}{I}\frac{\varepsilon_{\text{eff}}}{\Omega_{\text{cm}}}\left(2e\frac{1}{\lambda^2}\frac{1}{\omega}\frac{\Gamma_T}{\Gamma_\alpha}\frac{M}{M+m}\right). \tag{6.3}$$

Inserting the values for all the known quantities in Eqn. 6.3, leaves

$$\Gamma_p = 10{,}500\left(\frac{N_\alpha}{I}\frac{\varepsilon_{\text{eff}}}{\Omega_{\text{cm}}}\right)\left(\frac{\text{atoms}\cdot\text{C}}{\text{cm}^2}\right). \tag{6.4}$$

The values for the remaining quantities as determined in this experiment are summarized in Table 6.3, where the uncertainty in the value of Γ_p arising from each of these quantities, $\sigma(\Gamma_p)$, is also given. The uncertainty in the target density, beam current, and solid angle are all systematic errors. We cannot combine these errors without knowing something about their probability distribution. Since nothing is known about these distributions, we add these errors in quadrature, as if they were random Gaussian errors. This may not necessarily be an accurate estimate of the total error. Substituting the mean values of these four quantities and adding the errors in quadrature results in a value for the proton width of the 5673 keV state in ^{18}F of

$$\Gamma_p = 22 \pm 4 \text{ neV} . \tag{6.5}$$

We have not accounted for the screening of the ^{17}O nucleus by the atomic electrons in determining the width. The width for scattering by bare nuclei will be smaller than that given in Eqn. 6.5. One model of electron screening calculates the reduction in the width to be 20% [Ass87]. However, recent measurements that show the effects of electron screening have not been successfully described by theoretical predictions [Sch89, Eng92, Ang93]. Electron screening appears to be more complicated than is treated by current models. A proper treatment would remove the enhancement to the measured width caused by the atomic electrons, and then add an enhancement to the

Table 6.3: Contributions to the uncertainty in the measured value of Γ_p.

Quantity	Mean Value	$\sigma(\Gamma_p)$(neV)
N_α	860 ± 130	± 3
ε_{eff}	39 ± 4 (10^{-15} eV·cm^2)	± 2
I	$624\ ^{+19}_{-42}$ C	$^{+2}_{-1}$
Ω_{cm}	0.0261 ± 0.0006	± 0.4

width due to the screening in the astrophysical environment. To some extent this two effects cancel, and owing to the uncertainty in how to treat them, we omit them.

VII. Conclusions and Astrophysical Implications

The proton width of the E_x = 5673 keV state in ^{18}F as determined by this measurement is given in comparison to the results of other measurements in Table 7.1. Our value is consistent with the less accurate measurement of Landre *et al.*, but not with the upper limit set by Berheide *et al.* in an experiment similar to ours. In setting the upper limit on the number of alphas detected, Berheide *et al.* assumed that their sensitivity was given by Eqn. 2.10. Because of their background from the $^{10}B(p,\alpha)^7Be$ reaction, it is difficult to determine whether structure exists in the region of interest, and it is not safe to assume that the counts seen in their spectrum arise entirely from background. Eqn. 2.10 is true only under idealized circumstances and certainly is an underestimate in this case.

Our value for the proton width of the 5673-keV state implies a $^{17}O(p,\alpha)^{14}N$ reaction rate which is considerably larger than the upper bound tabulated by Fowler *et al.* [Fow75]. We write the total reaction rate, r, as a sum of 6 terms

$$r = \sum_{i=1}^{6} r_i \ . \tag{7.1}$$

Table 7.1: Comparison of measured value of Γ_p for the 5673-keV state in ^{18}F with previous measurements.

Author	Reaction	Γ_p (neV)
Landre *et al.* [Lan89]	$^{17}O(^3He,d)^{18}F$	71^{+40}_{-57}
Blackmon (this work)	$^{17}O(p,\alpha)^{14}N$	22 ± 4
Berheide *et al.* [Ber92]	$^{17}O(p,\alpha)^{14}N$	≤ 3

The contribution from each of these terms is given in Table 7.2. The resonant contribution from the 5673-keV state dominates the reaction rate. Except at very low or very high temperatures, the reaction rate can be approximated very well by this one term. There is a correction to this term that approximates the low energy tail of the resonance. This term corrects for the error that was made in approximating the integral in Eqn. 2.5. There are also two terms that are the resonant contributions from the E_x = 5603 and 5786 keV states. For these two terms we adopt the rates given by Landre *et al.* [Lan89]. For the contribution from the 5786-keV state, only an upper limit is known. We give this rate at its upper limit, but multiply by a scaling factor, f, which takes on values from 0 to 1. Lastly, there is the nonresonant contribution and the contribution from the tails of higher energy resonances. For these terms we adopt the values of Fowler *et al.* [Fow75]. The contribution of each of these terms to the reaction rate is shown in Figure 7.1. For temperatures in the range $0.025 < T_9 < 0.100$, the reaction rate is dominated by the E_x = 5673 keV resonance.

Table 7.2: Terms contributing to the $^{17}O(p,\alpha)^{14}N$ reaction rate.

Term	Source	Reaction Rate
5673-keV state	this work	$1.6\text{x}10^{-5} T_9^{-3/2} \exp\left(-0.767 T_9^{-1}\right)$
5673-keV state	this work	$1.5\text{x}10^{10} T_9 \exp\left(-16.667 T_9^{-1/3} - \left(\frac{T_9}{0.040}\right)^2\right)$
5603-keV state	[Lan89]	$1.78\text{x}10^{5} T_9^{-2/3} \exp\left(-16.669 T_9^{-1/3}\right)\left(0.479 T_9^{2/3} + 0.00312\right)^{-2}$
5786-keV state	[Lan89]	$f \times 98 T_9^{-3/2} \exp\left(-2.077 T_9^{-1}\right)$
nonresonant	[Fow75]	$1.53\text{x}10^{7} T_9^{-2/3} \exp\left(-16.712 T_9^{-1/3} - \left(\frac{T_9}{0.565}\right)^2\right) \times$ $\left(1 + 0.025 T_9^{1/3} + 5.23 T_9^{2/3} + 0.94 T_9 + 13.5 T_9^{4/3} + 5.98 T_9^{5/3}\right)$
HE reson. tail	[Fow75]	$2.92\text{x}10^{6} T_9 \exp\left(-4.247 T_9^{-1}\right)$

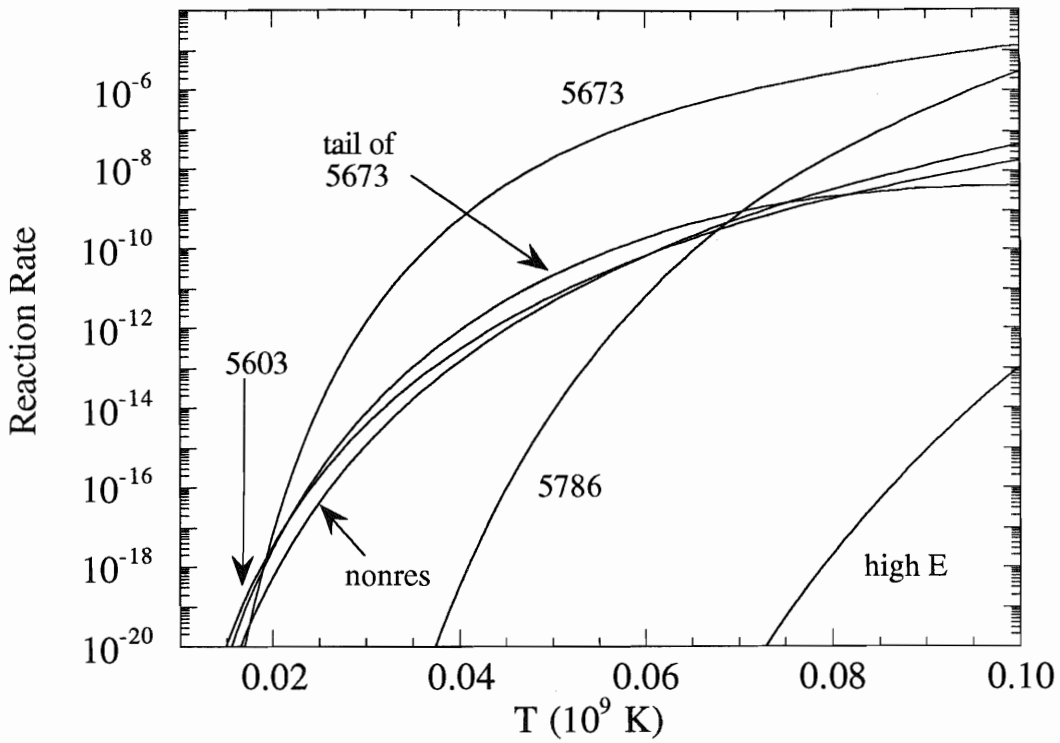

Figure 7.1: Contribution of each term (see Table 7.2) to the $^{17}O(p,\alpha)^{14}N$ reaction rate.

The total range of values consistent with the $^{17}O(p,\alpha)^{14}N$ reaction rate, given our new measurement, is shown in Figure 7.2. The low and high reaction rates of Fowler *et al.* are shown for comparison [Fow75]. For a wide range of temperatures the new reaction rate is higher than the upper limit used previously by about a factor of 10. This increased destruction rate for the ^{17}O isotope will increase the theoretical $^{16}O/^{17}O$ ratio in the atmospheres of red giants. Most importantly, only a narrow range of values are now allowed for the $^{17}O(p,\alpha)^{14}N$ reaction rate. This means that the $^{16}O/^{17}O$ can now be predicted with relative certainty from stellar models and observations can be used to constrain both convective and nonconvective mixing.

Figure 1.5 shows the observed $^{16}O/^{17}O$ ratio in 14 red giants and the calculated abundance ratio by Dearborn [Dear92], using the upper and lower limit on the

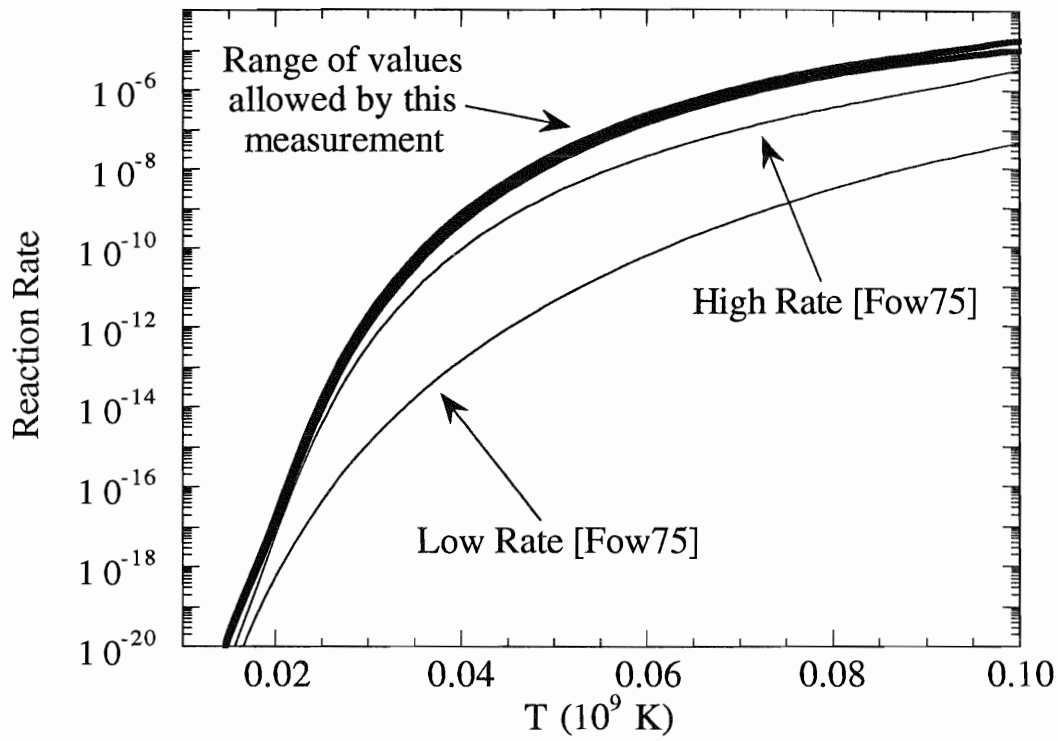

Figure 7.2: The total $^{17}O(p,\alpha)^{14}N$ reaction rate.

$^{17}O(p,\alpha)^{14}N$ reaction rate from Fowler *et al.* [Fow75]. Figure 7.3 shows this same data with the calculations of Dearborn for the f=1 destruction rate. Also shown is a calculation by El Eid that using our new value for the $^{17}O(p,\alpha)^{14}N$ rate [Ele94b]. The calculation of El Eid differs from that of Dearborn for two reasons. First is the increased value in the ^{17}O destruction rate. This results in the production of a consistently higher value for the $^{16}O/^{17}O$ ratio in stars heavier than 3 solar masses. The calculations also differ in the opacities and mixing lengths that were used. This is particularly evident in stars with masses less than about 2.5 solar masses.

With a certain value for the $^{17}O(p,\alpha)^{14}N$ reaction rate, convection and mass flow become the main parameters which affect the $^{16}O/^{17}O$ ratio. It is now possible to use observations of the $^{16}O/^{17}O$ ratio to constrain these parameters. However, we cannot impose a stringent constraint because of the uncertainties in the observed $^{16}O/^{17}O$ ratio.

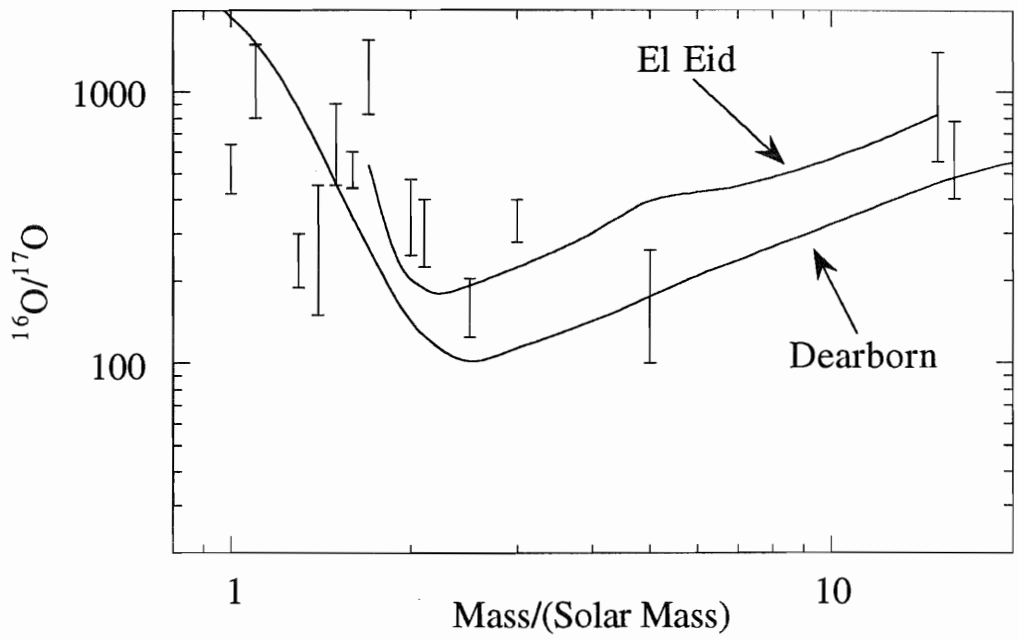

Figure 7.3: Comparison of the measured $^{16}O/^{17}O$ ratios in 14 red giants [Har84a, Har84b, Har88] to theoretical calculations of Dearborn [Dea92] and El Eid [Ele94b].

It appears that the model of El Eid gives a better fit to the observations than that of Dearborn. Not shown in Figure 7.3 are the uncertainties in the masses of the observed stars. These model-dependent uncertainties add large horizontal error bars to the plot.

The calculated abundance of El Eid predicts a minimum value for the $^{16}O/^{17}O$ ratio of about 200, while the calculation of Dearborn predicts a minimum of about half this value. One reason for the discrepancy is a difference in the way convective mixing and overshoot are treated. Because of the large error bars in the observed abundances, we cannot discriminate between the two models. It is at least reassuring that no stars have been observed with a $^{16}O/^{17}O$ ratio less than 200. However, we can get no more than reassurance from this. It should be possible to reduce the uncertainty in these observations by more than a factor of 2 using the latest spectrographic equipment. It is equally important to reduce the uncertainty in the mass of stars in the sample. This may be accomplished by observing stars in young clusters where the main sequence turn-off

can be used to determine the mass. With such improved observations, it will be possible to impose meaningful constraints on the depth of convective mixing and on the amount of nonconvective mixing occuring on the main sequence.

References

[Ajz87] F. Ajzenberg-Selove, Nucl. Phys. A **475**, 1 (1987).

[And77a] H.H. Anderson and J.F. Ziegler, *Hydrogen Stopping Powers and Ranges in All Elements* (Pergamon Press, New York, 1977).

[And77b] H.H. Anderson and J.F. Ziegler, *Helium Stopping Powers and Ranges in All Elements* (Pergamon Press, New York, 1977).

[Ang93] C. Angulo, S. Engstler, G. Raimann, C. Rolfs, W.H. Schulte, and E. Somorjai, Z. Phys. A **345**, 231 (1993).

[Ass87] H.J. Assenbaum, K. Langanke, and C. Rolfs, Z. Phys. A **327**, 461 (1989).

[Ber92] M. Berheide, C. Rolfs, U. Schröder and H.P. Trautvetter, Z. Phys. A **343**, 483 (1992).

[Ber77] I. Berka, K.P. Jackson, C. Rolfs, A.M. Charlesworth, and R.E. Azuma, Nucl. Phys. A **288**, 317 (1977).

[Bet80] G. Betz, Surf. Sci. **92**, 283 (1990).

[Bog89] G. Bogaert, V. Landre, P. Aguer, S. Barhoumi, M. Kious, A. Lefebvre, J.P. Thibaud, and D. Bertault, Phys. Rev. C **39**, 265 (1989).

[Boh89] E. Bohm-Vitense, *Introduction to Stellar Astrophysics Vol. 3: Stellar Structure and Evolution* (Cambridge University Press, Cambridge, England, 1989).

[Boo94] A.I. Boothroyd, I.-J. Sackmann and G.J. Wasserburg, Astrophys. J. **430**, 77L (1994).

[Che84] S. Chereckdjian and I.H. Wilson, Nucl. Inst. Meth. Phys. Res. B **1**, 258 (1984).

[Cla83] D.D. Clayton, *Principles of Stellar Evolution and Nucleosynthesis* (University of Chicago Press, Chicago, 1983).

[Cau89] G.R. Caughlan and W.A. Fowler, At. Data Nuclear Data Tables **40**, 283 (1989).

[Dea92] D.S.P. Dearborn, Phys. Rep. **210**, 367 (1992).

[Dom63] J.J. Domingo, Ph.D. Dissertation, Yale University (1963).

[Dom65] J.J. Domingo, Nucl. Phys. **65**, 39 (1965).

[Dom86] J.F. Dominy and G. Wallerstein, Astrophys. J. **317**, 810 (1986).

[Dow93] R.G. Downing, G.P. Lamaze, J.K. Langland, and S.T. Hwang, J. Res. Natl. Inst. Stand. Technol. **98**, 109 (1993).

[Ele94a] M.F. El Eid, Astron. Astrophys. **285**, 915 (1994).

[Ele94b] M.F. El Eid, private communication, 1994.

[Eng92] S. Engstler, G. Raimann, C. Angulo, U. Greife, C. Rolfs, U. Schröder, E. Somorjai, B. Kirch, and K. Langanke, Z. Phys. A **342**, 471 (1992).

[Fow75] W.A. Fowler, G.R. Caughlan, and B.A. Zimmerman, Annu. Rev. Astron. Astrophys. **13**, 69 (1975).

[Har84a] M.J. Harris and D.L. Lambert, Astrophys. J. **281**, 739 (1984).

[Har84b] M.J. Harris and D.L. Lambert, Astrophys. J. **284**, 223 (1984).

[Har88] M.J. Harris, D.L. Lambert and V.V. Smith, Astrophys. J. **325**, 768 (1988).

[Ick91] I. Iben, Astrophys. J. Suppl. Ser. **76**, 55 (1991).

[Jam75] F. James and M. Roos, Comput. Phys. Commun. **10**, 343 (1975).

[Lan89] V. Landre, P. Aguer, G. Bogaert, A. Lefebvre, J.P. Thibaud, S. Fortier, J.M. Maison, and J. Vernotte, Phys. Rev. C **40**, 1972 (1989).

[Mak80] H.B. Mak, G.T. Ewan, H.C. Evans, J.D. McArthur, W. McLatchie, and R.E. Azuma, Nucl. Phys. A **343**, 79 (1980).

[Mat84] N. Matsunami, Atomic Data & Nucl. Data Tables **31**, 1 (1984).

[Mer70] E. Merzbacher, *Quantum Mechanics* (Wiley, New York, 1970).

[Mus85] R.G. Musket, D.W. Brown and H.C. Hayden, Nucl. Inst. Meth. Phys. Res. B **7/8**, 31 (1985).

[Rol73] C. Rolfs, A.M. Charlesworth, and R.E. Azuma, Nucl. Phys. A **199**, 257 (1973).

[Rol75] C. Rolfs and W.S. Rodney, Nucl. Phys. A **250**, 295 (1975).

[Rol88] C. Rolfs and W.S. Rodney, *Cauldrons in the Cosmos* (University of Chicago Press, Chicago, 1988).

[Sch89] U. Schröder, S. Engstler, A. Krauss, K. Neldner, C. Rolfs, E. Somorjai, and K. Langanke, Nucl. Inst. Meth. Phys. Res. B **40/41**, 466 (1989).